Master's thesis

NTNU
Norwegian University of Science and Technology
Faculty of Natural Sciences
Department of Materials Science and Engineering

Tonje Aasheim Nymark

# Micro cracks in wind turbine bearings

## Investigation of microstructural characteristics and nanomechanical properties in White Etching Cracks (WEC)

Master's thesis in Materials Science and Engineering
Supervisor: Ida Westermann, Anette Brocks Hagen
Co-supervisor: Vigdis Olden
June 2022

NTNU
Norwegian University of
Science and Technology

Tonje Aasheim Nymark

# Micro cracks in wind turbine bearings

## Investigation of microstructural characteristics and nanomechanical properties in White Etching Cracks (WEC)

Master’s thesis in Materials Science and Engineering
Supervisor: Ida Westermann, Anette Brocks Hagen
Co-supervisor: Vigdis Olden
June 2022

Norwegian University of Science and Technology
Faculty of Natural Sciences
Department of Materials Science and Engineering

NTNU
Norwegian University of
Science and Technology

# Preface

This master thesis has been written in the course TMT4905 - Materials Technology, Master's Thesis in the spring of 2022 at the Department of Material Science and Engineering at NTNU. The thesis is written in cooperation with SFI PhysMet and AEMON, with Professor Ida Westermann (NTNU), Anette Brocks Hagen (SINTEF) and Vigdis Olden (SINTEF) as supervisors of the work. The work is a continuation of research conducted in the course TMT4500 Materials Technology, Specialization Project in the fall of 2021.

This master thesis could not have been written without the support of others. The first acknowledgement goes to my supervisors Ida Westermann, Anette Brocks Hagen and Vigdis Olden for their guidance, support and the possibility to write a publication on the project thesis. I could not wish for a better team of supervisors.

For my laboratory work, I would like to thank Yingda Yu, Sergey Khromov and Ingvild Runningen for technical assistance and introduction to testing equipment. Also, Morten Peder Raanes deserves a thank for performing the EPMA analysis and Anette Brocks Hagen for the nanoindentation. The experimental work could not have been done without Shymon Bernat for supplying a sample with WECs at the right moment. Thank you for your hard work on the test rig to introduce WECs.

Finally, I would like to thank my fellow students for five wonderful years, especially Ronja Björklund for your support and friendship, and my roommates for five amazing years living with you.

# Abstract

Over the last decades, there has been an increase in wind power capacity to reach renewable energy targets. To continue the growth of the renewable energy power capacity it is important to keep the operation and maintenance costs low, however, different failure mechanisms cost the industry millions every year. One of these failure mechanisms is White Etching Cracks (WECs). WECs develop in gears and bearings at moderate load and cycles, and the damage often leads to early fatigue, often only after 5-10 % of the estimated lifetime of 20 years.

WECs are characteristic due to the White Etching Matter (WEM) which is found at the crack faces. The WEM consists of a nano-crystalline ferrite which requires a microstructural transformation from the martensitic bulk microstructure through a low-temperature recrystallization process. The initiation and formation mechanisms of WEM are still under debate, however, there is broad consensus that the crack is responsible for WEM formation. Although voids, carbides, and other stress raisers have also been proposed as initiators, inclusions have been proven to be the most frequent initiating point.

This study aims to contribute to an increased understanding of the initiation and propagation mechanisms of WEC and how the mechanical properties are affected by the WEM, through a detailed microstructural characterisation of WEC features in a 100Cr6 through-hardened martensitic bearing steel. A combination of characterisation techniques, such as Scanning Electron Microscopy (SEM) combined with Electron Backscatter Diffraction (EBSD), Energy Dispersive X-ray Spectroscopy (EDS) and Backscatter Electron (BSE) imaging, Electron Probe Microanalysis (EPMA) and nanoindentation hardness measurements have been used in this study. The results have been compared to an 18CrNiMo7-6 case-hardened steel, partly investigated with EPMA in this study and previously investigated with SEM, EBSD, BSE and nanoindentation during the authors' project thesis.

The analysis conducted on the 100Cr6 trough hardened steel found many WEC in the initiation stage in a limited section of the bearing outer race. The drivers of the crack initiation were suggested to be hydrogen diffusion into the material due to a combination of electrical current and 'bad lubricant'. Initiation points were found to be small MnS and dual-phase inclusions. Microstructural features such as differences in grain size, voids, crack residues and mass transfer into WEM were suggested as evidence that WEM is created due to crack faces rubbing while the crack is moving normal to the surface through the material. The WEM was found to be carbon depleted compared to the parent material due to carbide dissolution.

A 36 % increase in hardness was observed in the WEM compared to the matrix, likely due to reduced grain size, high dislocation densities and high carbon content.

The EPMA investigation of the case-hardened steel found that the carbon concentration was homogenised throughout the WEM and matrix. During the comparison of the two steel grades, it was found that the microstructural features inside the WEM were the same in both steels, although the carbon content was higher in the through-hardened and the hardness of the WEM was higher in the case-hardened steel.

# Sammendrag

De siste tiårene har det vært en økning i verdens produksjonskapasitet fra vindenergi for å nå klima- og energimål. For fortsette å øke produksjonskapasiteten av fornybar energi er det viktig å holde drifts og vedlikeholdskostnadene lave, men, ulike feilmekanismer koster industrien millioner hvert år. En av disse feilmekanismene er sprekker med et hvitetsende område rundt sprekkflatene, kalt 'White Etching Cracks' (WECs). WECs dannes i gir og lagre etter moderat belastning og antall sykluser. Skaden leder ofte til tidlig utmattelse av materialet, ofte så tidlig som etter 5-10 % av en estimert livstid på 20 år.

WECs er veldig karakteristiske grunnet dette hvitetsende området kalt 'White Etching Matter' (WEM) i sprekkområdet. WEM inneholder nanokrystallinsk ferritt, som dannes gjennom en transformasjon av martensitt mikrostruktur via en lav-temperatur rekrystalliseringsprosess. Initierings- og formasjonsmekanismene debatteres enda, men det er en bred enighet om at sprekken dannes før WEM, og at sprekken er årsaken til at det dannes WEM. Tomrom, karbider og andre stress elementer som øker stresset i materialet har blitt nevnt som sprekkinitieringspunkt, men inneslutninger har vist seg å være det mest hyppige initieringspunktet.

Denne studien har som mål å bidra til en økt forståelse av initierings- og forplantningsmekanismene til WEC og hvordan de mekaniske egenskapene påvirkes av WEM, gjennom en detaljert mikrostrukturell karakterisering av WEC sine egenskaper i ett 100Cr6 gjennomherdet martensittisk lagerstål. En kombinasjon av karakteriseringsteknikker, som skanningelektronmikroskopi (SEM) kombinert med diffraksjon av tilbakespredte elektroner (EBSD), tilbakespredt elektron (BSE) avbildning og energi spredende røntgen spektroskopi (EDS), mikrosonde (EPMA) og hardhetsmålinger ved hjelp av nanoinnentering har blitt brukt i denne studien. Resultatene ble sammenlignet med ett 18CrNiMo7-6 settherdet stål delvis undersøkt med EPMA i denne studien og tidligere undersøkt med SEM, EBSD, BSE og nanoindentering under forfatterens prosjektoppgave.

Analysen utført på 100Cr6 gjennomherdet lagerstål fant mange WECs i startfasen av sprekkformasjon i en begrenset del av lagerets ytre løp. Driverne for sprekkinitieringen ble foreslått å være hydrogendiffusjon inn i materialet på grunn av en kombinasjon av elektrisk spenning og en WEC framkallende lubrikant. Initieringspunkt var små MnS og flerfasede inneslutninger. Mikrostrukturelle egenskaper som forskjeller i kornstørrelse, hulrom, sprekkrester og masseoverføring til WEM ble foreslått som bevis på at WEM dannes på grunn av sprekkflater som gnis mens sprekken beveger seg normalt til overflaten gjennom materialet. WEM ble funnet å

være karbonfattig sammenlignet med matrix på grunn av karbidoppløsning. En 36 % økning i hardhet ble observert i WEM sammenlignet med matrix, sannsynligvis på grunn av redusert kornstørrelse, høye dislokasjonstettheter og høyt karboninnhold.

EPMA-undersøkelsen av det settherdede stålet viste at karbonkonsentrasjonen var homogenisert gjennom hele WEM og matrix. Under sammenligningen av resultatet ble det funnet at de mikrostrukturelle egenskapene inne i WEM var de samme i begge stålkvaliteter, selv om karboninnholdet var høyere i det gjennomherdede og hardheten til WEM var høyere i settherdet stål.

# Table of Contents

# List of Figures

# List of Tables

# Abbreviations

| | |
|---|---|
| APT | Atom Probe Tomography |
| BCC | Body-Centered Cubic |
| BCT | Body-Centered Tetragonal |
| BSE | Back-Scattered Electron |
| CH | Case-hardened |
| DRX | Dynamic Recrystallization |
| EBSD | Electron Backscatter Diffraction |
| EDS | Energy Dispersive X-ray Spectroscopy |
| EPMA | Electron Probe Microanalysis |
| GAM | Grain Average Missorientation |
| ISE | Indentation Size Effect |
| IPF | Inverse Pole Figure |
| IQ | Image Quality |
| LOM | Light Optical Microscopy |
| OP | Oliver-Pharr |
| PFIB-SEM | Xe+ Plasma Focused Ion Beam - Scanning Electron microscope |
| RCF | Rolling Contact Fatigue |
| RX | Recrystallization |
| SAED | Selected Area Diffraction |
| SE | Secondary Electrons |
| SEM | Scanning Electron Microscopy |
| SPM | Scanning Probe Microscopy |
| TH | Though-hardened |
| WEA | White Etching Area |

| | |
|---|---|
| WEC | White Etching Cracks |
| WEM | White Etching Matter |
| WSF | White Structure Flaking |
| ZDDP | Zinc Dithiophosphates |

# Units

| | |
|---|---|
| ° | degrees |
| °C | degrees Celsius |
| $\mu$m | micrometre |
| $\mu$s | micronewton |
| $\mu$N | microsecond |
| % | percent |
| at.% | atom percentage |
| fps | frames per second |
| GPa | gigapascal |
| g | gram |
| h | hours |
| Hz | Hertz |
| kN | kilonewton |
| kV | kilovolts |
| mA | milliampere |
| mm | millimetre |
| MPa | megapascal |
| MW | megawatt |
| nm | nanometre |
| px | pixels |
| rpm | rotation per minute |
| wt.% | weight percentage |

# 1 Introduction

## 1.1 Motivation and Background

White etching cracks (WECs) are a contact fatigue mechanism that initiates subsurface in steel bearings due to heavy local stress and plastic strain consisting of a microcrack bordered by a microstructural alteration. The crack eventually evolves into the failure mode called White structure flaking (WSF) causing premature failures. The name of the microcrack is given by the microstructural alteration that appears white in light optical microscopy (LOM) after etching [1–3], illustrated in Figure 1.1.

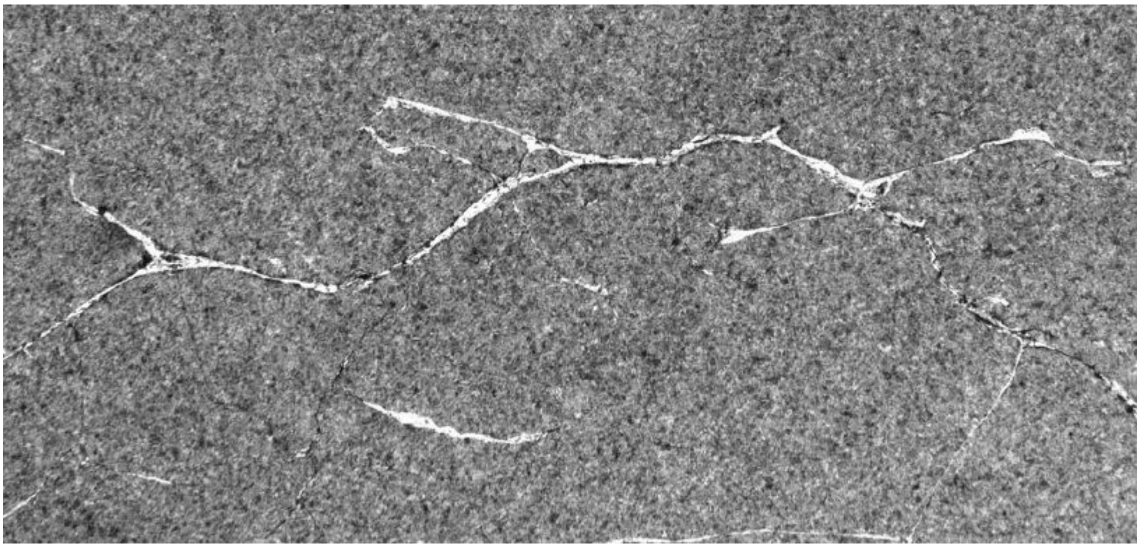

**Figure 1.1.** WEC network in steel. [4]

Premature failures due to WECs commonly occurs in gears and bearings in wind turbines and propulsion systems. They have become especially problematic since ambitious energy targets has pushed for a significant growth of wind power capacity [5]. The challenge to increase the power density has increased the size of wind turbines creating a demand for better materials and designs to increase reliability. More windfarms are established offshore to reduce visual and acoustic impact on nature and people. Their location makes operation and maintenance costs high due to transport and limited possibilities of remote condition monitoring [6]. WEC damage is most critical to the Wind Turbine Gearbox (WTGB) which never reaches its anticipated lifespan of 20 years, and has average repair price of €230,000 [7].

The WEC mechanism has yet to be completely understood and has become an urgent research topic to reduce cost of wind energy. Traditionally, investigations has focused on fully developed WECs from failed bearings where it can be difficult to determine the initiation and propagation processes. Lately, there has been more focus on the initiation stage, there is still unanswered questions regarding the propagation mechanisms and the effect of the microstructural alterations.

## 1.2 Aim and Scope of the Work

The thesis is part of the AEMON [8] project aiming to reduce operation and maintenance costs by developing a new monitoring system to be used on gear systems in marine vessels and wind turbines. Acoustic emission will be used to detect damage such as WECs in gears that other monitoring systems cannot detect [8]. An important part of this project is to understand the propagation mechanisms of WECs by characterisation of WECs, which is the focus of this thesis.

These investigations are a continuation of previous work done in the specialization project [9] where portions of the theory still is applicable. A summary of the results from the project thesis are included in this thesis as their own section because supplemental work on the specialization project was completed during the master thesis and they are used for comparison purposes in the discussion. The aim of this thesis is to increase the knowledge of the microstructural alteration, propagation and initiation causes and drivers in WECs. This is done through investigations of a through-hardened steel bearing by analysing the chemistry, microstructural features and mechanical properties through advanced material characterisation techniques. The results are compared to the earlier work on a case-hardened steel.

The key objectives of this thesis are to:

- Carry out a literature review with state-of-the-art knowledge of WECs including initiation and propagation mechanisms.
- Investigate the microstructure through advanced characterisation techniques such as Scanning Electron Microscopy (SEM) combined with Electron Backscatter Diffraction (EBSD) and Backscatter Electron (BSE) imaging.
- Investigate the chemistry of inclusions, altered microstructure and parent material through Energy Dispersive X-ray Spectroscopy (EDS) and Electron Probe Micro Analyzer (EPMA).
- Perform nanoindentation hardness measurments on the altered microstructure and parent material.

- Compare characterisation results of through-hardened steel with results from case-hardened steel investigated in the author's project thesis.

# 2 Previous results

This section will shortly summarise the results and discussion from the author's project thesis [9] in order to compare results from case-hardened steel with the results from the through-hardened steel investigated in this master thesis. In addition to these results, some further work was done on the sample during the author's master thesis, and the result from this experiment will be presented in Section 5.

## 2.1 Material and test procedure

The investigated material was an 18CrNiMo7-6 case-hardened steel, which consists of 0.15-0.19 wt.% carbon, but the surface is carburized with approx. 1 wt.% carbon. To induce WECs, the examined material was run in a high frequency rolling contact fatigue test machine, which is schematically shown in Figure 2.1. The test specimen was 60 mm wide and had a diameter of 115 mm. At three places separated by 120 degrees, the test specimen was loaded with rollers. The rollers were 115 mm in diameter and had a radius-controlled contact surface of 3750 mm. The testing device could apply maximum contact stress of 2200 MPa and could rotate at a maximum speed of 500 RPM. The current test had a 91 kN applied load, and it lasted 10.5 million cycles at a frequency of 14 Hz. Hertzian stress calculations positioned the maximum shear stress at a depth of 792 $\mu$m below the surface, with a shear stress of 603 MPa.

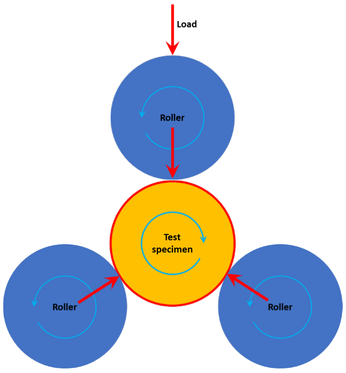

**Figure 2.1.** Schematic diagram of the test rig.

## 2.2 Initiation and propagation

The investigated sample contained a crack extending over 2300 $\mu$m as shown in the Light Optical Microscopy (LOM) images in Figure 2.2. The maximum shear force was calculated to be 792 $\mu$m below the contact surface while the crack was located at a depth of 2800 $\mu$m below the surface. Crack propagation appears to have propagated nearly parallel with the contact surface, but with a small incline. In Figure 2.2 the further investigated area A3 is marked with a square and arrows pointing to voids along the crack. Approximately in the centre of the crack, the third arrow from the left, a large void can be observed. Initial LOM investigation revealed a feature in this position assumed to be a non-metallic inclusion. The composition of the inclusion could not be tested since they disappeared after vibration polishing during sample preparation. This inclusion could be a potential initiation site for the crack propagation, which correlate with other findings that WECs propagate from and through inclusions [10]. Other voids could also be a result of missing inclusions, accumulation of vacancies due to mechanical loading or volume decrease since ferrite has a higher density than martensite [11]. The crack was found to have a transgranular propagation through the martensitic microstructure.

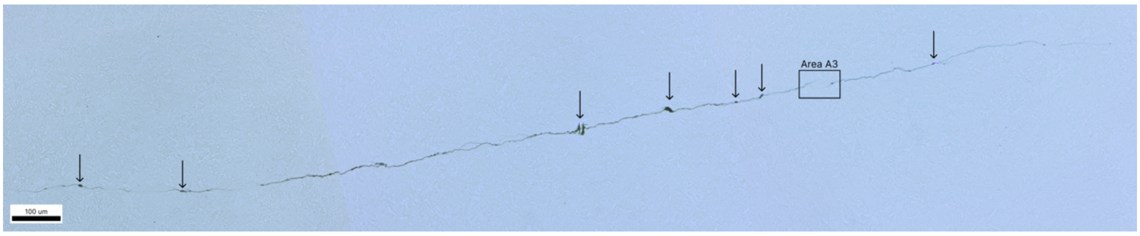

**Figure 2.2.** Optical micrograph of the crack network in the circumferential plane on a vibration polished sample. A black square indicates the further analysed area, called 'A3', and black arrows points to voids along the crack.

## 2.3 Microstructure

In LOM and SE-SEM two microstructures could be observed. In the bulk material a plate like microstructure and a smooth microstructure adjacent to the crack, respectively hypothesised to be martensite and nano-grained ferrite i.e. WEM. The microstructure of area A3 was further characterised by EBSD and BSE analysis. The EBSD results are presented in Figure 2.3. The result in Figure 2.3 a) confirmed that the bulk material consists of a $\alpha$-ferritic plate like structure i.e. martensite. The observed smooth area did not display an unambiguously signal, which supported the nano-grained ferrite hypothesis because the grains would be too small for the scanning volume of the EBSD signal. Some fine grains in the top part of the WEM could be observed. These had a lower dislocation density, which corresponds to the fact that ferrite has smaller dislocations than martensite, according to Grain Average Missorientation (GAM) analysis presented in Figure 2.3 c). From Figure 2.3 b) it can be observed that the transformation from martensite to WEM can be abrupt without any gradient or alterations in the martensitic structure.

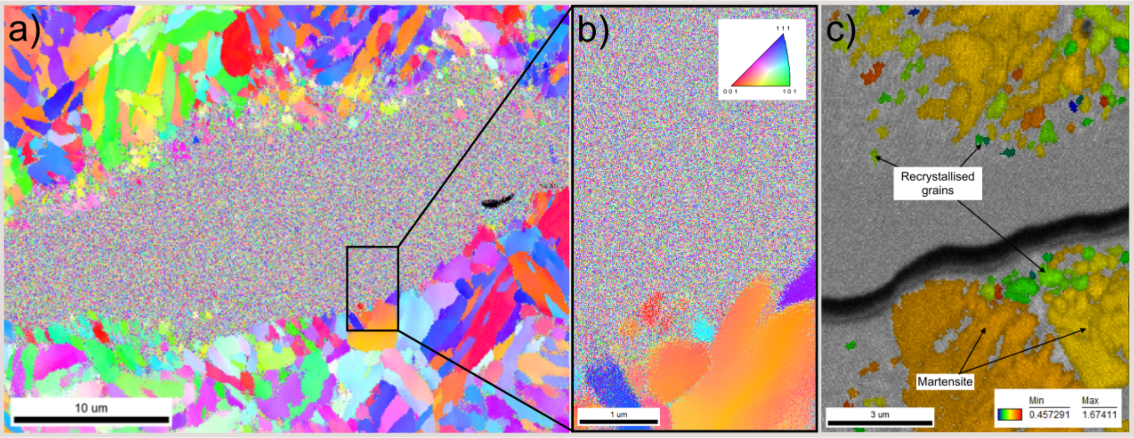

**Figure 2.3.** EBSD analysis of WEM in area A3. a) IPF of the investigated area with a black rectangle showing the position of the IPF image in b). c) GAM data of martensite and recrystallised grains in the transition between martensite and WEM.

The BSE results presented in Figure 2.4 further confirmed the theory that the smooth areas consisted of nanocrystalline grains. Figure 2.4 a) showed that the WEM consisted of grains of different sizes, coarse marked with green, fine marked with blue and nano-crystalline marked with orange. The different categories of grains also seem to be gathered in horizontal bands. A high-magnification BSE image is presented in Figure 2.4 b) where arrows point to darker spots in the structure which seem to be parallel to the crack. Morsdorf et al. [12] have found voids similar to this which they suggest to be a proof of their moving crack theory[12].

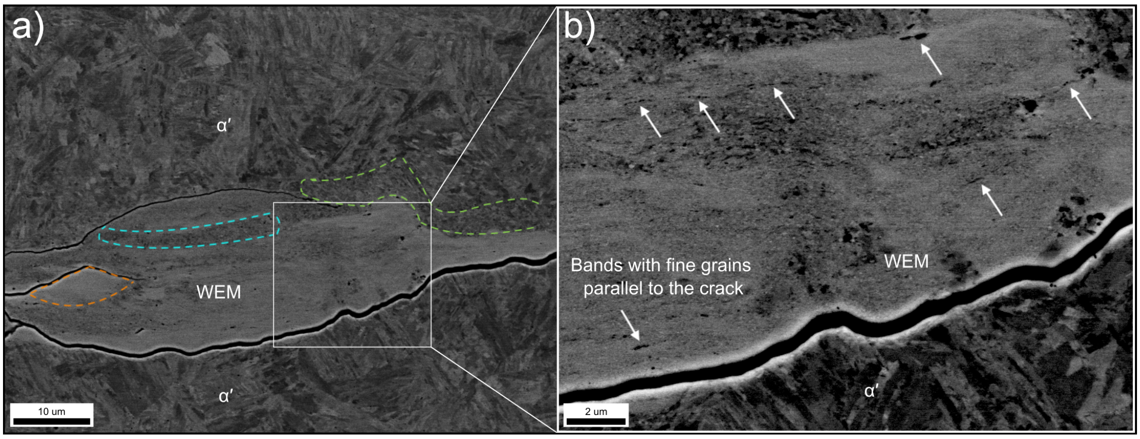

**Figure 2.4.** BSE and EPMA carbon analysis of WEM in area A3. a) BSE image of the A3 area, where coarse, fine and nano-crystalline grain structure is marked in respectively green, blue and orange. b) BSE image showing the nano-grained structure neighbouring the crack with arrows pointing to darker spots aligned in a direction parallel to the crack.

## 2.4 Mechanical properties

Figure 2.5 shows the nanoindentation property mapping. The colours in the heatmap in Figure 2.5 c) clearly show a significantly higher hardness in the WEM than in the martensite. Previous point indentations by Anette Brocks Hagen had shown that the WEM had a hardness of 10.2 ± 2.0 GPa and the matrix had a hardness of 5.2 ± 0.7 GPa. The increase in hardness is attributed to the grain refinement in the WEM.

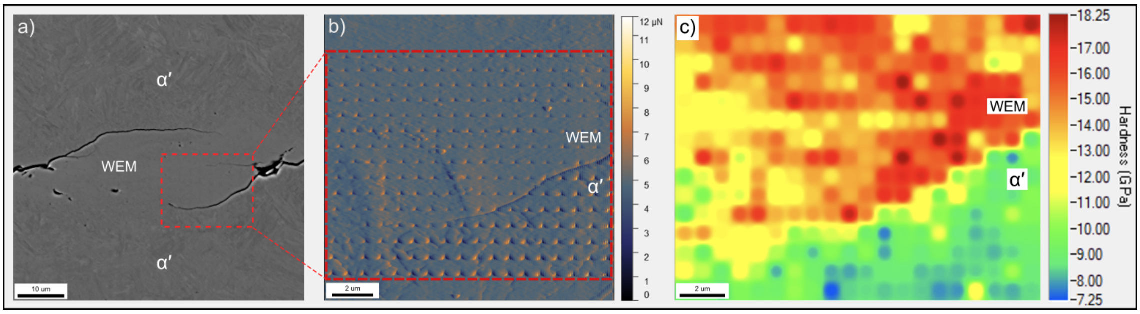

**Figure 2.5.** Nanoindentation property mapping with a) showing a SE-SEM image of the A3 area with a red square indicating the position of the mapped area, b) a SPM image of the indented are after mapping and c) a hardness heatmap.

# 3 Theory

This section will firstly give a brief overview of steel, how it is produced and how this leads to inclusions, voids etc., before an overview of the different phases and microstructures that are relevant to this thesis. Secondly, typical rolling bearing elements, bearing steels and rolling contact fundamentals are introduced. Following, is a detailed review of white etching cracks and their initiation and formation processes, focusing especially on white etching matter and its microstructural change from the parent material.

## 3.1 Steel

### 3.1.1 Production

Steel consists of a combination of iron, carbon and other alloying elements, where the carbon content is lower than 2 wt.% [13]. Steel is produced by reducing iron oxide with carbon into something called pig iron, which has a high carbon content at 2-4 wt.%. From pig iron, steel is made by removing some of this carbon by adding oxygen and limestone, also removing other contaminants such as sulphur, silicon, phosphor and manganese. The carbon and impurities are turned into oxides that can be removed from the steel as a slag. Simultaneously, alloying elements such as molybdenum, manganese, chromium, nickel and wolfram are added as needed depending on the application of the steel product. After removing the slag, there is a high oxygen content in the melt. If the steel is cooled down with the high oxygen content CO-pores will be made in the steel from the oxygen because the solubility of oxygen decrease. The steel is therefore deoxidised by adding silicon, aluminium or manganese. The air may also pollute the steel with nitrogen which may be removed by adding aluminium which creates nitrides [13].

### 3.1.2 Inclusions

All debris of slag can not be removed from the metal melt during production [13]. Non-metallic inclusions will therefore be present in the final material, which only has a negative effect on its performance. The non-metallic inclusions are either a result of the deoxidation process or slag from the lining in the furnace, which contains $Al_2O_3$ and $SiO_3$. The resulting non-metallic inclusions can be divided into two categories: ductile and brittle. Ductile inclusions can be physically deformed during hot rolling, making them stretch and get pointy ends. A common ductile inclusion is sulfides, ex. manganese sulphide (MnS). Brittle inclusions break into smaller pieces when processed, and are often found as clusters of particles. Examples of brittle inclusions are oxides and aluminium-manganese-silicates [13]. Illustrations of both types of inclusions are shown in Figure 3.1.

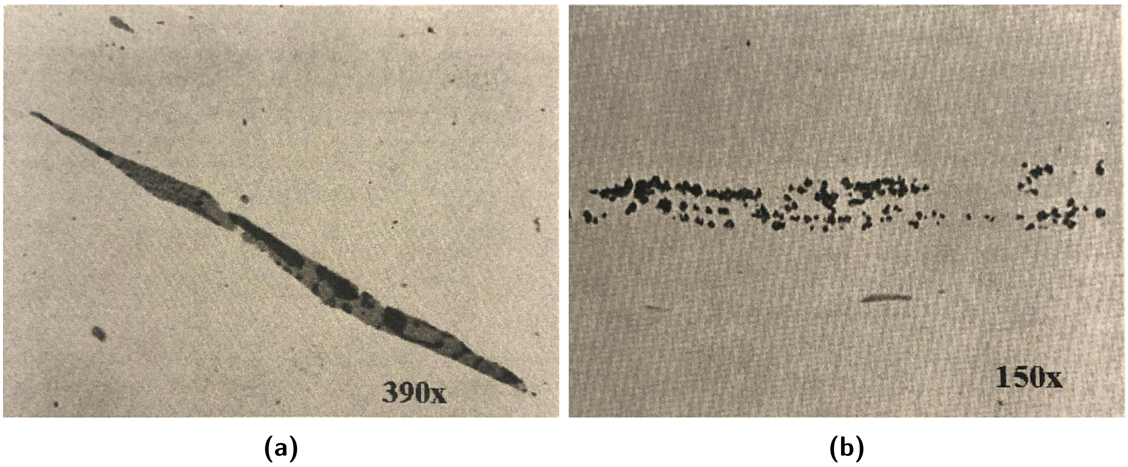

**(a)** **(b)**

**Figure 3.1.** Slag inclusions [13]. a) Ductile MnS-slag in hot rolled steel. b) Brittle $Al_2O_3$ in steel oxidized with aluminium.

### 3.1.3 Phases and microstructures

Five different phases can be found in steel: ferrite, cementite, graphite, martensite and austenite [14]. Also, microstructures that contain a combination of the mentioned phases can be found in steel, such as pearlite, bainite, spheroidite, ledeburite etc. The phases and microstructures relevant to this thesis are further explained below.

Ferrite, also called $\alpha$-ferrite, is a phase that consists of a body-centred cubic (BCC) structure, as shown in Figure 3.2. The structure has little room for interstitial sites, and can only dissolve up to 0.005 wt.% carbon at room temperature [15]. The ferrite phase only exists at temperatures below 912 °C. Ferrite can both be magnetic at temperatures below the Curie temperature 570 °C and non-magnetic at temperatures above the Curie temperature [14].

Austenite, also called $\gamma$-phase iron ($\gamma$-Fe), consist of a face-centered cubic (FCC) structure, shown in Figure 3.2. Austenite is found at temperatures above 723 °C, but can also be found as retained austenite by alloy additions such as nickel and manganese at room temperature. Austenite can dissolve considerably more carbon than ferrite, as much as 2.03 wt.% at 1146 °C [14].

Cementite, also called iron carbide, consists of an orthorhombic crystal structure with the formula $Fe_3C$. The structure dissolves a lot of carbon, 6.67 wt.%, and forms a brittle and hard material which is used as a strengthener in steel [14].

Martensite consists of a body-centered tetragonal (BCT) structure, shown in Figure 3.2. The BCT structure has the same crystal structure as the BCC structure, but it is elongated in one direction. Martensite is formed in steels that have a rapid cooling rate from austenite, in a diffusionless shear transformation. The transformation results in large shears, volume expansion and high dislocation densities, where carbon atoms remain as interstitial impurities in the martensite, shown with Xs in the BCT unit cell in Figure 3.2. The martensite is created as thin plates or laths to minimise the strain energy, and it is very hard due to the strain the interstitial carbon adds to the structure [14].

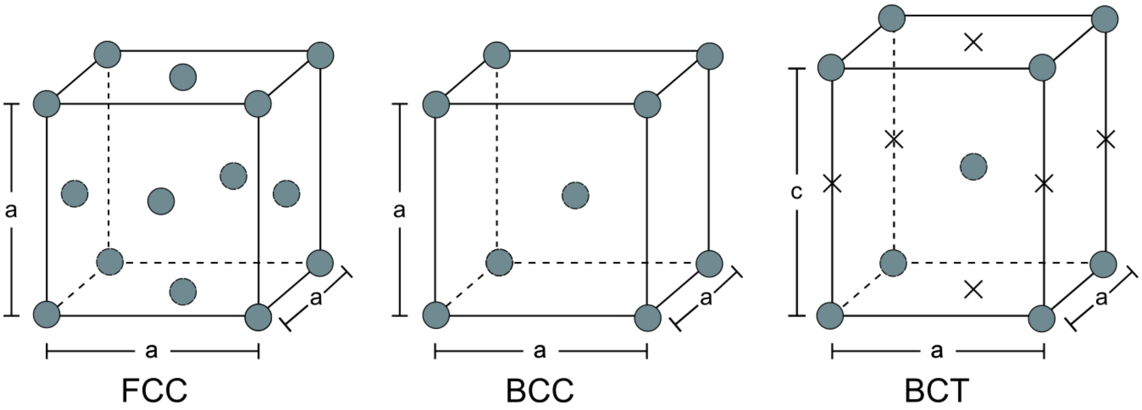

**Figure 3.2.** Illustrations of the face-centred cubic (FCC), body-centred cubic (BCC) and body-centred tetragonal (BCT) unit cell. Iron atoms are shown as circles while interstitial sites that may contain carbon are marked with X.

## 3.2 Rolling element bearings

### 3.2.1 Introduction

Rolling element bearings provide rotational freedom while transmitting load between two structures in relative motion [16]. Rolling element bearings usually consist of an inner and outer race that moves relative to each other, illustrated in Figure 3.3. In machine parts the outer race is usually attached to the housing while the inner race is attached to the shaft, making it possible to rotate the shaft without rotating the housing. Between the races rolling elements provide the rotational freedom with low frictional resistance since sliding is replaced by rolling. A cage usually separates and keeps the rolling elements in place between the races [16].

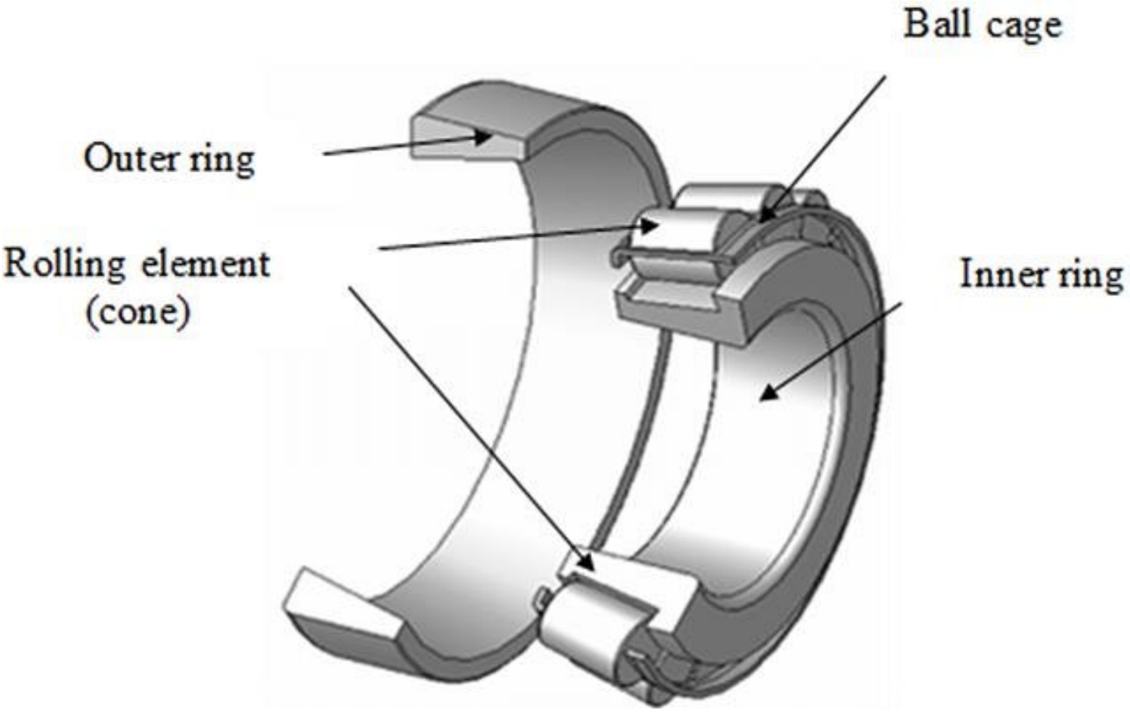

Figure 3.3. Schematic illustration of a tapered roller showing the main components in a bearing. Illustration from Malega et al. [17].

There are a number of different types of rolling bearings categorised based on the shape of the rolling elements. Some of the most common rolling element shapes include ball, cylindrical roller, spherical roller and tapered roller, illustrated in Figure 3.4. The shape of the rolling element is chosen based on load, speed and lubrication requirements for each application. Balls are often used when the loads are smaller. Shapes with a larger surface area, such as cylindrical, spherical and tapered rollers, are used when the loads are higher. A double row arrangement can also be used to increase the load capacity.

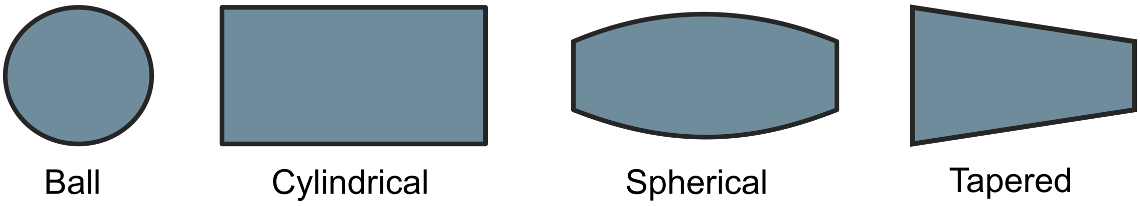

Figure 3.4. Cross-section of rolling elements used in bearings.

### 3.2.2 Bearing steels

Bearings have to withstand severe static and cyclic loading in difficult environments, such as in offshore windmills. The materials used in bearings require good rolling contact fatigue (RCF) resistance, wear resistance and creep tolerance [18]. The bearing steel could also be made corrosion resistant, but often sealing systems are used instead to cut the cost of corrosion resistant steel. Traditionally two types of steels have been used for bearings; through-hardened steels and case-hardened steels. Through-hardened steels have been hardened all the way through the bearing section into a martensitic or bainitic structure. Case hardened steels have a softer core while the surface layer is carburised and hardened into a martensitic structure.

Through-hardened steels, such as AISI 52100, are used for small bearings that have sufficient hardenability to obtain a martensitic structure throughout the bearing section. The steels contain carbon in the concentration range 0.8-1.1 wt.% and a total substitutional solute content below 3 wt.%. The steel is produced by austenitisation before quenching and low-temperature tempering. During austenitisation, the steel is heated to ∼1040 °C until the cementite is dissolved and the microstructure is fully austenitic i.e. face-centred cubic (FCC) configuration. Controlling the austenite grain size is important to reduce the probability of microcracking which can occur when the austenite grain size is too large. This can be controlled by the temperature and austenitisation time. After austenitisation, the steel is quenched in oil or salt. When the material is quenched the austenite transforms into body-centred tetragonal (BCT) martensite in a diffusionless shear transformation. The transformation requires a high cooling rate that does not allow for the diffusion of atoms. The microstructure will also contain 3-4 % cementite particles that had not dissolved during austenitisation and 6 vol.% of retained austenite. Further, the martensite is tempered at 160 °C to decompose some retained austenite and precipitate some carbides from the supersaturated martensite. After tempering, the steel softens if subjected to a temperature above 200 °C for a prolonged time, which limits its maximum service temperature [18].

Case hardened steels are used for larger bearings that do not have sufficient hardenability to produce martensite throughout the material. Due to the large dimensions, only a fraction of the surface is heavily loaded, which only necessitates the hardening of this zone. The steel originally holds a lower carbon content than ex. through-hardened steels, at 0.13-0.20 wt.%. The surface layer is then carbonated, which takes place in a carburising atmosphere which holds a temperature of 850-950 °C for 2-10 hours. During carburization, the austenite in the top ∼1 mm of the surface absorbs carbon and 3-4 wt.% carbides are formed. After carburization, the steel is quenched and the carburized zone is transformed into BCT martensite because of the rapid cooling. In the core the cooling is slower the atoms are able to diffuse during cooling creating a bainitic core, which consists of ferrite and cementite phases [18].

### 3.2.3 Rolling Contact Fundamentals

Heinrich Rudolf Hertz established in 1882 a model for contact mechanics based on the theory that two surfaces in contact will deform elastically [19]. The theory states that a contact area is created between two non-conformal surfaces due to elastic deformation. Without elastic deformation, the contact would happen at one point, resulting in an infinite pressure between surfaces causing automatic yielding. Hertz developed analytical formulas to calculate the stresses acting on the surfaces in these contacts called Hertz's Theory. Hertz's Theory is used to calculate the contact stress in many engineering applications where the non-conformal surfaces result in small contact areas and high contact pressures, including rolling bearing elements, gears, cams and seals etc. The theory is theoretically limited to static conditions, but it is still used in applications where the load is normal to the contact surface and there is no traction force present, such as roller bearings [20].

Between a ball and an inner race in a rolling element bearing the contact area is an ellipse, illustrated by Figure 3.5 a). Below the contact surface, there are normal ($\sigma$) and shear ($\tau$) stresses due to the contact pressure. The normal stresses are at a maximum at the surface, principal plane, decreasing with depth below the surface. The shear stress is zero in the principal plane, therefore also zero at the surface. The maximum shear stress is found subsurface at some depth below the surface. The normal and shear stresses are illustrated in Figure 3.5 b). During lubricated rolling, the contact stresses are affected by the rolling, the lubricating film that separates the surfaces and some degree of sliding. These factors have their separate effects on the contact mechanics. Rolling does in general create a larger contact area while sliding causes shear to act along the surface moving the maximum shear stress towards the surface [20].

The rolling contact fatigue (RCF) life of a bearing is often given as the $L_{10}$ life, which is the lifetime before 10% of all the bearings in one bearing selection have failed. Models predicting the lifetime of bearings at any load have been developed. One version is Lundberg and Palmgren's [21] relationship that uses the life for standard load in relationship with the applied load:

$$L = \frac{C^p}{P} \tag{3.1}$$

Where L is the fatigue life in revolutions x$10^6$, C is the standard load, P is the applied load and p is a constant which is 3 for ball bearings and 10/3 for roller bearings.

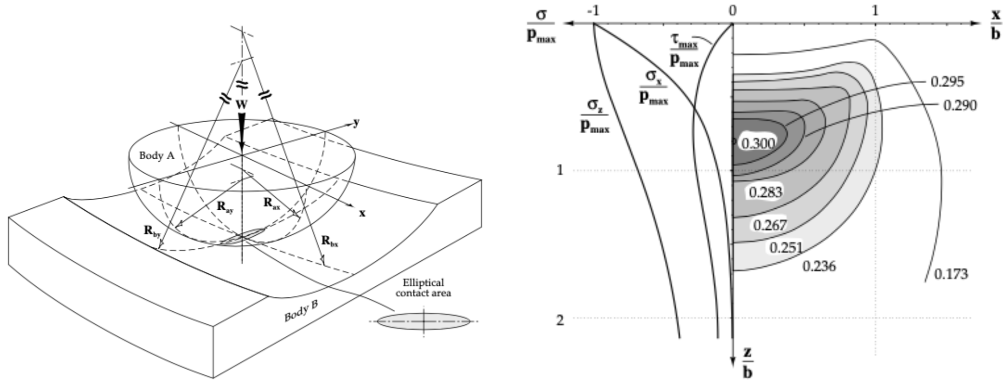

**(a)** **(b)**

**Figure 3.5.** (a) Geometry of contact area between a convex and concave surface, (b) stress fields of a static Hertz contact between two cylinders. Illustrations from Stachowaik et al. [20].

### 3.2.4 Wind turbine bearing operating conditions and failure

Most bearing failures in wind turbines occur in the wind turbine gearbox (WTGB). Inside the WTGB there are approximately 15 bearings whose job is to increase the rotor input of 5 - 22 rpm to an output of 1000 - 1600 rpm allowing the AC generator to transform the mechanical energy into electrical energy [22]. The operating condition of the bearings is unfavourable because of the tribological and complex loading conditions the bearings experience, especially offshore. Common issues are among others gearbox oil overheating, misalignment, transient loads due to wind gusts, sliding between the race and rolling elements, torque reversals from the electrical grid and overloading [1, 15, 23–25].

In a few years, the size of wind turbines has had high growth to increase the production capacity. In 2012, when the last IEC standard on wind turbine gearboxes was published (IEC 61400-4:2012) [26], the capacity of the largest commercial wind turbine was 7,5 MW and the rotors blades had a diameter of 126 meters [27]. In 2021 Siemens Gamesa's has successfully tested a wind turbine with 14 MW capacity and rotor blades of 222 metres in diameter which will be available for commercial use in 2024 [28]. The rapidness of the size growth means that the materials and designs used in today's gear-boxes often are inadequate for its use, and lead to early fatigue and failure. The problems the wind industry faces have led them to have a more proactive approach to their maintenance needs, with more focus on condition monitoring and periodic maintenance schedules to reduce the potential of long and costly downtimes due to failures [29].

### 3.2.5 Microstructural alterations

The unfavourable operating conditions in wind turbine bearings can lead to a range of different failure modes, which include dark etching regions (DER), white etching bands (WEB), WEC and butterflies [30]. DER is denominated after deformed areas that appear dark when observed in LOM after nital etching. The dark colour is due to carbon mitigation towards dislocated regions, found around the maximum shear stress. The microstructure is characterised as tempered martensite and softens the material compared to the bulk microstructure [18, 30]. WEB appear within the DER microstructure and consists of bands with carbon depleted refined ferrite and is soft compared to the bulk material [4, 31]. Both these microstructural alterations appear after moderate to high loading cycles and do not induce premature failure, contrary to WEC and butterflies which will be further described in Section 3.3.

## 3.3 White etching cracks

### 3.3.1 Microcrack

White etching cracks (WECs) are the dominant reason for premature bearing failure in wind turbine gearboxes, called White Structure Flaking (WSF) [3]. WSF can be seen only after 1% of the bearing's expected lifetime, which is 20 years, but more commonly occurs after 5-10% of the lifetime [15]. If and when WSF occurs is therefore unpredictable, and can not be calculated with standard RCF life estimates. WECs can also be found in other applications than bearings, such as gears and railways [32]. The phenomenon was firstly named by Scott et al. [1] in 1966 and has been widely investigated in later years, much due to the problems it causes in the offshore wind energy sector.

The characteristic feature of the cracks is the White Etching Matter (WEM) that decorates the crack surfaces. The cracks are found at varying depths, but normally in the area of maximum shear Hertz stresses which usually can be found at a depth between 100-500 $\mu$m [2, 30, 33]. The crack network can be long, and contain branches. In the axial plane, WECs are often found parallel to the contact surface, while in the circumferential plane WECs are found with more vertical branches [34]. Transgranular propagation of WEC has also been found, suggesting that the crack propagation is not influenced by grain boundaries [30, 35]. WECs are believed to initiate due to Mode I fracture from stress raisers in the material, where the loading is normal to the crack growth direction. Further crack propagation is governed by Mode II/III shear loading [34, 36].

Failure due to WEC has been reported in many types of steels, such as high carbon steels, low alloy bearing steels (ex. AISI 52100) [2, 15], graphite steels [37], high carbon chromium steels [37], tool steels [38], bainitic 100CrMo7-3 [39] and 18CrNiMo14-6 [33]. Common for these steels is that they are high carbon steels, while high nitrogen bearing steels such as X30CrMnN15-1 where nitrogen partly substitutes carbon has no reports of WEC, which indicates that carbon may be an important factor in WEC formation [40]. In the last few years, there has therefore been more focus on the effect of carbon during the formation of WECs [41–43].

Differences in the crack propagation in through-hardened and case-hardened steels have been investigated [44]. Trough-hardened steels were found to fail by axial cracks that propagate radially through the bearing. Case hardened steel is divided into two categories, steels with more and less than 20 % retained austenite. Steels with more than 20 % retained austenite were found to be immune to WEC, while steels with less than 20 % retained austenite displayed long subsurface crack networks that in the end propagates towards the surface resulting in macro pits from flaking [44].

### 3.3.2 White etching matter

The main factor that characterises WECs from other subsurface cracks is the White Etching Matter (WEM), also called White Etching Area (WEA), surrounding the crack surfaces. The WEM consists of a nanocrystalline ferritic microstructure which is almost equiaxed. The fine grains have a diameter between 5-100 nm, and the coarser grains are often found in the transition between WEM and matrix. When etched, the ferritic microstructure of the WEM has a higher etching resistance than the microstructure of the matrix and therefore appears white in LOM [15, 45, 46]. The WEM is usually heterogeneously distributed around the crack surfaces, mainly on crack faces in a more parallel direction to the contact surface [44]. WEM is also often only positioned at one side of the crack [47]. Inside the WEM fine structural features, voids, cavities, amorphous areas and elongated grains can be found, while it is free from carbides. The lack of carbides is likely due to dislocation gliding triggered by the cyclic Hertzian stresses dissolving the carbides [48]. The hardness of WEM is usually found to be 30-50 wt.% harder than the parent material, which is attributed to a combination of fine grains, a high carbon content resulting in dispersion of very fine cementite particles and high dislocation densities due to plastic deformation [15, 46]. The relationship between grain size and hardness can be described mathematically by the Hall-Petch relationship, where $H_0$ and $K_H$ are constants and $d$ is the grain diameter [14].

$$H = H_0 + K_H d^{-1/2} \tag{3.2}$$

There have been found few variations in WEM microstructure between different steel grades, however, Gould et al. [49] found that the WEM in case hardened steels were wider than for through-hardened steels. The authors suggested this to be due to either a lower crack propagation rate in case hardened steels leading to a larger number of contact cycles and more localised energy creating WEM, or inherent compressive residual stresses increasing the amount of rubbing between the crack faces [49].

WEM is normally developed in a martensitic, perlitic or bainitic matrix. Recrystallisation from the matrix microstructure into nanocrystalline ferrite requires grain refinement, which only can happen because of i) thermally induced recrystallisation or ii) deformation along with dynamic recrystallization. Thermally induced recrystallisation requires a temperature of 900 °C while the standard operating conditions of a bearing are less than 90 °C, which makes the only possible formation mechanism severe plastic deformation [12]. Different theories of how severe plastic deformation can produce WEM is given in Section 3.3.4.

Ferrite can be hard to distinguish from martensite and cementite since their electron diffraction can coincide, but Selected Area Diffraction (SAED) patterns have identified WEM as nanocrystalline ferrite that is supersaturated with carbon. Ferrite is known to be a bad solvent of carbon, only 0.005 wt.% in solid solution, while WEM usually has a higher carbon content. However, more recent APT investigations have shown that instead of being dissolved in the ferrite grain the carbon is segregated at the grain boundaries. Through Electron Probe Microanalysis (EPMA) investigations, Curd et al. [47] found that within a WEM there are both areas of carbon enrichment and depletion compared to the matrix. Further, the APT investigations of Mayweg et al. [41], which are shown in Figure 3.6, found that the carbon content highly influences the grain size within the WEM. They found that areas with higher carbon content have finer grains while areas that have less carbon content have larger grains, which also corresponds with the work of Li et al. [50] and Danielsen et al. [51].

As mentioned, investigations of Curd et al. [47] showed a larger degree of carbon depletion, which raises the question of where the "missing" carbon is. APT investigations of Mayweg et al. [42] also found a general carbon depletion in WEM, but they also found a carbon film at the crack surfaces. They suggest that the carbon film reduces friction between the crack surfaces, and increases crack tip displacement

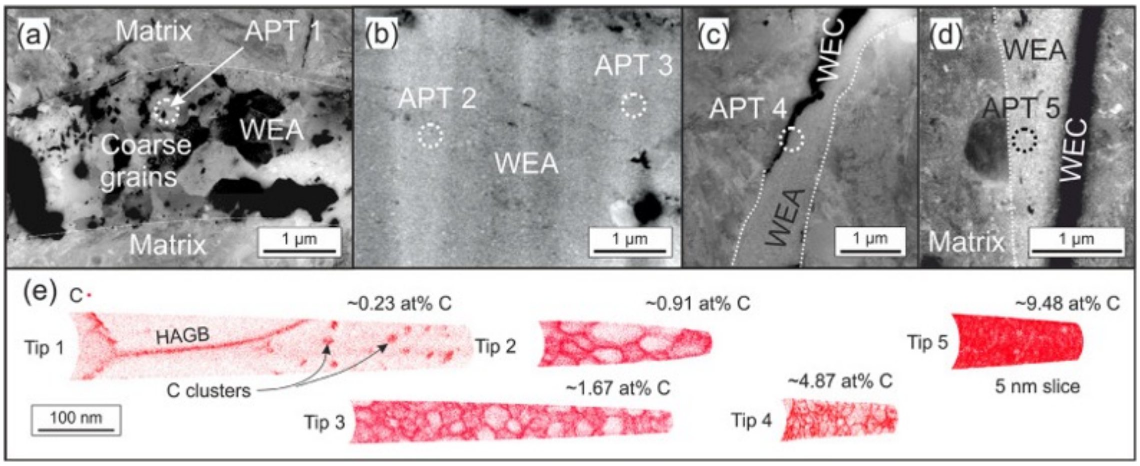

**Figure 3.6.** APT results from Mayweg et al. [41] showing segregation of carbon on the grain boundaries in WEM.

which results in accelerated crack propagation [42].

### 3.3.3 WEC vs. butterfly

Damage that is often mentioned in relation to WECs due to the many resemblances are butterfly cracks (or butterflies) [52]. In likeness with WECs, butterflies are created near the raceway surface in bearing steel due to cyclic stresses during RCF. They initiate at material imperfections which act as stress raisers, such as non-metallic inclusions, defects and second phases. From the material imperfection, two cracks together with a microstructural change consisting of WEM form the feature which resembles butterfly wings, as shown in Figure 3.7. The cracks have a length between 10-100 $\mu$m. They are believed to initiate due to concentrations of unidirectional shear stress, which is found at an angle of 45° compared to the surface. Butterfly cracks therefore propagate between 30-50° and 130-150° from the initiation point compared to the over-rolling direction [2, 3, 18, 31, 34]. Additionally, two smaller cracks, making a total of four cracks, can be created if the over-rolling direction is changed [53].

Butterflies are mainly found to form at inclusion made of sulphurs, oxides ($Al_2O_3$) or dual-phase inclusions made from sulphurs and oxides. At MnS and MnS/$Al_2O_3$ inclusions, butterflies have been found to always initiate from inclusions that have cracked along the direction of the major axis, making the inclusion the butterfly initiator [3]. Butterflies are divided into two categories: 1) those that do not continue to propagate and thus do not cause failure, and 2) those that do propagate and create WECs [3, 54].

The microstructure of the WEM connected to butterflies is reported to be similar to the ones connected to WEC. It consists of a fine or nanocrystalline grain structure with increased hardness of 10-50 % [55]. The WEM is found to be carbon depleted compared to the matrix [55], similar to that of WECs, but in WEM in connection to WECs, there have also been found carbon enriched areas [47].

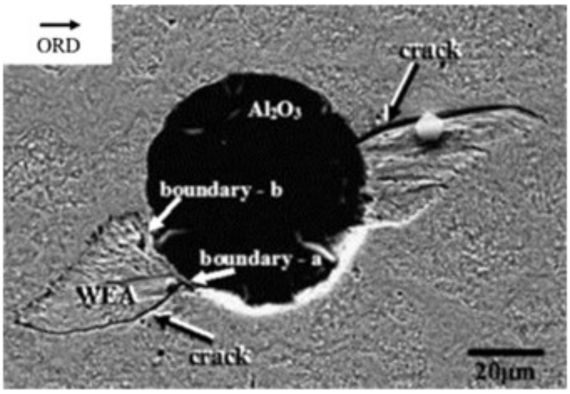

Figure 3.7. Butterfly crack, image from Grabulov et al. [56].

### 3.3.4 Initiation

A large number of investigations on WECs have led to several different theories of initiation mechanisms. While some theories are believed to be confirmed, this does not exclude the possibility that other proposed mechanisms may also be correct. The following section will outline some of the most common initiation hypotheses.

The suggested main categories of initiation hypotheses are surface initiation and subsurface initiation. The surface initiation hypothesis suggests that WECs initiate from microcracks and damage on the surface, which is created due to the high surface stress concentration creating ruptures in the lubricant film. From the surface damage, a crack propagates subsurface, and WEM forms on the surface creating a WEC [57, 58]. It has been shown that WEM only forms on crack faces when there is negative sliding, i.e. the traction force is in the same direction as the raceways moving direction [58].

The subsurface initiation hypothesis suggests that material defects and stress raisers in the maximum shear stress region are the cause of WEC initiation. The WEC will propagate into a subsurface crack network before it reaches the contact surface, leading to WSF and bearing failure. The stress raisers can be inclusions, voids, large carbides etc. Non-metallic inclusions, such as MnS and $Al_2O_3$, in a larger WEC network, several of these non-metallic inclusions can be found to interact with the crack, indicating that they also play an important role in WEC formation. Experiments on pre-cracked samples have shown that subsurface pre-cracked samples fail quicker than surface pre-cracked samples, which indicates that the WEC causing problems in WTGB are sub-surface cracks since damage occurs much earlier than RCF life predicts.

A fully developed crack network can span from the surface into the subsurface making the process of identifying the initiation point extremely difficult. However, when cracks are captured soon after their initiation it is easier to identify the initiation point and formation mechanisms. In recent years investigations, through serial sectioning methods and x-ray tomography, have provided a lot of evidence that subsurface cracks initiated on non-metallic inclusions are *one* of the initiation mechanisms [10, 59]. The non-metallic inclusions can not be totally removed from the material since they are by-products of the steel production process. Manganese is added to remove the sulphide in the steel, preventing the formation of iron sulphide which has a low melting point and can be problematic. Aluminium oxide can be found in steel due to the oxidising process. Both of these inclusions create different implications. MnS is a soft inclusion where debonding from the matrix and void formation is a potential crack initiation site. The MnS inclusion has also been found to crack, due to its lower plastic limit, where it continues to propagate into the matrix. The $Al_2O_3$ inclusions are hard compared to the matrix, and the hardness mismatch and poor coherence between the inclusion and matrix make it a good crack initiator. Dual-phase inclusions consisting of Mn, S, Al and O can also be initiation sites, and according to Gould et al. [60] this is a preferential initiation site for WECs, most likely due to the large size of the inclusion creating stress concentrations in the bulk material, thin shape applies severe stresses to the inclusion tip while there is a hardness mismatch between $Al_2O_3$ and the matrix.

There has also for many years been a discussion about whether WEM or microcracks form first, which can be hard to distinguish in fully developed crack networks. The latest publications in the field mostly agree that the microcrack is formed first, followed by WEM formation which will be explained in further detail in Section 3.3.5. This agreement is based on the fact that there is more evidence showing microcracks without WEM than there is WEM without microcracks. Contrary to this, Spille et al. [61] have observed WEM formation around subsurface voids in the early stages of WEM formation. The authors suggest that these pores can be *one* initiation point for WEC formation where WEM is followed by crack formation.

### 3.3.5 Formation

As previously mentioned, there has been a lot of debate whether WEM or microcracks are formed first, or if it is a cooperative growth. The researchers that suggest that WEM is formed first explain that the high strain from contact pressure leads to the transformation of WEM which again leads to cracking because of the hardness mismatch between the altered WEM and the surrounding matrix [61, 62]. The other group of researchers suggests that the crack develops first followed by WEM formation due to crack propagation [59, 63–66]. In recent publications, most authors' agree that the latter case is more likely (or common) which indicates that the general agreement at the moment is that the WEM is a result of a microcrack.

In addition to the debate around the two mentioned theories, researchers are not agreed on how the further propagation of the WEC and formation of WEM along it occurs. There are two main theories, i) the 'crack faces rubbing' hypothesis [12, 41, 42] and ii) WEM formation at the crack tips [47]. The 'crack faces rubbing' hypothesis suggests that the exposed crack faces are rubbed together during each cyclic loading. The stresses from the plastic deformation during each rubbing result in the phase transformation into nano-crystalline ferrite and dissolves carbon from carbides into a solid solution [40]. The critics of this theory believe the theory is questionable because WEM often is found on only one side of the crack or in very uneven amounts on each crack face [51, 60, 67, 68]. The other proposed theory is that WEM is generated ahead of the crack-tip due to the high stress concentration in this area. Since the WEM is harder than the matrix material this cracks easier and creates a preferential propagation path for the microcrack [47].

Morsdorf et al. [12] have proposed a suggestion to the reason why the 'crack faces rubbing' hypothesis is correct even though the WEM is only placed on one crack face. This is called the 'moving crack' theory and suggests that in addition to conventional crack propagation the crack moves normal to its plane. During cyclic loading, the crack faces rub together and crystallisation due to severe plastic deformation occurs and essentially welds the crack together. During unloading the crack reopens in a new position transferring material from one side of the crack to another. The theory is based on several findings inside the WEM, such as smooth crack surfaces, distribution of Cr and carbon, voids, cavities and partially rewelded cracks [12].

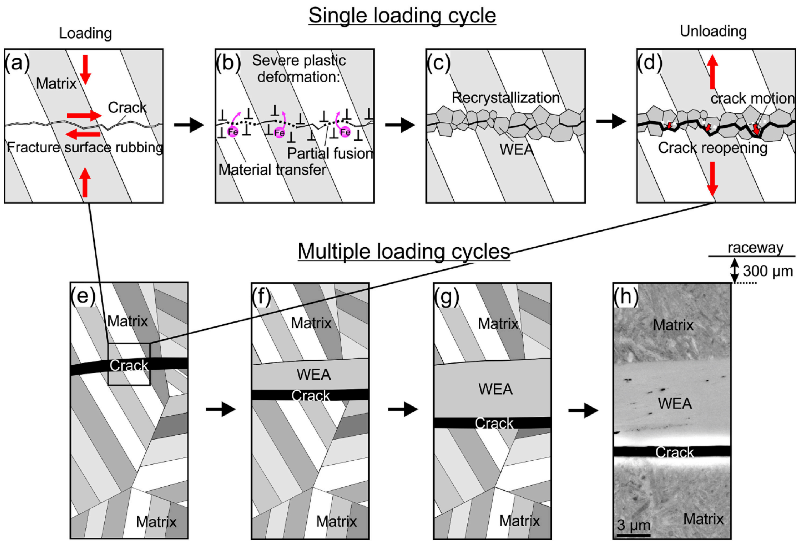

**Figure 3.8.** Schematic illustration from Morsdorf et al. [12] explaining the normal movement of WEC.

### 3.3.6 Drivers

Hydrogen diffusion [57, 69], heat treatment [70], lubricant [70, 71], electrothermal effects [2], transient loading conditions [2] and steel cleanliness [54, 60] are among the explanations proposed by researchers as drivers for WEC initiation and development. There are two factors that have been shown to drive WEC formation, i) the use of low-reference lubricant oil in combination with rolling-sliding conditions [54, 58, 67, 72, 73], and ii) defects in the material such as cracks, inclusions, rough surface and intergranular enbritlement [64, 66, 70].

Low-reference lubricants, also called 'bad lubricants', 'WEC critical oils' or 'WEC oils', are believed to induce hydrogen into the material causing WEC [15, 74]. A study by Newlands et al [75] found that gaseous hydrogen can evolve at lubricated contacts from oil or greases. Hydrogen is thought to diffuse into materials and become confined at material defects like inclusions. Higher hydrogen content at defects decreases the crack initiation threshold, allowing subsurface cracks to develop at low stress levels [57] because hydrogen promotes separation between inclusion and metal matrix and localised plasticity around defects. Franke et al. [69] found that the size of the contact area between the raceway and the rolling element influenced the hydrogen content in the matrix, where a large contact area and small free surface outside the contact area promote hydrogen diffusion into the matrix [69]. The source of the hydrogen still remains unknown, although it is thought to be either tribochemical lubricant breakdown caused by significant plastic deformation [76] or water contaminants in the lubricant [74, 77] due to condensation.

Lubricant additives, such as the extreme-pressure/anti-wear additive zinc dithiophosphates (ZDDP) and the corrosion protection additive dicyclohexylamine (DCHA), are thought to play a role in WEC formation by the formation of a tribofilm in the top 150 nm layer of the contact surface [78]. Warnik et al. [78] found the tribofilm to be thick and patchy in the incubation period, with varying friction properties from patch to patch leading to high and inconsistent friction. The authors suggest that the high friction from the patchy tribofilm provides the energy needed to decompose the lubricant resulting in hydrogen formation, while this earlier has been suggested to be a result of the metal-to-metal contact [74]. The tribofilm contains a higher level of hydrogen transporting hydrogen from the surface into the subsurface high stress zone [57, 79], resulting in microstructural changes leading to WEC [61, 69, 78].

Residual electrical currents can be present in the gearboxes due to discharges from the generator, which makes it a possible WEC driver [46, 74]. Small electrical currents ($I < 1$ mA) have been found to favour the formation of WEC, where electrical current is suggested to promote WEC formation by promoting hydrogen diffusion into the material [80]. Studies have shown that WEC preferably occurs at the bearing ring connected to the negative pole of the current source. To explain why only the cathodic (negative pole) race is affected Loos et al. [80] suggest that the Volmer reaction solving hydrogen cations only takes place at the cathode. This limits the presence of hydrogen atoms to the cathode where they can be absorbed by the steel.

In contrast, high electric currents ($I > 1$ mA) have been found to provoke WEC failures in the anodic part due to increased wear at the electrical positive pole [81–83]. When the dielectric strength of the lubricant is exceeded it will cause electrical discharge events generating hydrogen radicals. The hydrogen radicals can be absorbed in both the anodic and cathodic rings, but fatigue happens earlier at the anodic part due to the increased wear [81, 83].

To produce WEC in accelerated benchtop testing conditions hydrogen pre-charged samples have frequently been used [71, 74, 77, 84, 85]. Ruellan et al. [57] investigated the effect of hydrogen pre-charging versus non-charged specimens, suggesting that WEC initiation differs between the two. Pre-charged specimens were found to easily form WEC in the centre of the maximum shear stress zone, while WEC initiation in non-charged samples happened after more cycles and at the edge of the contact region [57].

Even though hydrogen diffusion in the matrix is a commonly mentioned driver, there are examples where hydrogen diffusion is not one of the initiation mechanisms

[58], suggesting that hydrogen diffusion into the matrix is not the only possible driver. Other suggested drivers include transient loading conditions as a result of sudden changes in wind and generator-grid engagements. Another reported issue is high loading sliding ratios, which have been suggested to contribute to WEC failure. Normally the slide to roll ratio in a wind turbine gearbox is between 3-10 %, however, slide to roll ratios as high as 30-110% have been calculated to occur under certain conditions [86].

### 3.3.7 Prevention of WEC failure

To avoid WEC failure, the major drivers of WEC must be addressed, which include inclusions, slip and hydrogen diffusion. Richardson et al. [59] have shown that steel cleanliness is a critical factor in WEC formation. As mentioned, inclusions can not be totally removed from the steel, but it is possible to produce cleaner steel grades than what is normally used for bearing steels [54]. Also, the heat treatment of the steel could affect its WEC failure qualities. Case-hardened steel has been found to last twice as long as through-hardened steels [49], which is suggested to be due to their high surface hardness, and high compression residual stresses hindering crack growth and high retained austenite percentage making the steel ductile.

Minimising the access of hydrogen by using lubricants without additives that generate hydrogen is one suggested way of minimising the problem of hydrogen diffusion. Creating a coating that acts as a diffusion barrier has also been mentioned as a solution. Several studies have shown that the run time of bearings has increased through using a black oxide coating on the surface, and it is the most common solution to prevent WEC damage [84, 87, 88]. The coating also reduces the probability of chemical attacks, protects against corrosion and stabilizes the microstructure [88].

# 4 Experimental

This section introduces the sample material, the test procedure which introduced the WEC to the sample and the different methods and techniques used for microstructure characterisation. In this study methods such as Light Optical Microscopy (LOM), Scanning Electron Microscopy (SEM) with techniques such as Secondary Electron (SE) and Back-scattered Electron (BSE) imaging, Electron Backscatter Diffraction (EBSD) and Energy-dispersive X-ray spectroscopy (EDS), Electron Probe Micro Analyzer (EPMA) and Nanoindentation were used to analyse the WEM accompanying the WEC. Each of these methods is explained in detail in the following sections.

## 4.1 Material

The analysed sample came from a FAG 61908 bearing. The alloy composition was not given by the manufacturer, but the metal was investigated through a chemical analysis, which results are given in Table 4.1. From the analysis, it was concluded that the steel grade most likely is 100Cr6, which is through-hardened bearing steel which is intended for use in rolling contacts and high fatigue applications because of its high strength, hardness and cleanliness. The dimension series of rolling bearings have been standardized internationally, and the material to be used should follow the ISO 683-17:2014 - ball and roller bearing steels [89].

**Table 4.1.** Chemical analysis of steel bearing.

| Element | Fe | C | Si | Mn | Cr |
|---|---|---|---|---|---|
| Content [wt.%] | 96.55-97.30 | 0.90-1.05 | 0.15-0.35 | 0.25-0.40 | 1.40-1.65 |

## 4.2 Test procedure

The test set-up used to create the WECs in this study was a design based on a 'TE88 multi station friction and wear test machine', but modifications of this design resulted in a separate test rig with schematics presented in Figure 4.1. During testing the bearing was subjected to load from a screw located on the top of the bearing, and could be measured via the load cell. Around the outside of the bearing, a conductive outer ring delivered a controlled electrical current to the bearing and lubricant film. The conductive ring was installed to deliver a direct current between the two bearing rings to accelerate the WEC formation. The negative pole was attached to the outer race, while the positive pole was connected to the inner race. LD 75W-80 oil with ZDDP anti-wear additive was used as the lubricant. The unit was also connected to an acoustic emission (AE) sensor which as a part of the AEMON project was installed with the goal to capture signals from the WEC propagation. The finished test set-up could be performed at a temperature of 50 °C, with contact pressures reaching up to 1.9 GPa and 2000 rpm. To produce the WECs analysed in this study a load of 3.6 kN was applied to the bearing, the test ran for 250 h and a maximum current of I = 0.2 mA was applied.

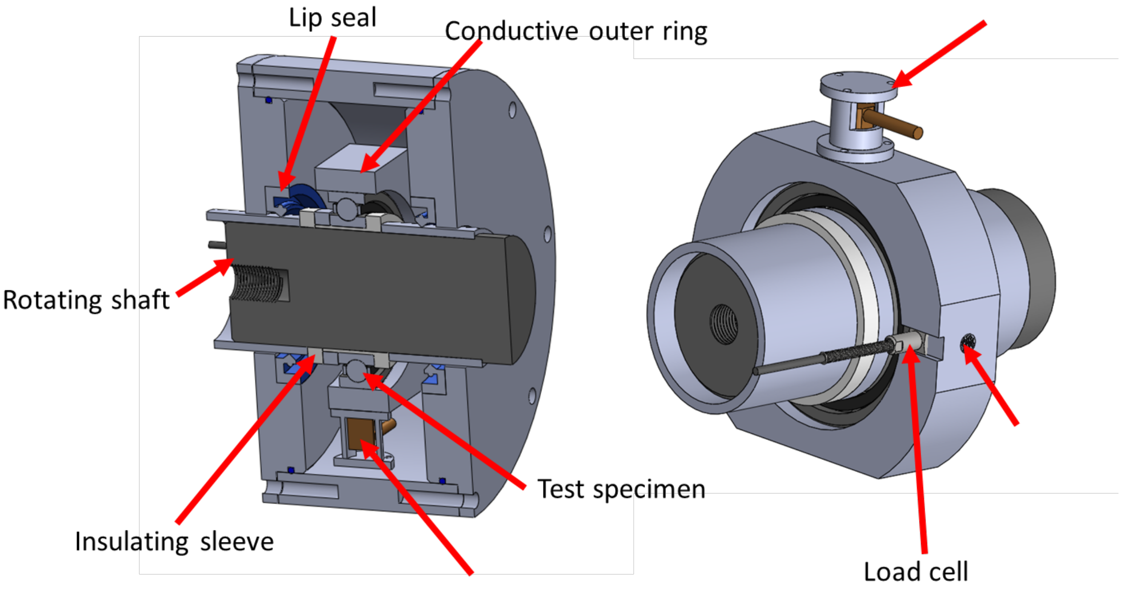

**Figure 4.1.** Schematic illustration of the ball bearing test rig.

## 4.3 Metallographic sample preparation

### 4.3.1 Case-hardened steel

Previous to the EPMA analysis on the case-hardened steel performed in this thesis the sample was vibration polished for one hour, with 70 % amplitude and 550 g weight with Buehler Vibromet 2, to remove any surface contamination due to previous SEM investigations.

During the work in the project thesis, the sample had been wet grinded with silicon carbide (SiC) paper and polished with diamond suspensions down to 3 $\mu$m and 1 $\mu$m. Further, it had been vibration polished for 16 hours with 70 % amplitude and 550 g weight.

### 4.3.2 Through-hardened steel

The inner and outer race of bearings that had been run in the test rig was cut in the circumferential plane in the middle of the ball grove. The sections were further mounted in a conductive resin and wet grinded with silicon carbide (SiC) paper and polished with diamond suspensions down to 3 $\mu$m and 1 $\mu$m. After this preparation step, the initial search for WECs and WEMs was conducted. When potential sites for further investigation were located the sample was vibration polished for 16 h with Buehler Vibromet 2, with an amplitude of 70 % and 550 g additional weight. Freshly from vibration polishing to reduce the possibility of contaminants the sample was investigated with EPMA. Prior to the EPMA analysis, the surface was coated with a carbon layer to increase conductivity. After the analysis, this layer had to be removed to do further analyses such as EBSD. In an attempt to remove the layer without polishing away too much of the areas of interest the ion milling technique was used, with a voltage of 5 kV and an angle of 70° for 30 minutes. Unfortunately, the milling resulted in significant surface topography. Therefore, a new round of vibration polishing was conducted to prepare the sample for further BSE and EBSD analysis. During this round of polishing the areas mapped with EPMA were polished away, and new inclusions had to be chosen for further microstructural analysis. A plasma cleanser was used to remove surface contamination and optimise the surface for the EBSD analysis.

## 4.4 Scanning Electron Microscopy (SEM)

Scanning Electron Microscopy (SEM) was used for multiple investigations, such as Back-Scattered Electron (BSE) imaging, Electron Backscatter Diffraction (EBSD) and Energy-dispersive X-ray spectroscopy (EDS), which will be explained in further detail. SEM produces images of a sample by collecting information from signals emitted from the sample after being scanned with a focused beam of electrons. The signals that are most frequently used are Secondary Electrons (SE), Backscatter Electrons (BSE) and X-rays, illustrated in Figure 4.2.

Secondary electrons (SE) are used to produce SE-SEM images which show the topography of the surface. When the electron beam hits weakly bounded electrons at the surface electrons are reflected inelastic at approximately the same angle as the primary electron beam hit the surface [90]. Operating conditions for SE-SEM imaging is given in Table 4.2

BSEs are used to produce images that can differentiate between phases and visualise

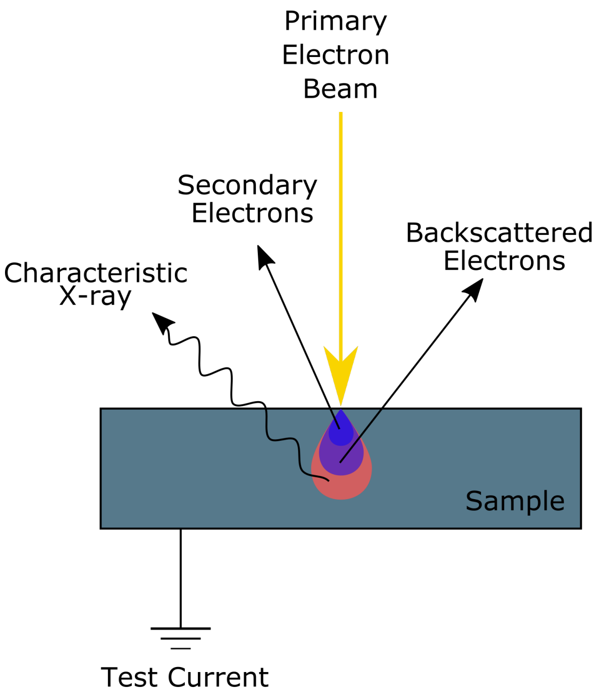

**Figure 4.2.** Signals that can be detected in SEM.

texture. The electrons are either elastically reflected when they hit the sample surface changing their direction more than 90° or after multiple elastic collisions with atoms underneath the surface. Phases can be differentiated from the signals because lighter atoms have a smaller atom core which will reflect fewer signals than heavier elements that have a larger atom core. The texture can be observed because some grain orientations reflect fewer electrons than others. The result is therefore a grey-scaled picture that is based on a combination of these signals [90].

Characteristic X-ray signals are used to find the chemical composition of the material. When an electron from the primary electron beam hits an atom it is ionised, meaning the electrons are excited into an energy state greater than its ground state. The electrons want to have as little energy as possible, and an electron will try to fill the vacant position from the excited electron. When the vacancy is filled an x-ray signal characteristic for the atom and the difference in shell position is emitted. These signals can therefore be used to differentiate between different elements [90].

### 4.4.1 Back-Scattered Electron (BSE) imaging

Back-Scattered Electron (BSE) imaging display microstructural features due to grain orientation and material composition. Material composition affects the brightness of the BSE image, where lighter elements appear darker than heavier elements because the atom core of heavier elements is larger and will reflect a higher amount of

**Table 4.2.** Parameters used during SE-SEM, EBSD, EDS and BSE imaging

| Parameter | SE-SEM | EBSD | EDS | BSE |
|---|---|---|---|---|
| Accelerating voltage | 10/15 kV | 21 kV | 10 kV | 10 kV |
| Working distance | 10 mm | 25 mm | 10 mm | 10 mm |
| Aperture | 120 $\mu$m | 300 $\mu$m | 120 $\mu$m | 120 um |
| Angle | 0° | 70° | 0° | 0° |
| High current mode | ON | ON | ON | ON |
| Dynamical focus | OFF | 0.3-1.1 % | OFF | OFF |

electrons intensifying the BSE signal. The detector used for BSE imaging is placed directly above the sample, and in this thesis, a Zeiss automatic BSE detector was used with the operating setting listed in Table 4.2.

### 4.4.2 Electron Backscatter Diffraction (EBSD)

Electron Backscatter Diffraction (EBSD) is a characterisation technique used to provide information about crystal orientation, structure, phase or strain in a material. During data collection, the polished sample is tilted 70 °C to be at an optimal angle compared to the EBSD detector. Other operating parameters are given in Table 4.2. Lines are created on a fluorescent screen, called Kikuchi bands, which hits the screen in different patterns depending on the orientation of the crystal. To index the pattern, Hough Transform is then used to detect the band positions from the pattern.

In this thesis, EBSD is used to obtain crystallographic information about the sample. The software NORDIF 3 was used to collect the EBSD data. The acquisition settings are listed in Table 4.3. Data was processed in EDAX TSL OIM Data Collection 7 and analysed in EDAX TSL OIM Analysis 7.2.

**Table 4.3.** Parameters used for acquisition in NORDIF 3 Software.

| Parameter | Acquisition |
|---|---|
| Averaging | 3 # |
| Speed | 300 fps |
| Resolution | 120x120 px |
| Exposure time | 3283 $\mu$s |
| Gain | 6 |

The EBSD data in this thesis is presented in form of maps, where the following four types are utilised.

### Phase map

Phase maps are used to identify phases by comparing symmetries in the EBSD pattern with symmetries of known phases in an EBSD library. In these investigations, the measured patterns have been compared to retained austenite (i.e. $\gamma$-Fe), martensite and ferrite (i.e. $\alpha$-Fe) and cementite. The BCC structure of ferrite is difficult to distinguish from the BCT structure of martensite, which normally results in martensite being indexed as ferrite. To differentiate between the two phases another mapping is used, as Image Quality (IQ) and Kernal Average Mapping (KAM).

### Image Quality (IQ)

Image Quality (IQ) maps describe the quality of the diffraction pattern by mapping from low to high intensity of the Kikuchi bands on a grayscale. Different microstructural features such as grain boundaries, strain, topology and phase can be visualised since they will affect how perfect the crystal lattice is. Structures that compromise the perfection of the lattice lead to a poorer pattern quality and will appear darker on the IQ map. As mentioned, ferrite and martensite are not possible to separate after indexing, but differences in pattern quality can make it possible to differentiate in an IQ map since martensite has a higher strain density than ferrite, and will appear darker [91].

### Inverse Pole Figure (IPF)

Inverse Pole Figure (IPF) maps are used to represent crystal orientation by assigning different colours depending on the crystallographic direction of a point compared to a predetermined reference axis. The meaning of the colours of the map can be determined from the IPF key. The IPF key, as shown in Figure 4.3, has three corners relating to the face {001}, edge {101} and corner {111} of the crystal, which is compared to the x, y or z reference axis of the material. Because of this, the IPF map will not show the complete crystal orientation, but only the plane that is normal to the chosen reference direction [92].

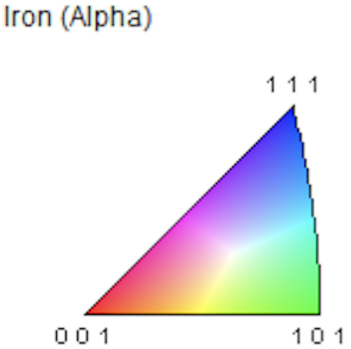

**Figure 4.3.** IPF key of Iron (alpha).

### Kernal Average Misorientation map (KAM)

A KAM map provides information about the amount of internal strains and dislocation densities in the analysed microstructure. A kernel is the set of neighbouring pixels around the scanned pixel. The analysis calculates the average degree of misorientation within the kernel assigned to the centre point. High KAM values are a result of orientation change which comes from dislocation or internal strains. For example, martensite has a higher internal strain than ferrite, and will therefore result in higher KAM values [93].

### 4.4.3 Energy-dispersive X-ray spectroscopy (EDS)

Energy-dispersive X-ray spectroscopy (EDS) is a commonly used analytical method in SEM that provides a chemical analysis of the specimen. Elements with low atomic numbers cannot be detected, which include elements from hydrogen to beryllium. In these experiments the EDAX OCTANE PRO-A EDS detector (sensor area 10 $mm^2$) was used. Several elements, such as carbon, chromium, sulphur, manganese, aluminium, silicon and others have been mapped at the same time. The operating settings are given in Table 4.2.

## 4.5 Electron Probe Micro Analyzer (EPMA)

Electron Probe Micro Analyzer (EPMA) was used for more detailed chemical analysis of the sample than EDS can deliver. EPMA can produce both quantitative and qualitative results. The machine works similarly to a SEM, with an electron beam bombarding the sample, but multiple Wavelength Dispersive X-ray Spectroscopy (WDS) detectors make it specialised in analysing chemical composition. The sampling volume can be as small as one cubic micron and all elements heavier than boron can be detected. The sensitivity of the WDS detectors is also 1-3 times increased compared to EDS.

In these investigations mapping of carbon and chromium content was in focus, but, also aluminium, oxygen sulphide, silicon, manganese and iron were mapped. The analysis was performed using EPMA JEOL - JXA 8500F - Microprobe at an acceleration voltage of $E = 15$ kV for the case-hardened steel and $E = 10$ kV for the through-hardened steel, with a spatial resolution of 0.100 $\mu$m. Before the EPMA analysis, the vibration polishing step was repeated to remove any carbon contamination that may have occurred in previous investigations.

## 4.6 Nanoindentation

In order to determine the mechanical properties of the steel, the well-established nanoindentation technique was employed using a Hysitron Ti 950 TriboIndenter®.

The indentation apparatus consists of a depth-sensing indenter and an optical microscope. When the load is applied to the indenter the depth of the indent is continuously monitored, and the resulting data is used to calculate mechanical properties [94]. The used indenter has a Scanning Probe Microscope (SPM) imaging option which was used to get information about the surface topography, where the images were processed in the open-source software, Gwyddion.

Calculation of Berkovich hardness ($H_{it}$) is preformed according to the Oliver-Pharr (OP) method from the following formula [95]:

$$H_{it} = \frac{P_{max}}{A(h_c)} \tag{4.1}$$

where $P_{max}$ is the peak load and $A(h_c)$ is the projected area of contact between the indenter and the test specimen at the contact depth, $h_c$ [96].

Conversion from Berkovich hardness, $H_{it}$, to Vickers hardness, HV can be achieved using the following equation [96]:

$$HV = 94.5 \cdot H_{IT} \tag{4.2}$$

Vickers (4-sided), Cube-Corner (3-sided), and Berkovich (3-sided) are examples of indenter tips that are commonly used for hardness tests [97]. For fracture toughness measurements, a tip with a larger indent volume, such as Cube-Corner is prefered, while Berkovich has a smaller indent volume which is better for hardness measurements [94].

In this thesis, the Berkovich tip was used for nanoindentation hardness measurements. For single indents, a maximum load of 3000 $\mu$N was applied. The time vs. load function for single indents is presented in Figure 4.4.

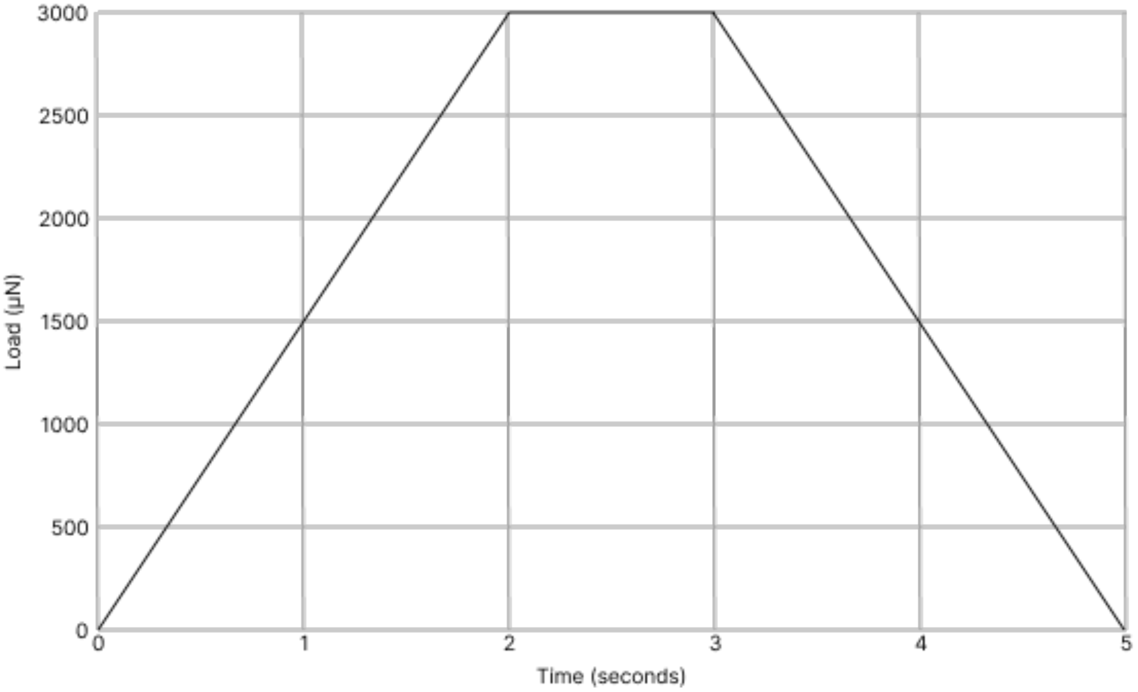

**Figure 4.4.** Load vs. time function used in hardness measurements.

# 5 Results

In this section, SE-SEM, EBSD, BSE, EDS, EPMA and Nanoindentation results are presented. The results are divided into two sections, case-hardened steel and through-hardened steel. The two sections are further divided by the characterisation method.

## 5.1 Case-hardened steel

For the master thesis, only EPMA results were performed for the case-hardened steel. Results from SEM, such as BSE and EBSD, and nanoindentation can be seen in Section 2.

### 5.1.1 Chemical composition

EPMA was used to characterise area A3 of the case-hardened steel. The focus was mainly on carbon content analysis, but also other elements assumed to be present in the sample were analysed, such as silicon, oxygen, manganese, chromium, iron, molybdenum and nickel. These results are attached in Figure A.1 in Section A the Appendix. The carbon analysis showed a homogeneous carbon distribution both inside and outside the WEM. The carbon concentration was low, and no differences between the matrix and the WEM were observed. No carbides were observed in the matrix. There was an elevated carbon, silicon, oxygen and iron concentration in the crack. No other tested elements showed anything but a homogeneous distribution without any differences between the matrix and the WEM.

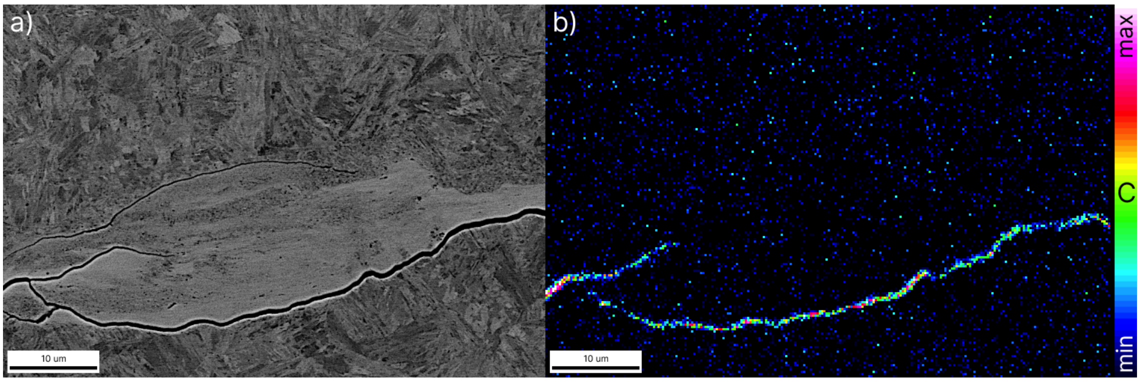

**Figure 5.1.** EPMA carbon analysis of WEM in area A3. a) BSE image with a white rectangle highlighting the EPMA analysed area in b).

## 5.2 Through-hardened steel

### 5.2.1 Material

Figure 5.2 shows a BSE image of an area of the analysed sample which came from an outer race. The image is taken close to the raceway surface in the circumferential plane, which can be observed in the bottom part of the image. As can be seen in the image the microstructure consists of martensite plates and randomly distributed spheroidised carbides. Many inclusions in varying sizes could be observed in the material, ranging from less than 1 $\mu$m to more than 5 $\mu$m in diameter.

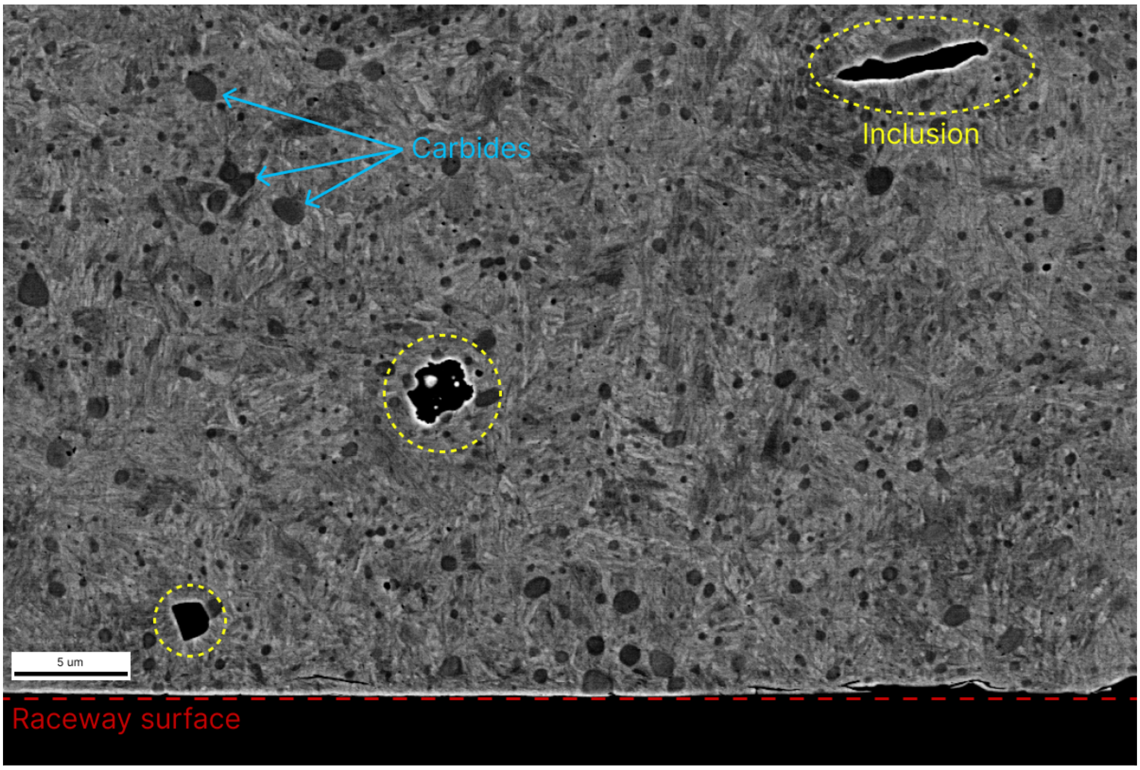

**Figure 5.2.** BSE image showing a typical section along the raceway surface with inclusions marked with yellow circles and examples of carbides marked with blue arrows.

### 5.2.2 Crack development

The analysed bearing section can be seen in Figure 5.3. The orange arrow marks the area in which every WEC analysed in this thesis was found. Outside this area and in other bearing sections there was no observed WECs.

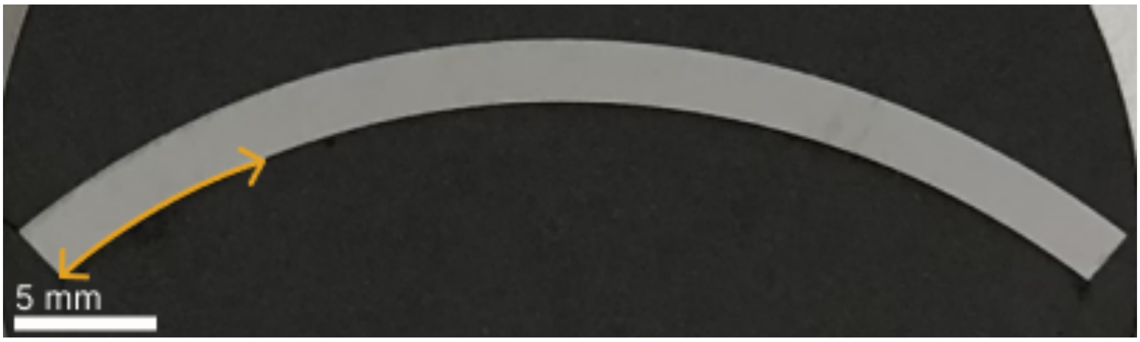

**Figure 5.3.** Analysed bearing section with orange line showing the area where WECs were observed.

While inside this area, most inclusions at a depth between 30-150 $\mu$m had some form of crack propagation, either only within the inclusion but mostly also some cracking in the bulk material. In Figure 5.4, twelve cracks in various stages of crack propagation are presented. WEM connected to the cracking is outlined with blue stipples, and the depth of each WEC is given in the bottom right corner of each figure. Each analysed WEC were given a name, which is visible in the top right corner of each figure.

The cracks were found to most commonly initiate from inclusion tips, and varied in shape, orientation and size. The longest crack found was B7 with a length of 15 $\mu$m, while the shorter cracks, such as B1 could be less than 1 $\mu$m. Every crack propagated with an angle equal to or less than 30°, illustrated in Figure 5.4 d) with WEC B4 which was the crack with the steepest crack propagation at 30°. The amount and shape of the WEM did also vary a lot. The cracks B7 and B8 had long narrow WEM following the long cracks, while cracks such as B4, B5 and B6 had wider WEM areas but shorter cracks. At some cracks, all the WEM was on one side of the crack, while in others the WEM was seen on both sides, but usually with a large portion on one side.

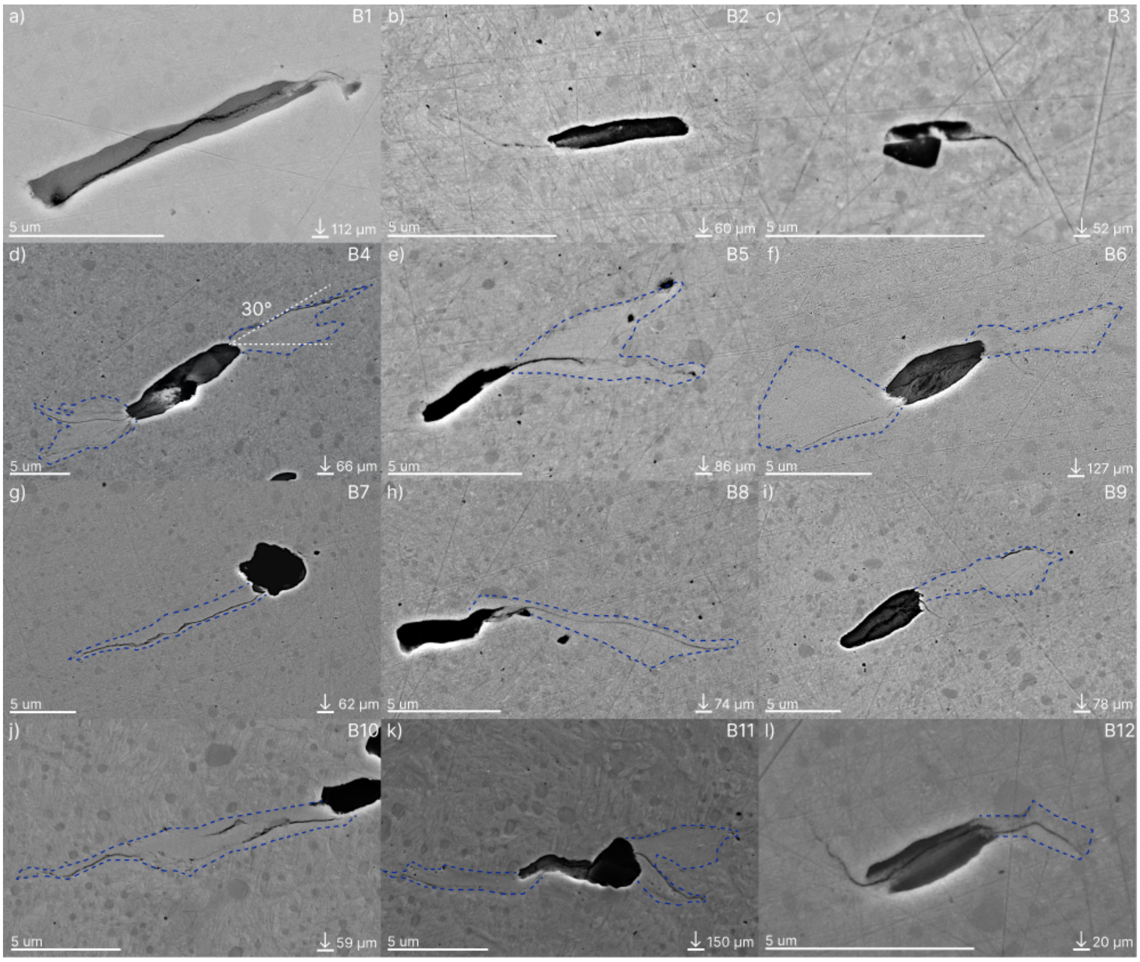

**Figure 5.4.** Inclusions with crack development. WEM is outlined with blue stippled lines, depth below the contact surface is given in the bottom right corner, and each area is given a name in the top right corner.

### 5.2.3 Crack initiation point

Results from the EDS analysis of five inclusions with WEC initiation are shown in Figure 5.5 - Figure 5.7, the result from all tested elements can be seen in the appendix. In Figure 5.5, EDS analysis of three WEC initiating inclusions is presented. The analysis showed that the three cracks were initiated from inclusions made from MnS.

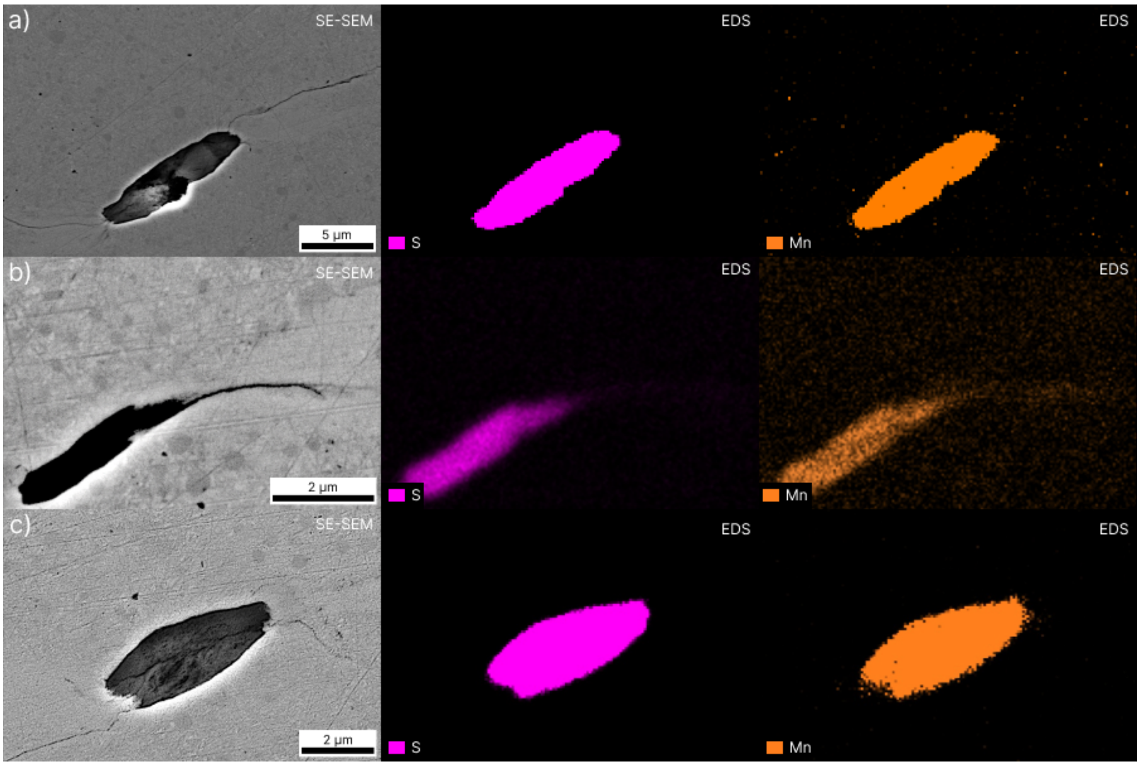

**Figure 5.5.** EDS result of three inclusions with WEC propagation, showing SE-SEM image and EDS analysis of sulphide and manganese for a) WEC B4, b) WEC B5 and c) WEC B6.

The result of the EDS analysis of inclusion B7 is shown in Figure 5.6. The inclusion was determined to be a dual-phase inclusion, consisting of sulphur, manganese, aluminium and oxygen. The inclusion featured an $Al_2O_3$ core, with MnS detected in the inclusion's outer region in some instances. Figure 5.6 d) reveals that the crack initiated from a portion of the inclusion where the $Al_2O_3$ was covered by MnS. In Figure 5.6 a), a minor crack between the MnS portion and the $Al_2O_3$ can be seen marked with a green arrow. Cracking was observed inside the MnS inclusion the crack initiated from. Black spots were also observed along with the interface between the MnS and the martensite matrix, this was also observed at the crack initiation site. A crack was also discovered inside the MnS along the right side of the inclusion, marked with red arrows.

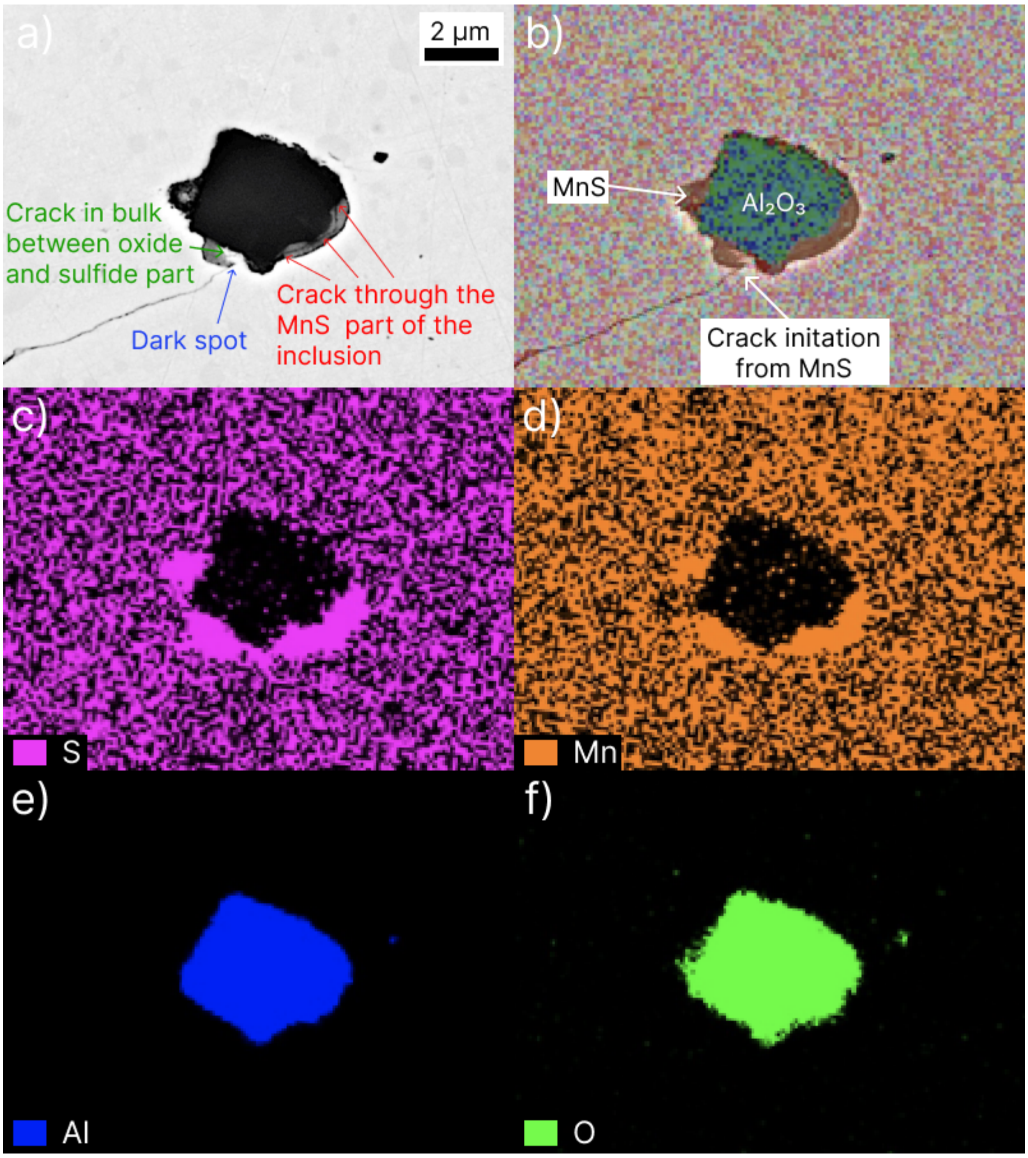

**Figure 5.6.** EDS result of inclusion connected to WEC B7. a) SE-SEM image, b) combination of all tested elements on top of SE-SEM image, c) sulphur analysis, d) manganese analysis, e) aluminium analysis and f) oxygen analysis.

Investigations of inclusion in area B8 revealed that it was a dual-phase inclusion consisting of sulphur, manganese and aluminium, presented in Figure 5.7. It appears that there was a minor increase in oxygen content in the same position as the Al component of the inclusion, based on the oxygen analysis in Figure 5.7 f). As depicted with red arrows in Figure 5.7 a), a crack from the aluminium oxide part of the inclusion, through the sulphide, to the region of crack initiation was observed.

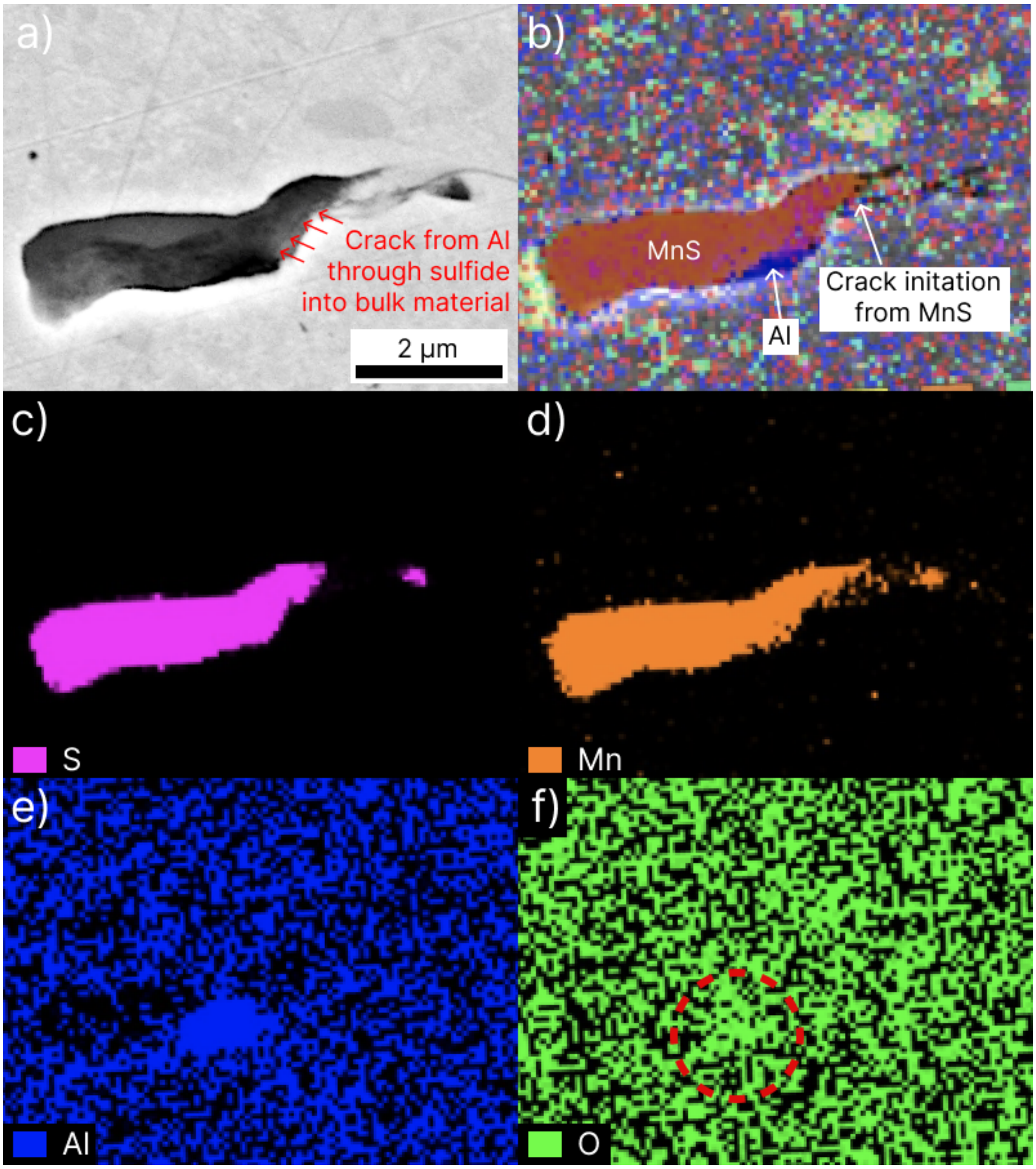

**Figure 5.7.** EDS result of inclusion connected to WEC B8. a) SE-SEM image, b) combination of all tested elements on top of SE-SEM image, c) sulphur analysis, d) manganese analysis, e) aluminium analysis and f) oxygen analysis.

### 5.2.4 Microstructure

BSE imaging was used to study several cracks and detect microstructural changes in the WECs. Two samples of typical microstructures are illustrated in Figure 5.8. Fine and nanocrystalline grain sizes were discovered inside the WEM. The fine and nanocrystalline grains appear to be grouped in bands parallel to the crack. Dark spots can be seen near the edges of the WEM. In Figure 5.8 b) a crack can be seen between the WEM and the matrix to the right in the middle of the WEM area. The crack is not connected to the main crack which propagates from the inclusion.

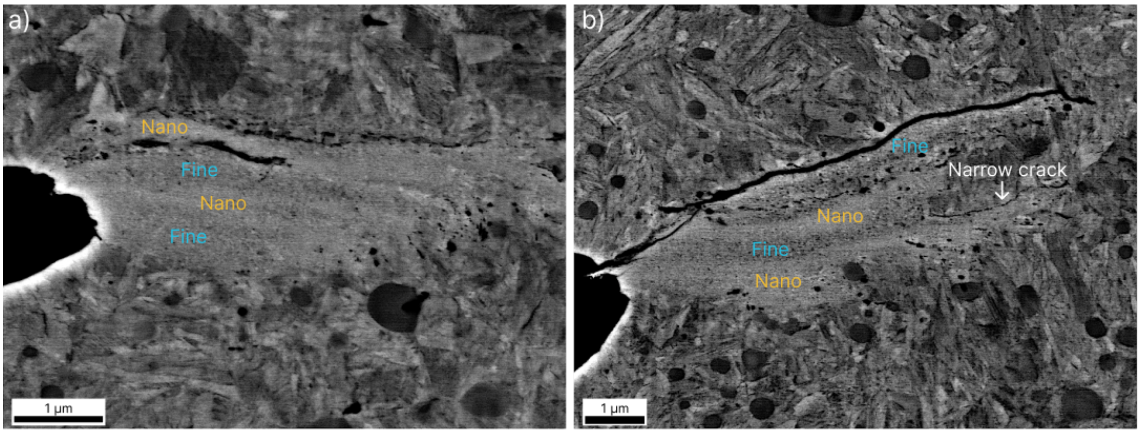

**Figure 5.8.** BSE images showing the microstructure of a) WEC B13 and b) WEC B4. Areas of different sized grains have been marked as fine or nanocrystalline.

Although no spheroidised carbides were identified in the WEM, multiple cases of dissolved carbides near WEC were discovered, as seen in Figure 5.9.

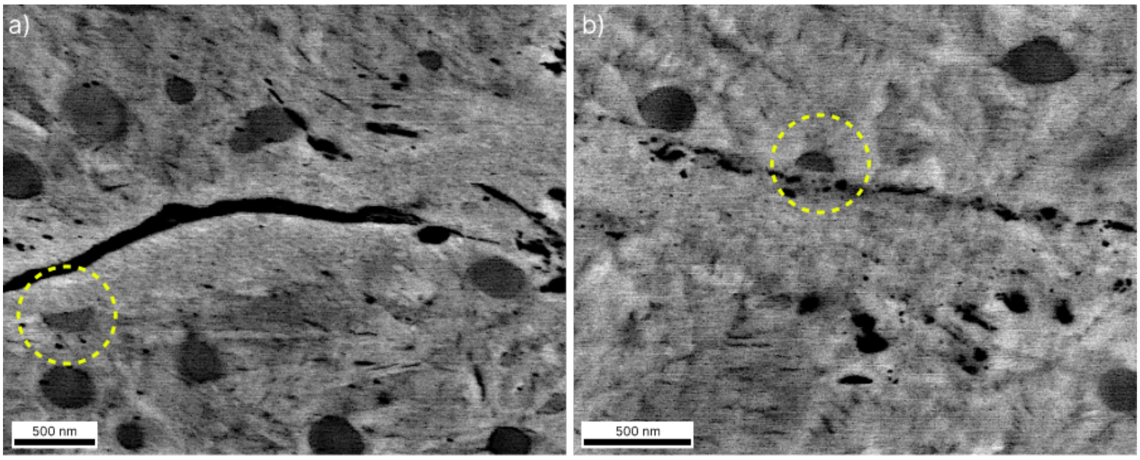

**Figure 5.9.** BSE images og a) WEC B10 and b) WEC B14 showing partly dissolved carbides marked with yellow circles.

Voids were observed in many places, both in the matrix as illustrated with blue circles in SE-SEM and BSE images in Figure 5.10 and in the transition between the WEM/matrix illustrated with yellow circles and inside the WEM.

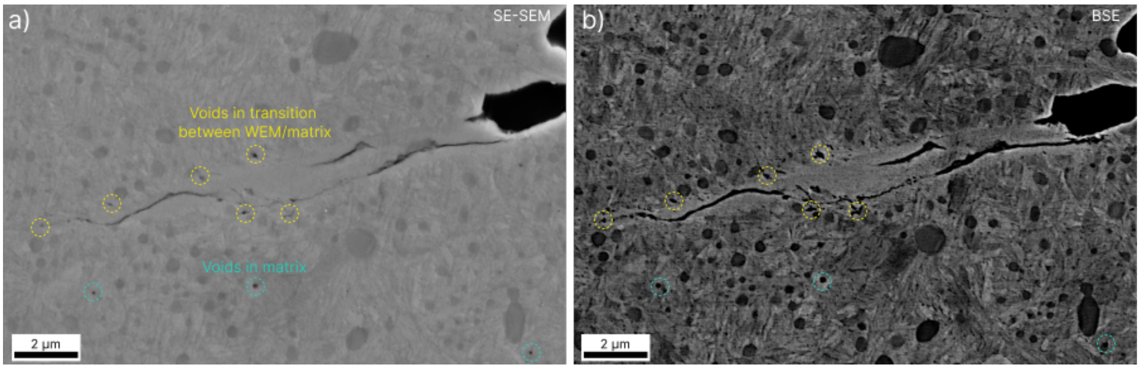

**Figure 5.10.** a) SE-SEM and b) BSE image of WEC B10 showing voids in the WEM and matrix.

As previously mentioned, BSE analysis found multiple dark spots inside WEM. One WEM in particular, shown in Figure 5.11, contained numerous dark spots. In the BSE analysis, a partly dissolved carbide could be observed close to the inclusion. A crack could be distinctly seen at the right part of the WEM, while a more narrow dark line resembling a crack could be seen at the left part of the WEM. Most of the dark spots are observed in the WEM closest to the inclusion and up on the left side of the WEM. Along the crack on the right side, there are also many black spots. The colour of the dark spots on the BSE image appears darker than the carbides and approximately the same colour as the inclusion and crack. The WEM was investigated further using SE-SEM and EDS. Some darker features inside the WEM can be seen in the SE-SEM image, which could either be due to varying atom number contrast of distinct phases or tiny voids or cavities. A larger black spot marked with blue in the SE-SEM image was tested with EDS. The spectrum from the analysis is shown in Figure 5.11 c). The analysis found that the area contained 61.61 at.% Fe, 12.65 at.% S, 10.88 at.% Cr and 14.86 at.% Mn.

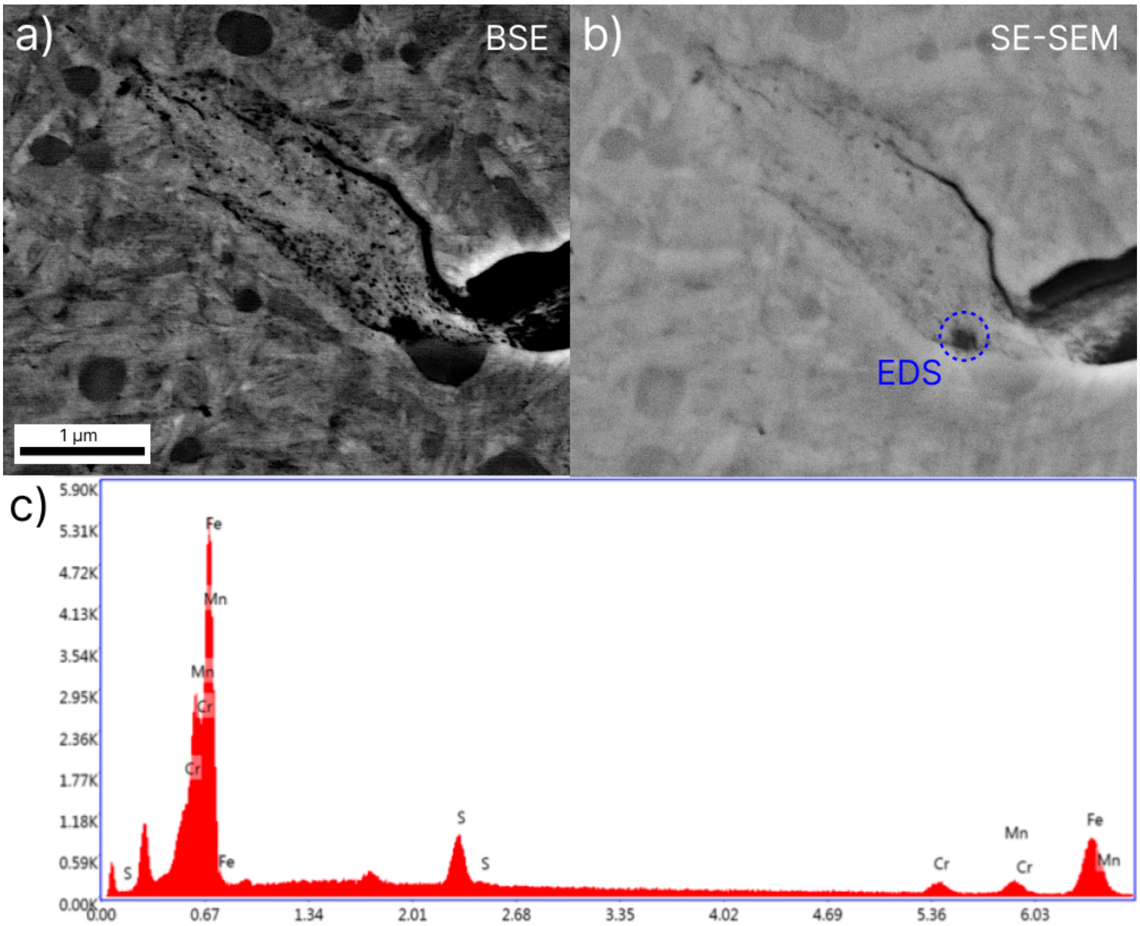

**Figure 5.11.** a) BSE image of WEC B12 b) corresponding SE-SEM image and c) spectrum from EDS point scan with position marked with blue ring in b).

Figure 5.12 shows EBSD maps of a WEC, including an IQ map, an IPF map, a map displaying the different phases, and a KAM image. The WEM region appears dark in the IQ map since the fine and nanocrystalline grains in the WEM are too fine to produce good EBSD patterns, also grain boundaries show low IQ values. IPF map in the [001] direction is shown in Figure 5.12 c). All points are indexed with CI>0.15 to remove most of the non-indexable points. In the map, it can be seen that the WEM areas are non-indexable. The phase map shows that the microstructure consists of 0.899 $\alpha$-iron, 0.099 cementite and 0.001 $\gamma$-iron, while the KAM map shows that the martensite has a low to moderate internal strain, the strain is highest at the grain boarders.

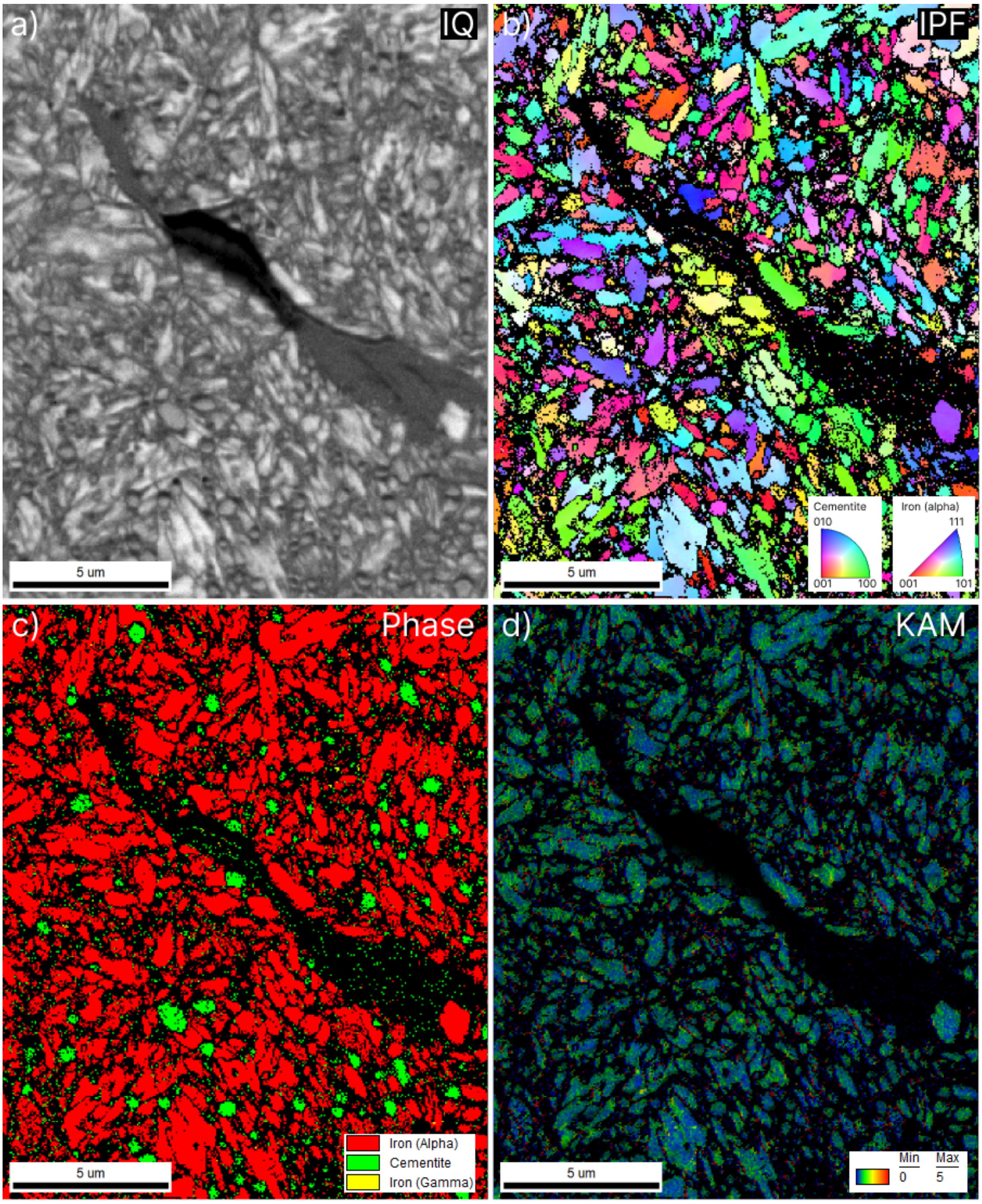

**Figure 5.12.** EBSD result from WEC B14. a) IQ map, b) IPF map, c) phase map and KAM map.

### 5.2.5 Chemical composition

Carbon and chromium dissolution and redistribution during the formation of WEM has been a highly debated topic, as discussed in the introduction. To investigate if there are any chemical variations between the WEM and the untransformed matrix material, EPMA analyses of three WECs were conducted. The EPMA results are organised from Figure 5.13 through Figure 5.15. The spherical high carbon and chromium areas on the EPMA maps match the positioning of dark spots assumed to represent carbides in the BSE images, confirming that the matrix consists of a chromium carbide rich microstructure. The microstructure in close proximity to the WEM seems to be unaffected by the microstructural change in the WEM. Inside the WEM, there was no such enhanced carbon concentration from carbides. From these results it is difficult to detect any carbon depletion or enrichment inside the WEM, however, the carbon and chromium content in the WEM appears to be similar to that of the martensitic structure in the matrix that is unaffected by carbides. A couple of chromium clusters was observed inside the WEM, shown in Figure 5.13 and Figure 5.14.

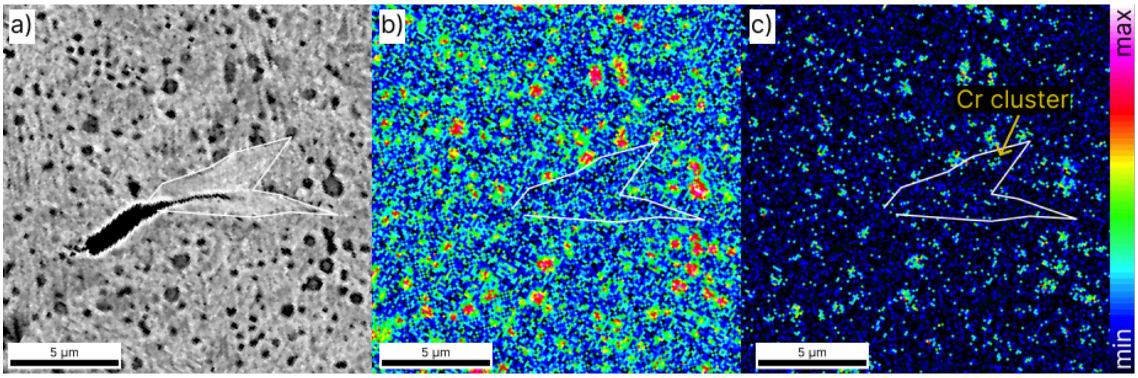

**Figure 5.13.** EPMA carbon analysis of WEC B5 where the WEM area is marked with white lines, showing a) BSE image of the area and b) the corresponding EPMA carbon and c) chromium analysis.

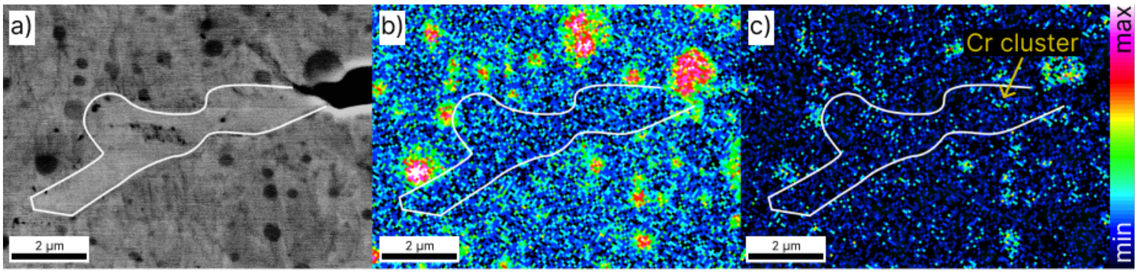

**Figure 5.14.** EPMA carbon analysis of WEC B15 where the WEM area is marked with white lines, showing a) BSE image of the area and b) the corresponding EPMA carbon and c) chromium analysis.

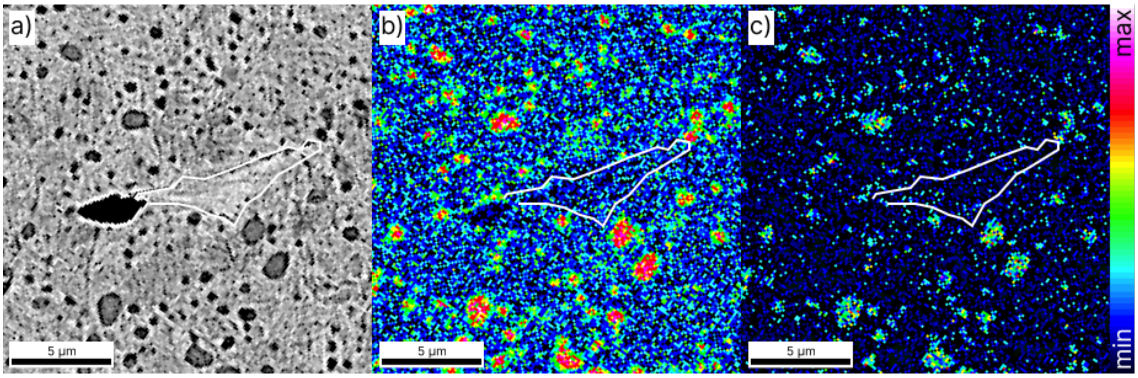

**Figure 5.15.** EPMA carbon analysis of WEC B16 where the WEM area is marked with white lines, showing a) BSE image of the area and b) the corresponding EPMA carbon and c) chromium analysis.

### 5.2.6 Mechanical properties

Single indent nanoindentation mapping was performed in two regions which had been investigated with BSE. All point data from these tests can be found in Table B.1 in the Appendix. The hardness of the matrix was tested by a 4x4 grid with 10 $\mu$m indent spacing, shown in Figure 5.16. The results showed that the unaltered matrix had an average hardness of 5.8 ± 0.4 GPa.

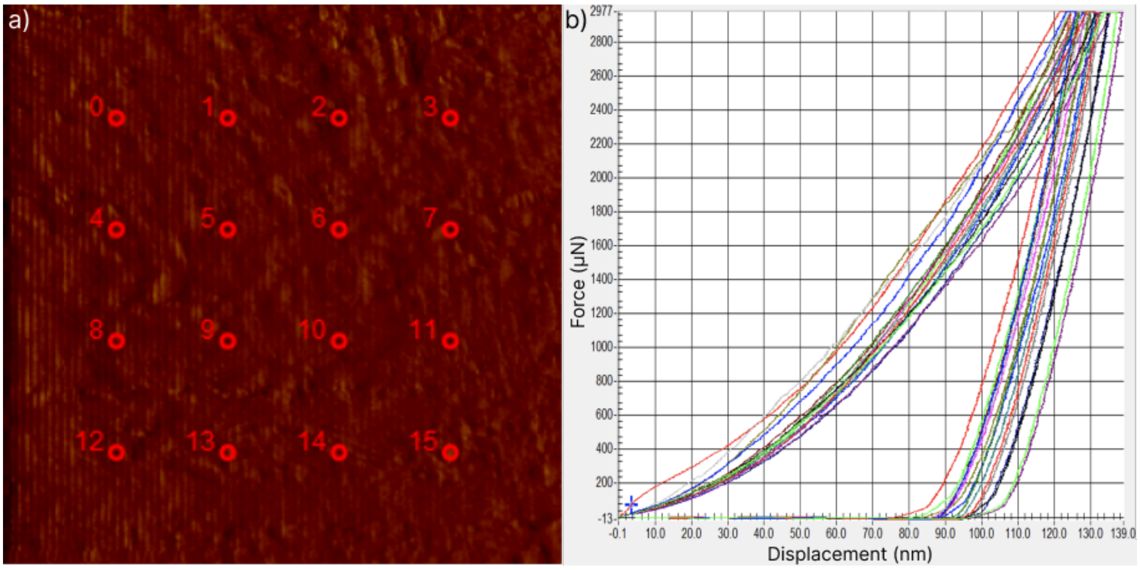

**Figure 5.16.** Indentation grid of martensite matrix. a) SPM image of indented area and b) load-displacement curves

Further, the hardness in two WECs was tested. In WEC B10, presented in Figure 5.17, ten indents were placed in the WEM (indent 1 to 10), and displayed an average hardness of 8.0 ± 0.5 GPa.

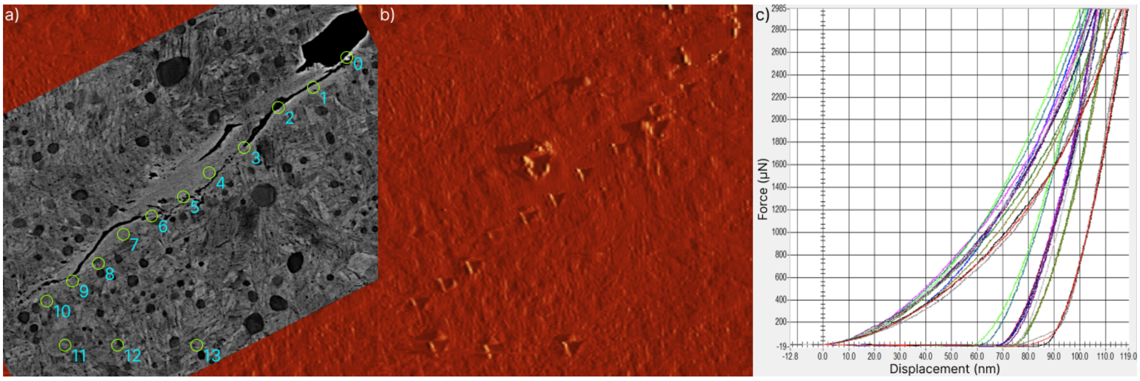

**Figure 5.17.** Indentation of WEC B10. a) BSE image showing indent placements, b) SPM image after indentation and c) representable load-displacement curves from nanoindentation in WEM and matrix.

In WEC B11, shown in Figure 5.18, three indents were placed in the WEM (indent 2-4). The average hardness of these indents is 7.40 ± 0.05 GPa.

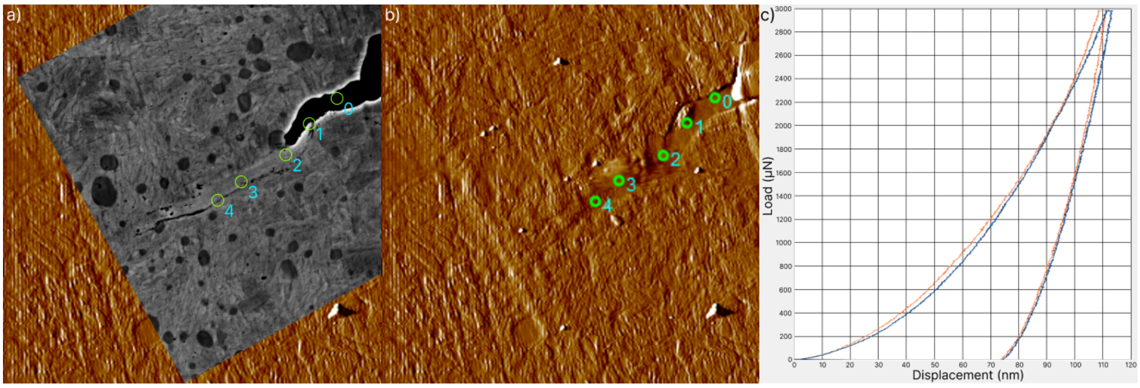

**Figure 5.18.** Indentation of WEC B11. a) BSE image showing indent placements, b) SPM image before indentation showing indent placements and c) representable load-displacement curves from nanoindentation in WEM.

Overall the hardness in the WEM was found to be 7.9 ± 0.5 GPa, thus showing that the WEM had a 36 % increase in hardness compared to the measured hardness of the unaltered matrix.

# 6 Discussion

First, the new results for the case-hardened steel will be discussed, then the through-hardened steel results before comparison between the two steel grades of relevant topics.

## 6.1 Case-hardened steel

### 6.1.1 Chemical composition

The EPMA carbon analysis map reveals a carbon concentration that is uniform, with no difference in concentration between the WEM and the matrix. In addition, no carbides were found in the parent material or the WEM. Analysis showed a high carbon content in the crack, however, since the EPMA study also revealed a high silicon and oxygen content in the crack, the high carbon content is presumed to represent residue from the polishing procedures.

The crack was discovered 2800 $\mu$m below the surface, and since no carbides were found in the area and the carbon concentration was uniform, it is evident that the matrix at this depth was not influenced by carburization during the case hardening process. As a result, a carbon content of 0.15-0.19 wt.% is anticipated in the matrix. When analysing these results one therefore should keep in mind that carbon is an element that is difficult to analyse due to its light nature. Due to the low overall carbon content in the analysed steel, there may be variations in the carbon content that the method can not detect.

In contrast to the homogeneous carbon distribution found in this study, others have reported both carbon enriched and depleted areas inside the WEM, however, a general carbon depletion is often seen in the WEM compared to the matrix [41, 42, 47]. Carbon has a low solubility ($>$0.005 wt%) in ferrite and is stabilised by lattice defects, grain boundaries, and dislocations [15]. Curd et al. [47] argue that the WEM expel carbon when transforming into ferrite, resulting in depleted areas in the WEM since newly formed ferrite grains have a low dislocation density. Further RCF introduces dislocations to the recrystallised grains, allowing them to accommodate more carbon, resulting in an enriched WEM. The carbon content of the parent material around the WEC analyses in this thesis, on the other hand, is much lower than the carbon content of the through-hardened steels ($\sim$1 wt.%) in the results of Curd et al. [47] and Mayweg et al. [41, 42]. As a result, in this particular WEM, depletion may not be required to stabilise the ferrite grains in the first place.

The variety in grain size has been linked to the carbon concentration [41], as mentioned in the introduction, but based on these EPMA data, it can be assumed that the carbon content was not the source of the varying grain sizes in the investigated WEM. The chemical examination revealed a uniform distribution of all the elements mapped with EPMA, including chromium, which has also been connected to the production of WEM, implying that the transformation is not related to the chemical composition of the material.

## 6.2 Through-hardened steel

### 6.2.1 Crack development

The test rig successfully created WECs in the outer ring of a 100Cr6 bearing with contact pressure at 1.9 GPa. The cracks were found at a depth between 30 - 150 $\mu$m underneath the surface, correlating with findings of other authors [24, 45] suggested to be due to that the maximum shear stress is found at these depths. All WECs were found in one restricted area in the outer race of the bearing (see Figure 5.3). This could indicate that something was affecting this area only which induced the cracks, this could include local electrical currents, surface damage or damage to tribofilm [57, 78, 80]. The bearing was under the influence of a low electrical current and 'bad lubricant' containing ZDDP that has been found to promote hydrogen diffusion into the steel. The outer ring was connected to the negative pole in the electric current, which should mean that the cracks should form in the outer ring [80], consistent with the findings in this study. A likely scenario could be that the electrical current has decomposed the lubricant in this specific region due to cathode reactions. Further, hydrogen has been absorbed into the steel and becomes confined at inclusions decreasing the crack initiation threshold. However, no further investigations into hydrogen levels, tribofilm or surface damage were done during the experimental work of this thesis.

The cracks found in the bearing section were all short $\leq 15$ $\mu$m, indicating that they were captured not long after the initiation stage. WEM and cracking were seen on both sides of several inclusions, where the WEM resembled butterfly wings. At first glance, it would be easy to mistake these cracks for butterflies. All cracks propagated with an angle less than or equal to 30°, as shown in Figure 5.4. Butterfly cracks must propagate at an angle of 30° to 50° per definition. WECs propagating at lower degrees than 30° have been mistakenly labelled as butterflies because of their winged appearance, however, there are suggested two different initiation mechanisms that create the different types of fractures, as Bruce et al. [45] points out. As a result, the cracks identified in this thesis will be referred to as WECs rather than butterflies.

The WEM seemed to be heterogeneously disturbed around the cracks. In some WECs, all WEM was on one side of the microcrack, while in others WEM was found on both sides, often in unequal amounts. The fact that WEM is only found on one side of the crack has been mentioned to be evidence that the microstructural transformation by crack faces rubbing is not likely [47, 98], but that WEM is rather created in front of the crack tip due to severe plasticity/stress concentration [47]. Morsdorf et al. [12] have developed a theory where they explain how it is possible to have WEM at only one crack face due to the crack moving nominally through the material.

### 6.2.2 Crack initiation point

All cracks were found interacting with inclusions, making it evident that inclusions were the initiation point for the investigated cracks, which previously has been confirmed by Evans et al. [10] to be a WEC initiator. Spille et al. [61] found that the use of 'bad lubricant' could lead to the formation of voids and pores accompanied by microstructural change, which could be WEC initiators. Voids were observed in the matrix in this study, but no microstructural change around them was observed.

All WEC initiating inclusions were categorised as small inclusions, less than 20 $\mu$m in width. The WECs appear to prefer to start at the inclusion tips, where the inclusion has the smallest radius of curvature i.e. the location of maximum stress around the inclusion [99]. Five WEC initiating inclusions were analysed with EDS. The result showed three inclusions made of MnS and two dual-phase inclusions made of MnS-$Al_2O_3$. Cracking that propagated into the steel matrix could be observed in the three MnS inclusions (Figure 5.5). Internal cracking in sulphides has been attributed to the lower plastic limit of the manganese sulphide compared to the martensitic steel matrix [45]. The crack formation continues into the steel matrix and the inclusion is the initiator of crack propagation.

The dual-phase inclusions (Figure 5.6 and Figure 5.7) both displayed examples of crack inside the MnS part of the inclusion. In Figure 5.6 the crack marked with red inside the MnS does not propagate into the matrix, but each end of the crack stops when it meets the oxide. In Figure 5.7 the crack ends in the aluminium part on one side and is the cause of crack propagation on the other side. Possible reasons for the initiation of these cracks could both be that cracks were created in the MnS due to the low plastic limit of sulphide or the hardness mismatch between the oxide and sulphide phases in the inclusion.

The crack propagation into the matrix for the dual-phase inclusion in Figure 5.6 happens from the MnS part. A crack could be observed from the MnS part through the matrix to the $Al_2O_3$ part, but where this crack was initiated is unknown. Both internal cracking and a black mark could be observed at the WEC initiation site. The black mark could be a void from detachment between the soft sulphide and the harder martensite, which could happen during quenching or rolling due to the weak bond between the sulphide and martensite or be a separation between bulk and inclusion due to internal cracking [45].

It should be noted that the cracks initiated at dual-phase inclusions are the two cracks that have propagated the longest. This may suggest that the crack initiation has occurred earlier for these two cracks than for the cracks only containing MnS, favouring the theory that the hardness mismatch has led to an earlier crack propagation for the two cracks [60].

### 6.2.3 Microstructure

In the present work, the WEM microstructure was demonstrated to contain an altered microstructure consisting of fine and nanocrystalline grains (see Figure 5.8) that can not be indexed by the EBSD system (see Figure 5.12). This show how difficult it is to produce good quality EBSD maps of WEM because of the small grain size and the restrictions on the scanning volume. The fine grains appear grey and the nanocrystalline grains appear white-grey on BSE images. In the bulk material, EBSD confirmed that the plate-like structure consisted of an $\alpha$-ferritic structure, i.e. martensite, with spherical carbides. EBSD also showed that the matrix contained no significant amount of retained austenite. The KAM map showed a homogeneous distribution of KAM values, low inside grains and moderate at the grain boundaries, which indicates that there are not any localised strain points in the matrix microstructure. Inside the investigated WEMs no carbides were observed but partly dissolved carbides were found bordering the WEM (see Figure 5.9). Carbide dissolution has been considered to be caused by severe plastic deformation, increased dislocation interaction or grain refinement [1, 10, 24, 51, 85].

Other studies have reported coarse grains in the WEM closest to the untransformed material, furthest away from the crack. This was not observed in this study, but grain size varies from fine to nanocrystalline was found, and in some cases organised in horizontal bands parallel to the crack (see Figure 5.8). Grabolov et al. [24] also saw this difference in grain size inside the WEM of a butterfly crack, but in that case, the grain size increased as a function of the distance from the crack. They concluded that the grain size and non-uniform distribution of the ferrite grains were a direct result of the recrystallization process (RX) within the WEA, where the factor deciding the grain size is the dislocation density induced during plastic deformation. The grain size has also been linked to the carbon concentration, where the grain size is found to decrease with increasing carbon content [41], which will be discussed further in the next section.

Morsdorf et al. [12] have suggested that the crack moves nominally through the material. They propose that the WEM is created as a result of a dynamic recrystallization (DRX) process due to severe plastic deformation. Morsdorf et al. did not look at the variation of grain size to validate their hypothesis, however, based on their hypothesis it is suggested that the variation in grain refinement could be evidence of normal crack movement. Figure 6.1 shows how the hypothesis of Morsdorf et al. [12] could be related to the crack found in this study. Based on this theory the crack is proposed to have propagated as explained in the next steps and illustrated in Figure 6.1 b).

1. The crack initiated from the inclusion at the crack position marked with 'Initial WEC pos.' at the bottom of the WEM area.
2. The crack has gradually extended and the crack faces have been rubbed together creating WEM and allowing the crack to be closed and opened again in a slightly different position moving normally through the material.
3. Residues from what is suggested to be an earlier crack position can be seen marked with an arrow in the right part of the WEM. After this point, the crack has been divided and only a part of the crack has continued propagation and normal movement. The crack then gradually extends again while moving normal to the current crack location.

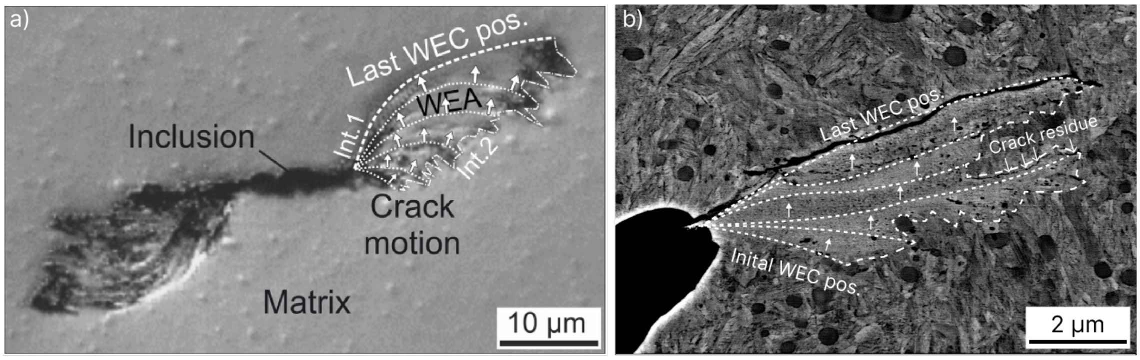

**Figure 6.1.** a) Illustration from Morsdorf et al. [12] showing the proposed crack movement during formation of a butterfly crack, b) illustration showing how the same formation mechanism could be applied to a WEC found during this study.

It is suggested that the grain size is homogenised inside each band because they are subjected to the same degree of plastic deformation along the whole crack. When the crack‘s normal movement has changed the position of the crack, the plastic deformation at the new location could recrystallise the grains into finer or coarser grains based on increased or decreased plastic deformation. Voids found at the interface between WEM and parent material, both in this WEC and as illustrated in Figure 5.10, have been reported to be due to the hardness difference between

WEM and matrix [55], while in this case they are suggested to be residues from the crack tip at earlier crack placements. Due to the short crack lengths of the WECs in this thesis, it has been concluded that they are in the initiation stage. It is proposed that if the crack had been allowed to propagate further before it was analysed, the crack would have had an angle larger than 30° from the inclusion compared to the rolling direction since further rubbing would have continued to move the crack normal through the material. This would have to lead it to be categorised as a butterfly rather than a WEC due to its appearance and propagation angle. It is therefore proposed that both WEC and butterflies can arise from the same mechanism.

One of the findings in this study was a WEM within particular many dark spots visible in the BSE image (see Figure 5.11). The WEM was further analysed with SE-SEM and EDS. The dark spots were in many places organised as lines in a direction from the inclusion to the end of the WEM, at some places parallel to the crack. It is hard to identify from the SE-SEM analysis due to the small features requiring high magnification, but the dark spots are assumed to be due to atom number contrast rather than voids in most cases. Morsdorf et al. [12] have reported dark features parallel to the crack inside the WEM, which has been identified as voids and cavities or redistribution of chromium. Based on these and other findings, they suggested moving crack theory as a new formation mechanism. In the current study, chemical analysis of the largest dark spot identified four elements: iron, chromium, manganese and sulphide. The iron likely originates from the overall microstructure and the chromium from the dissolved chromium carbide. The nearest source of manganese and sulphide is the MnS inclusion where the crack has initiated. Based on the likeness in colour of the dark spots that can be observed from the BSE image it is assumed that all the dark spots consist of MnS. A possible explanation for distribution of MnS throughout the WEM can be based on the 'moving crack theory' of Morsdorf et al. [12], where small parts of the inclusion has been transported into the WEM as a result of crack faces rubbing and normal crack movement. Another explanation could be that the MnS has been redistributed due to polishing during sample preparation, but this is not likely due to the lack of dark spots outside the altered microstructure.

### 6.2.4 Chemical composition

The EPMA results of three WECs confirmed that the microstructure of the matrix consists of a carbide rich martensite, as seen in EBSD and BSE results. The maps confirm the dissolution of carbides in the WEM, which has been attributed to the high local density during WEM formation. The carbon migrates to lattice defects, such as grain boundaries, vacancies and dislocations, since the new ferritic microstructure can not dissolve more than 0.005 wt.% carbon [15]. APT investigations have revealed that the carbon segregates at the grain boundaries, and is suggested to stabilise the nano-sized grains [41, 42, 50].

The WEM was found to be depleted relative to the matrix overall, but not compared to the martensitic matrix structure without carbides. Depletion within the WEM is in agreement with others [42, 47, 55], but as pointed out by Mayweg et al. [42] is this surprising if WEM is created by crack faces rubbing because the carbon concentration in the WEM should be the same as the nominal alloy composition. They suggest that the missing carbon can be found in nano-scale carbon deposits found heterogeneously distributed throughout the WEM. APT analysis showed that the deposits contained above 85 at.% carbon. They also point out that such deposits are small and soft and can be removed due to sample preparation leaving behind a void. They are also smaller than the spatial resolution of EPMA, and will therefore not be visible on EPMA heat maps.

As mentioned in the discussion in Section 6.1.1, Curd et al. [47, 55] found both carbon depletion and enrichment in WEM which was attributed to a varying degree of total damage accumulated in the WEM. This was not observed in the analysed WEMs in this thesis. In butterflies, they found only depleted areas, which they suggest is due to that butterflies often are found in the initiation stage of WEC networks. In the initiation stage, the damage is suggested to be more consistent and consequently, depletion may be seen, which can be applied to the WECs in this study since they were all in the initiation stage. But one should also consider that it is difficult to capture small differences in carbon content with EPMA when the carbon content is as low as approx. 1 %, as it is in the WEM and martensitic matrix since carbon is a light element. The sample was also coated with a carbon layer to increase conductivity, which may have been applied unevenly and could affect the ability to see small changes in carbon content.

Carbon diffusion into the matrix has been suggested as a possible reason for the carbon depletion in the WEM. In the results from this study, there seems to be no difference in the carbide density in the regions close to the crack from the regions further from the crack, as reported by Curd et al. [47]. Further, they suggest that the carbon may have diffused more broadly throughout the parent material [55], but this was not supported by any evidence.

Chromium content has also been investigated in relation to WEM formation.

Morsdorf et al. [12] suggested that the chromium content was redistributed within the WEM due to carbide dissolution during crack faces rubbing. Features of chromium resembling dissolved carbides have also been reported in other studies [47, 100]. Such redistribution was not found in investigated WEMs in this study. Some instances of clusters with elevated Cr were observed, but not clearly enough to conclude that these may have been residues of earlier carbides since the distribution was similar to that of the carbide free matrix. Other studies have also reported that the chromium content is homogenised [55, 98] and have suggested that this is because the chromium has been subjected to sufficient deformation to diffuse into the BCC lattice.

### 6.2.5 Mechanical properties

From the single point analysis it is evident that the WEM is 36 % harder than the parent material which agrees with previous studies which reports of increased hardness of generally 10-50% in the WEM [24, 31, 33, 47, 52, 55, 98]. The increase in hardness has been seen as a consequence of grain refinement due to the Hall-Petch relationship, dispersion of fine cementite particles and high dislocation densities [47, 55, 98]. It is suggested that the hardness of the WEM may promote cracking and micro-voids at the WEM/matrix boundary. Recent studies by Curd et al. [47, 55] have looked at the correlation between carbon depletion and enrichment and hardness where no clear correlation between the two was found. Their suggestion is that grain size, increased dislocation density and the presence of voids are the main reasons for increased hardness in the WEM. However, they do also suggest that if carbon is not in solid solution the carbon analysis would still show a high carbon content, but the carbon would lose its strength increasing the effect. Unfortunately, this thesis was not able to study the direct correlation of carbon content and hardness because of the preparation issues leading to the loss of the EPMA analysed areas, and would be suggested as further work together with APT or TEM analysis to investigate whether the carbon is in solid solution or not. Even though there is a depletion of carbon in the analysed WEM, the ferrite grains are supersaturated with carbon, and the carbon content is high to be a ferritic microstructure. It is therefore assumed that the main causes for hardness increase in the investigated WEM areas are the microstructural changes, such as grain refinement and dislocation density, but also possibly the supersaturation of ferrite grains and dispersion of fine cementite particles.

## 6.3 Comparison between case and through-hardened steel

### 6.3.1 Initiation and propagation

The difference in the lifetime of case-hardened (CH) steel and through-hardened (TH) steel has been investigated by Gould et al. [49]. They found that CH steel had a 2.3 times longer lifetime than TH steel during the same operating conditions. This is believed to be due to the induced compressive residual stresses in the carburized area in the CH steel which prevented the crack propagation.

The crack in the CH steel was found to propagate horizontally, which falls in line with what others have observed in CH steels [44, 49]. The cracks in the TH steel were in the initiation stage, and whether they would evolve to propagate in a horizontal or vertical manner could not be decided, but TH steels generally exhibit more axial cracking [44].

Results from the project and master thesis both showed that the crack initiation point likely was subsurface inclusions, however, there was a big difference in crack length, depth and number of initiated cracks. These features can not be compared since the two analysed steels did not undergo the same testing conditions since two different testing machines, sample shapes and drivers to promote WEC formation were utilised. This comparison will therefore focus more on the microstructural, chemical and mechanical properties of the WEM.

### 6.3.2 Microstructure

A side by side comparison of WEM microstructures in the two materials is presented in Figure 6.2. Both crack neighbouring matrix microstructures consisted mainly of a martensitic plate like structure with no retained austenite, which could be seen from EBSD results. Martensitic grains seem to be smaller in the TH steel than in the CH steel. The crack in the CH steel had initiated below the carburized area, carbides were therefore not observed with EBSD or BSE in the matrix microstructure in the CH steel, opposite to the TH where carbides were frequently observed. Similar structural features such as fine and nanocrystalline grains, voids and cracks not connected to the main crack were found in both WEM.

Based on the distribution of different grain sizes in bands parallel to the crack in the CH steel it was suggested that this was a result of the moving crack theory proposed by Morsdorf et al. [12]. This suspicion was further reinforced by the findings of similar and even clearer bands containing the same grain size in the TH steel, and the mass transport of inclusion into the WEM of a WEC in the TH steel. Crack residues and voids found in the WEMs also support this theory.

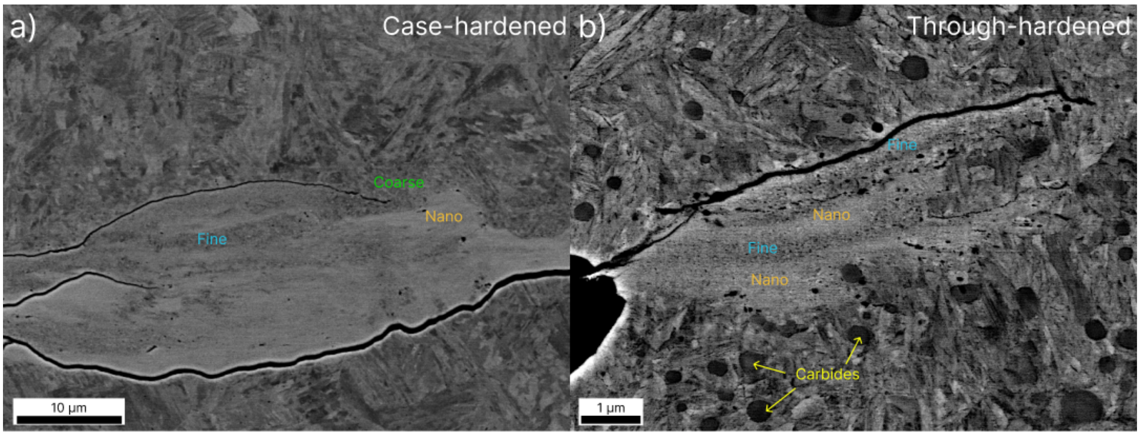

**Figure 6.2.** Microstructure of WEC in a) case-hardened steel and b) through-hardened steel.

### 6.3.3 Chemical composition

In the CH steel, the carbon concentration was homogenised inside and outside the WEM, and it was suspected to be about 0.19 wt.% since the area was not affected by the carburizing. The TH steel did also show a somewhat homogenised carbon concentration in the WEM which contained the same amount of carbon as the martensitic matrix but was depleted compared to the overall matrix. Carbon is a light element and is hard to measure quantitatively with EPMA. This may result in slight changes in the carbon content not captured by the analysis, especially when the carbon content is low as it is in the WEM. For both WEM it was discussed that the homogeneous distribution of carbon inside the WEM was a result of equal total damage accumulated and therefore equal amounts of dislocation sites stabilising the excess carbon, which do not promote the need for carbon diffusion from one area to another [47, 55]. Carbon dissolution was only seen in the TH steel since the CH steel was surrounded by a carbide free matrix. The dissolved carbon could not be located with EPMA but was suggested to either be in the form of carbon deposits in the WEM or have diffused broadly throughout the matrix.

### 6.3.4 Mechanical properties

The hardness of the matrix for the CH and TH steel were found to be respectively 5.2 ± 0.7 GPa and 5.8 ± 0.39 GPa, making the TH steel the hardest of the two. This is not a large hardness difference, and one should consider that the values are within each other's area of uncertainty, however, the factors that may have contributed to the slight hardness difference are the smaller martensitic grains in the TH steel and the higher carbon concentration which both will increase hardness.

The WEMs of the CH and TH steel were respectively found to have a hardness of 10.2 ± 2.0 GPa and 7.9 ± 0.5. This means that the CH WEM is 96 % harder than the matrix compared to just a 36 % increase in the TH steel. One explanation of why the CH WEM has a higher hardness than the TH WEM is that the average grain size in the CH WEM is smaller than in the TH WEM, but no BSE imaging suggested that this is true. Another suggestion is that the dislocation densities are higher in the CH WEM. The CH steel was further in the propagation process and may have accumulated more dislocation densities than the TH WEM which was in the initiation stage. CH steels have also been found to have broader WEM [49] which has been suggested to be due to slow propagation speed allowing the WEC to rub more which results in higher dislocation densities. The slow propagation was in temporary attributed to the induced compressive residual stresses in the carburized layer which would not affect this crack since it propagates deeper than the carburized layer. A third suggestion is that the higher carbon content of the TH steel results in more carbon, not in-solution but as carbon deposits reducing the hardness of the WEM [42].

# 7 Conclusion

This section provides the conclusion from this study related to case-hardened steel, followed by the through-hardened steel and finally the comparison between the two steels.

## 7.1 Case-hardened steel

EPMA analysis was performed at an area of the WEC in the case-hardened steel. The key findings are outlined below.

- The carbon concentration was found to be homogenised in the matrix and the WEM. Hence, the carbon concentration is not suggested to be the source of grain size variations or differences in mechanical properties.

## 7.2 Through-hardened steel

The microstructural alteration around several WEC in the initiation phase from a through-hardened steel bearing which had been tested under the electrical influence and with the use of 'bad lubricant' has been thoroughly studied. The main findings are summarised below.

- Multiple WECs were created in a localised area in the outer race of a bearing around the depth of maximum shear stress, between 30 - 150 $\mu$m beneath the surface, with electrical current and hydrogen diffusion as suggested drivers.
- Small inclusions were found to have caused crack initiation both due to the sulphide phase cracking and detachment between inclusion and matrix.
- WEM was found to be free of carbides, containing fine and nano-crystalline ferrite grains.
- Bands with similar grain sizes parallel to the crack are suggested to be an effect of the moving crack hypothesis.
- Distribution of MnS from inclusion through a WEM is suggested as evidence for crack faces rubbing.

- WEM was shown through EPMA carbon mapping to be carbon depleted compared with the overall matrix structure. The missing carbon was discussed to either be found in nano-scale deposits not visible with EPMA or have diffused broadly into the parent material.
- EPMA investigations showed that the chromium from carbides likely had been dissolved into the microstructure due to sufficient deformation since there were only a few features resembling dissolved carbides.
- The hardness in the WEM is increased by 36% with respect to the parent material. The increase is suggested to be due to grain refinement, increased dislocation densities and high carbon content.

## 7.3 Comparison between case-hardened and through-hardened steel

For the comparison between the case-hardened steel and the trough hardened steel, results from the project thesis and the EPMA result from this thesis were compared with the through-hardened steel analysed in this thesis. The comparison concluded with the following:

- WEM from both steels had similar microstructural features such as nanocrystalline and fine grains, the case-hardened steel also had coarse grains in the transition between WEM and martensite.
- Both WEMs had microstructural features which were suggested to support the moving crack theory of Morsdorf et al. [12].
- Both had a WEM with similar carbon content as the parent material. The through-hardened steel showed examples of carbide dissolution, while the crack in the case-hardened steel was located in a carbide free matrix.
- The WEM in the case-hardened steel had a higher increase in hardness compared to the matrix than the through-hardened steel. This is suggested to be due to increased dislocation densities in the case-hardened steel or more carbon in solution in the through-hardened steel.

# 8 Further work

Based on the analysis carried out in this thesis, the following work is suggested to increase the understanding of WEC:

- Investigate the effect of the electric current and 'bad lubricant' as drivers there should be conducted investigations into how the interaction between the two drivers affects the microstructure, and confirm whether hydrogen has diffused into the material by hydrogen measurements.
- Investigate the same WEM with EPMA mapping, BSE, EBSD and nanoindentation hardness mapping in the given order without any polishing in between analysing methods to get a better understanding of how chemistry, microstructure and mechanical properties affect each other.
- Test carried out during the current study has only given a 2D view of the WEC and WEM. Xe+ Plasma Focused Ion Beam - Scanning Electron microscope (PFIB-SEM) could be utilised to get a 3D map of the microcrack and the WEM to see whether any microstructural features inside the WEM affect the observed microstructure.
- Atom Probe Tomography (APT) and Transmission Electron Microscopy (TEM) of the WEM to look at the grains and carbon distribution with high resolution to further increase understanding of the microstructural change and carbide dissolution.
- Investigate how different steel microstructures and heat treatments (eg. through-hardened vs. case-hardened and case-hardened with a high amount of retained austenite) affect the initiation and propagation speed of WEC by studying the microstructural evolution of WECs at different propagation stages.

APT, TEM and PFIB-SEM are destructive techniques, gathering adequate information about the area before employing these techniques is therefore important to be able to analyse the results in the best possible way.

# Bibliography

[1] D. Scott, B. Loy and G. H. Mills. ‘Paper 10: Metallurgical Aspects of Rolling Contact Fatigue’. en. In: *Proceedings of the Institution of Mechanical Engineers, Conference Proceedings* 181.15 (June 1966), pp. 94–103. ISSN: 0367-8849, 2058-3362. DOI: 10.1243/PIME_CONF_1966_181_303_02. URL: http://journals.sagepub.com/doi/10.1243/PIME_CONF_1966_181_303_02 (visited on 20/10/2021).

[2] M-H Evans. ‘White structure flaking (WSF) in wind turbine gearbox bearings: effects of ‘butterflies’ and white etching cracks (WECs)’. en. In: *Materials Science and Technology* 28.1 (Jan. 2012), pp. 3–22. ISSN: 0267-0836, 1743-2847. DOI: 10.1179/026708311X13135950699254.

[3] M-H Evans. ‘White Structure Flaking Failure In Bearings Under Rolling Contact Fatigue’. PhD. Faculty of engineering and the enviroment: University of Southampton, July 2013. URL: https://eprints.soton.ac.uk/355966/.

[4] Kenred Stadler, Reinder H Vegter and David Vaes. *WHITE ETCHING CRACKS*. Jan. 2018. URL: https://evolution.skf.com/en/white-etching-cracks-a-consequence-not-a-root-cause-of-bearing-failure/.

[5] IEA. *Net Zero by 2050 - A Roadmap for the Global Energy Sector*. Tech. rep. International Energy Agency, May 2021.

[6] Lizet Ramírez, Daniel Fraile and Guy Brindley. *Offshore Wind in Europe - Key trends and statistics 2020*. Tech. rep. Aug. 2021. URL: https://proceedings.windeurope.org/biplatform/rails/active_storage/disk/eyJfcmFpbHMiOnsibWVzc2FnZSI6IkJBaDdDRG9JYTJWNVNTSWhkV1J2ZFhoa1lXdDBOVEo1ZDI1MU1ETTBOMlpyTldSNWVtZHdkd1k2QmtWVU9oQmthWE53YjNOcGRHbHZia2tpQVpKcGJteHBibVU3SUdacGJHVnVZVzFsUFNKWGFXNWtSWFZ5YjNCbExWOW1abk5vYjNKbExYZHBibVF0YVc0dFJYVnliM0JsTFhOMFlYUnBjM1JwWTNNdE1qQXlNQzV3WkdZaU95Qm1hV3hsYm1GdFpTbzlWVlJHTFRnbkoxZHBibVJGZFhKdmNHVXRUMlptYzJodmNtVXRkMmx1WkMxcGJpMUZkWEp2Y0dVdGMzUmhkR2x6ZEdsamN5MHlNREl3TG5Ca1pnWTdCbFE2RVdOdmJuUmxiblJmZEhsd1pVa2lGR0Z3Y0d4cFkyRjBhVzl1TDNCa1pnWTdCbFE9IiwiZXhwIjoiMjAyMi0wNi0wNlQxNzoxNDo0Ny4yMjJaIiwicHVyIjoiYmxvYl9rZXkifX0=--d0958287bbfd234073238548f7a19a451676d007/WindEurope-Offshore-wind-in-Europe-statistics-2020.pdf?content_type=application%2Fpdf&disposition=inline%3B+filename%3D%22WindEurope-Offshore-wind-in-Europe-statistics-2020.pdf%22%3B+filename%2A%3DUTF-8%27%27WindEurope-Offshore-wind-in-Europe-statistics-2020.pdf.

[7] James Carroll, Alasdair McDonald and David McMillan. 'Failure rate, repair time and unscheduled O&M cost analysis of offshore wind turbines: Reliability and maintenance of offshore wind turbines'. en. In: *Wind Energy* 19.6 (June 2016), pp. 1107–1119. ISSN: 10954244. DOI: 10.1002/we.1887. URL: https://onlinelibrary.wiley.com/doi/10.1002/we.1887 (visited on 06/06/2022).

[8] Vigdis Olden. *AEMON - Novel Failure Monitoring System for Marine Applications by including Acoustic Emission.* Nov. 2019. URL: https://www.sintef.no/en/projects/2019/aemon-/.

[9] Tonje Aasheim Nymark. 'Micro cracks in wind turbine bearings - Investigation of microstructural evolution and nanomechanical properties in White Etching Cracks (WEC)'. Project thesis. Trondheim: NTNU, Dec. 2021.

[10] M. -H. Evans et al. 'Confirming subsurface initiation at non-metallic inclusions as one mechanism for white etching crack (WEC) formation'. en. In: *Tribology International* 75 (July 2014), pp. 87–97. ISSN: 0301-679X. DOI: 10.1016/j.triboint.2014.03.012. URL: https://www.sciencedirect.com/science/article/pii/S0301679X14000991 (visited on 07/12/2021).

[11] H. K. D. H. Bhadeshia and R. W. K. Honeycombe. *Steels: microstructure and properties.* Fourth edition. OCLC: ocn974195800. Amsterdam: Butterworth-Heinemann, 2017. ISBN: 978-0-08-100270-4.

[12] L. Morsdorf et al. 'Moving cracks form white etching areas during rolling contact fatigue in bearings'. en. In: *Materials Science and Engineering: A* 771 (Jan. 2020), p. 138659. ISSN: 09215093. DOI: 10.1016/j.msea.2019.138659. URL: https://linkinghub.elsevier.com/retrieve/pii/S0921509319314455 (visited on 27/11/2021).

[13] Jan Ketil Solberg. *Teknologiske metaller og legeringer*. Trondheim: NTNU, 2017.

[14] William D. Callister and David G. Rethwisch. *Materials science and engineering.* eng. 9. ed., SI version. Hoboken, NJ: Wiley, 2015. ISBN: 978-1-118-31922-2.

[15] M.-H. Evans. 'An updated review: white etching cracks (WECs) and axial cracks in wind turbine gearbox bearings'. en. In: *Materials Science and Technology* 32.11 (July 2016), pp. 1133–1169. ISSN: 0267-0836, 1743-2847. DOI: 10.1080/02670836.2015.1133022. URL: https://www.tandfonline.com/doi/full/10.1080/02670836.2015.1133022 (visited on 09/12/2021).

[16] Bernard J. Hamrock and William J. Anderson. *Rolling-Element Bearings.* 1983.

[17] P. Malega, J. Kadarova and J. Kobulnicky. 'Improvement of Production Efficiency of Tapered Roller Bearing by Using Plant Simulation'. In: *International Journal of Simulation Modelling* 16.4 (Dec. 2016), pp. 682–693. ISSN: 17264529. DOI: 10.2507/IJSIMM16(4)10.405. URL: http://www.ijsimm.com/Full_Papers/Fulltext2017/text16-4_682-693.pdf (visited on 17/02/2022).

[18] H.K.D.H. Bhadeshia. 'Steels for bearings'. en. In: *Progress in Materials Science* 57.2 (Feb. 2012), pp. 268–435. ISSN: 00796425. DOI: 10.1016/j.pmatsci.2011.06.002. URL: https://linkinghub.elsevier.com/retrieve/pii/S0079642511000922 (visited on 17/10/2021).

[19] H. R. Hertz. *Miscellaneous Papers*. Ed. by Jones and Schott. London, UK: Macmillan, 1896.

[20] G. W. Stachowiak and A. W. Batchelor. *Engineering tribology*. Fourth edition. OCLC: ocn865545667. Oxford: Elsevier/Butterworth-Heinemann, 2014. ISBN: 978-0-12-397047-3.

[21] Gustaf Lundberg and Arvid Palmgren. 'Dynamic Capacity of Rolling Bearings'. en. In: *Journal of Applied Mechanics* 16.2 (June 1949), pp. 165–172. ISSN: 0021-8936, 1528-9036. DOI: 10.1115/1.4009930. URL: https://asmedigitalcollection.asme.org/appliedmechanics/article/16/2/165/1106338/Dynamic-Capacity-of-Rolling-Bearings (visited on 16/02/2022).

[22] Adam Ragheb and Mag Ragheb. 'Wind turbine gearbox technologies'. In: *2010 1st International Nuclear & Renewable Energy Conference (INREC)*. Amman, Jordan: IEEE, Mar. 2010, pp. 1–8. ISBN: 978-1-4244-5213-2. DOI: 10.1109/INREC.2010.5462549. URL: http://ieeexplore.ieee.org/document/5462549/ (visited on 09/05/2022).

[23] Andreas Heege, Jaume Betran and Yvan Radovcic. 'Fatigue load computation of wind turbine gearboxes by coupled finite element, multi-body system and aerodynamic analysis'. en. In: *Wind Energy* 10.5 (Sept. 2007), pp. 395–413. ISSN: 10954244, 10991824. DOI: 10.1002/we.226. URL: https://onlinelibrary.wiley.com/doi/10.1002/we.226 (visited on 07/06/2022).

[24] A. Grabulov, R. Petrov and H.W. Zandbergen. 'EBSD investigation of the crack initiation and TEM/FIB analyses of the microstructural changes around the cracks formed under Rolling Contact Fatigue (RCF)'. en. In: *International Journal of Fatigue* 32.3 (Mar. 2010), pp. 576–583. ISSN: 01421123. DOI: 10.1016/j.ijfatigue.2009.07.002. URL: https://linkinghub.elsevier.com/retrieve/pii/S0142112309002072 (visited on 19/10/2021).

[25] B. J. Gould and D. L. Burris. 'Effects of wind shear on wind turbine rotor loads and planetary bearing reliability: Pitch moments as contributors to wind turbine bearing failure'. en. In: *Wind Energy* 19.6 (June 2016), pp. 1011–1021. ISSN: 10954244. DOI: 10.1002/we.1879. URL: https://onlinelibrary.wiley.com/doi/10.1002/we.1879 (visited on 07/06/2022).

[26] Internationale Elektrotechnische Kommission and International Electrotechnical Commission, eds. *Wind turbines: Part 4: Design requirements for wind turbine gearboxes*. eng. Ed. 1.0. Wind turbines / IEC Part 4. Geneva: International Electrotechnical Commission, 2012. ISBN: 978-2-8322-0506-8.

[27] Zachary Shahan. *History of Wind Turbines*. Nov. 2014. URL: https://www.renewableenergyworld.com/storage/history-of-wind-turbines/#gref.

[28] Adnan Durakovic. *World's Most Powerful Wind Turbine Starts Producing*. Oct. 2021. URL: https://www.offshorewind.biz/2021/12/10/worlds-most-powerful-wind-turbine-starts-producing/.

[29] Reg Tucker. 'Proactive approach to gearbox repairs'. en. In: *Renewable Energy Focus* 15.1 (Jan. 2014), pp. 30–31. ISSN: 17550084. DOI: 10.1016/S1755-0084(14)70020-1. URL: https://linkinghub.elsevier.com/retrieve/pii/S1755008414700201 (visited on 06/06/2022).

[30] Viktorija Rumpf. 'A Study on Microstructural Alterations in White Etching Cracks, Dark Etching Region, and White Etching Bands in Rolling Contacts'. PhD. University of Southampton, Faculty of Engineering and the Environment, 2018.

[31] Arnaud Ruellan. 'Tribological analysis of White Etching Crack (WEC) failures in rolling element bearings'. English. physics.class-ph. INSA de Lyon, 2014. URL: https://tel.archives-ouvertes.fr/tel-01153235/.

[32] A. Kumar et al. 'In situ study on fracture behaviour of white etching layers formed on rails'. en. In: *Acta Materialia* 180 (Nov. 2019), pp. 60–72. ISSN: 13596454. DOI: 10.1016/j.actamat.2019.08.060. URL: https://linkinghub.elsevier.com/retrieve/pii/S1359645419305816 (visited on 21/11/2021).

[33] A. Greco et al. 'Material wear and fatigue in wind turbine Systems'. en. In: *Wear* 302.1-2 (Apr. 2013), pp. 1583–1591. ISSN: 00431648. DOI: 10.1016/j.wear.2013.01.060.

[34] M.-H. Evans et al. 'Serial sectioning investigation of butterfly and white etching crack (WEC) formation in wind turbine gearbox bearings'. en. In: *Wear* 302.1-2 (Apr. 2013), pp. 1573–1582. ISSN: 00431648. DOI: 10.1016/j.wear.2012.12.031. URL: https://linkinghub.elsevier.com/retrieve/pii/S0043164812004590 (visited on 09/12/2021).

[35] H.K. Danielsen, C. Hong and O.V. Mishin. ‘Microstructural characterization of white etching cracks in bearings after long-term operation in wind turbines’. en. In: *Materials Letters* 294 (July 2021), p. 129754. ISSN: 0167577X. DOI: 10.1016/j.matlet.2021.129754. URL: https://linkinghub.elsevier.com/retrieve/pii/S0167577X2100450X (visited on 16/04/2022).

[36] Mwj Lewis and B Tomkins. ‘A fracture mechanics interpretation of rolling bearing fatigue’. en. In: *Proceedings of the Institution of Mechanical Engineers, Part J: Journal of Engineering Tribology* 226.5 (May 2012), pp. 389–405. ISSN: 1350-6501, 2041-305X. DOI: 10.1177/1350650111435580. URL: http://journals.sagepub.com/doi/10.1177/1350650111435580 (visited on 16/06/2022).

[37] Kazuhiko Hiraoka, Misaki Nagao and Tatsuro Isomoto. ‘Study on Flaking Process in Bearings by White Etching Area Generation’. en. In: *Bearing Steel Technology-Advances and State of the Art in Bearing Steel Quality Assurance: 7th Volume.* Ed. by John M. Beswick. 100 Barr Harbor Drive, PO Box C700, West Conshohocken, PA 19428-2959: ASTM International, Jan. 2007, pp. 234–234–7. ISBN: 978-0-8031-3491-1. DOI: 10.1520/STP41656S. URL: http://www.astm.org/doiLink.cgi?STP41656S (visited on 09/12/2021).

[38] A. V. Olver. ‘The Mechanism of Rolling Contact Fatigue: An Update’. en. In: *Proceedings of the Institution of Mechanical Engineers, Part J: Journal of Engineering Tribology* 219.5 (May 2005), pp. 313–330. ISSN: 1350-6501, 2041-305X. DOI: 10.1243/135065005X9808. URL: http://journals.sagepub.com/doi/10.1243/135065005X9808 (visited on 09/12/2021).

[39] O. H. E. West et al. ‘Application of Complementary Techniques for Advanced Characterization of White Etching Cracks’. en. In: *Practical Metallography* 50.6 (June 2013), pp. 410–431. ISSN: 2195-8599, 0032-678X. DOI: 10.3139/147.110246. URL: https://www.degruyter.com/document/doi/10.3139/147.110246/html (visited on 09/12/2021).

[40] H. K. D. H. Bhadeshia and W. Solano-Alvarez. ‘Critical Assessment 13: Elimination of white etching matter in bearing steels’. en. In: *Materials Science and Technology* 31.9 (July 2015), pp. 1011–1015. ISSN: 0267-0836, 1743-2847. DOI: 10.1179/1743284715Y.0000000036. URL: https://www.tandfonline.com/doi/full/10.1179/1743284715Y.0000000036 (visited on 18/12/2021).

[41] D. Mayweg et al. ‘Correlation between grain size and carbon content in white etching areas in bearings’. en. In: *Acta Materialia* 215 (Aug. 2021), p. 117048. ISSN: 13596454. DOI: 10.1016/j.actamat.2021.117048. URL: https://linkinghub.elsevier.com/retrieve/pii/S1359645421004286 (visited on 17/11/2021).

[42] D. Mayweg et al. 'The role of carbon in the white etching crack phenomenon in bearing steels'. en. In: *Acta Materialia* 203 (Jan. 2021), p. 116480. ISSN: 13596454. DOI: 10.1016/j.actamat.2020.11.022. URL: https://linkinghub.elsevier.com/retrieve/pii/S1359645420308971 (visited on 09/12/2021).

[43] Yu Qin et al. 'Mechanism of cementite decomposition in 100Cr6 bearing steels during high pressure torsion'. en. In: *Acta Materialia* 201 (Dec. 2020), pp. 79–93. ISSN: 13596454. DOI: 10.1016/j.actamat.2020.09.069. URL: https://linkinghub.elsevier.com/retrieve/pii/S1359645420307631 (visited on 26/11/2021).

[44] Robert Errichello, Robert Budny and Rainer Eckert. 'Investigations of Bearing Failures Associated with White Etching Areas (WEAs) in Wind Turbine Gearboxes'. en. In: *Tribology Transactions* 56.6 (Nov. 2013), pp. 1069–1076. ISSN: 1040-2004, 1547-397X. DOI: 10.1080/10402004.2013.823531. URL: http://www.tandfonline.com/doi/abs/10.1080/10402004.2013.823531 (visited on 09/12/2021).

[45] T. Bruce et al. 'Characterisation of white etching crack damage in wind turbine gearbox bearings'. en. In: *Wear* 338-339 (Sept. 2015), pp. 164–177. ISSN: 00431648. DOI: 10.1016/j.wear.2015.06.008.

[46] Fernando José López-Uruñuela et al. 'Broad review of "White Etching Crack" failure in wind turbine gearbox bearings: Main factors and experimental investigations'. en. In: *International Journal of Fatigue* 145 (Apr. 2021), p. 106091. ISSN: 01421123. DOI: 10.1016/j.ijfatigue.2020.106091. URL: https://linkinghub.elsevier.com/retrieve/pii/S014211232030623X (visited on 04/06/2022).

[47] M.E. Curd et al. 'The heterogenous distribution of white etching matter (WEM) around subsurface cracks in bearing steels'. en. In: *Acta Materialia* 174 (Aug. 2019), pp. 300–309. ISSN: 13596454. DOI: 10.1016/j.actamat.2019.05.052. URL: https://linkinghub.elsevier.com/retrieve/pii/S1359645419303362 (visited on 17/11/2021).

[48] S. Kiranbabu et al. 'Cementite decomposition in 100Cr6 bearing steel during high-pressure torsion: Influence of precipitate composition, size, morphology and matrix hardness'. en. In: *Materials Science and Engineering: A* 833 (Jan. 2022), p. 142372. ISSN: 09215093. DOI: 10.1016/j.msea.2021.142372. URL: https://linkinghub.elsevier.com/retrieve/pii/S0921509321016361 (visited on 11/03/2022).

[49] Benjamin Gould et al. 'Figure the impact of steel microstructure and heat treatment on the formation of white etching cracks'. en. In: *Tribology International* 134 (June 2019), pp. 232–239. ISSN: 0301679X. DOI: 10.1016/j.tribo

int.2019.02.003. URL: https://linkinghub.elsevier.com/retrieve/pii/S0301679X19300660 (visited on 05/06/2022).

[50] Y.J. Li et al. 'Atomic scale characterization of white etching area and its adjacent matrix in a martensitic 100Cr6 bearing steel'. en. In: *Materials Characterization* 123 (Jan. 2017), pp. 349–353. ISSN: 10445803. DOI: 10.1016/j.matchar.2016.12.002. URL: https://linkinghub.elsevier.com/retrieve/pii/S1044580316311639 (visited on 21/11/2021).

[51] H.K. Danielsen et al. 'Multiscale characterization of White Etching Cracks (WEC) in a 100Cr6 bearing from a thrust bearing test rig'. en. In: *Wear* 370-371 (Jan. 2017), pp. 73–82. ISSN: 00431648. DOI: 10.1016/j.wear.2016.11.016. URL: https://linkinghub.elsevier.com/retrieve/pii/S0043164816306809 (visited on 21/11/2021).

[52] M.-H. Evans et al. 'A FIB/TEM study of butterfly crack formation and white etching area (WEA) microstructural changes under rolling contact fatigue in 100Cr6 bearing steel'. en. In: *Materials Science and Engineering: A* 570 (May 2013), pp. 127–134. ISSN: 09215093. DOI: 10.1016/j.msea.2013.02.004. URL: https://linkinghub.elsevier.com/retrieve/pii/S0921509313001160 (visited on 10/12/2021).

[53] R. Tricot, J. Monnot and M. Lluansi. 'HOW MICROSTRUCTURAL ALTERATIONS AFFECT FATIGUE PROPERTIES OF 52100 STEEL.' In: *Met Eng Q* 12.2 (May 1972), pp. 39–47.

[54] Benjamin Gould, Nicholaos G. Demas and Aaron C. Greco. 'The influence of steel microstructure and inclusion characteristics on the formation of premature bearing failures with microstructural alterations'. en. In: *Materials Science and Engineering: A* 751 (Mar. 2019), pp. 237–245. ISSN: 09215093. DOI: 10.1016/j.msea.2019.02.084. URL: https://linkinghub.elsevier.com/retrieve/pii/S0921509319302576 (visited on 18/11/2021).

[55] M.E. Curd et al. 'Redistribution of carbon caused by butterfly defects in bearing steels'. en. In: *Acta Materialia* 183 (Jan. 2020), pp. 390–397. ISSN: 13596454. DOI: 10.1016/j.actamat.2019.10.057. URL: https://linkinghub.elsevier.com/retrieve/pii/S1359645419307359 (visited on 13/06/2022).

[56] A. Grabulov, U. Ziese and H.W. Zandbergen. 'TEM/SEM investigation of microstructural changes within the white etching area under rolling contact fatigue and 3-D crack reconstruction by focused ion beam'. en. In: *Scripta Materialia* 57.7 (Oct. 2007), pp. 635–638. ISSN: 13596462. DOI: 10.1016/j.scriptamat.2007.06.024. URL: https://linkinghub.elsevier.com/retrieve/pii/S1359646207004228 (visited on 07/06/2022).

[57] Arnaud Ruellan et al. 'Understanding white etching cracks in rolling element bearings: The effect of hydrogen charging on the formation mechanisms'. en. In: *Proceedings of the Institution of Mechanical Engineers, Part J: Journal of Engineering Tribology* 228.11 (Nov. 2014), pp. 1252–1265. ISSN: 1350-6501, 2041-305X. DOI: 10.1177/1350650114522452. URL: http://journals.sagepub.com/doi/10.1177/1350650114522452 (visited on 18/11/2021).

[58] Mohanchand Paladugu, Douglas R. Lucas and R. Scott Hyde. 'Effect of lubricants on bearing damage in rolling-sliding conditions: Evolution of white etching cracks'. In: *Wear* 398-399 (Mar. 2018), pp. 165–177. DOI: 10.1016/j.wear.2017.12.001.

[59] A. D. Richardson et al. 'The Evolution of White Etching Cracks (WECs) in Rolling Contact Fatigue-Tested 100Cr6 Steel'. en. In: *Tribology Letters* 66.1 (Mar. 2018), p. 6. ISSN: 1023-8883, 1573-2711. DOI: 10.1007/s11249-017-0946-1. URL: http://link.springer.com/10.1007/s11249-017-0946-1 (visited on 19/04/2022).

[60] Benjamin Gould et al. 'Using advanced tomography techniques to investigate the development of White Etching Cracks in a prematurely failed field bearing'. en. In: *Tribology International* 116 (Dec. 2017), pp. 362–370. ISSN: 0301679X. DOI: 10.1016/j.triboint.2017.07.028. URL: https://linkinghub.elsevier.com/retrieve/pii/S0301679X17303742 (visited on 18/11/2021).

[61] J. Spille et al. 'A study on the initiation processes of white etching cracks (WECs) in AISI 52100 bearing steel'. en. In: *Wear* 477 (July 2021), p. 203864. ISSN: 00431648. DOI: 10.1016/j.wear.2021.203864. URL: https://linkinghub.elsevier.com/retrieve/pii/S0043164821002532 (visited on 07/12/2021).

[62] Annika M. Diederichs et al. 'Study of subsurface initiation mechanism for white etching crack formation'. en. In: *Materials Science and Technology* 32.11 (July 2016), pp. 1170–1178. ISSN: 0267-0836, 1743-2847. DOI: 10.1080/02670836.2016.1155842. URL: https://www.tandfonline.com/doi/full/10.1080/02670836.2016.1155842 (visited on 21/11/2021).

[63] Junbiao Lai and Kenred Stadler. 'Investigation on the mechanisms of white etching crack (WEC) formation in rolling contact fatigue and identification of a root cause for bearing premature failure'. en. In: *Wear* 364-365 (Oct. 2016), pp. 244–256. ISSN: 00431648. DOI: 10.1016/j.wear.2016.08.001. URL: https://linkinghub.elsevier.com/retrieve/pii/S0043164816301636 (visited on 18/12/2021).

[64] Mohanchand Paladugu and R. Scott Hyde. 'Microstructure deformation and white etching matter formation along cracks'. en. In: *Wear* 390-391 (Nov. 2017), pp. 367–375. ISSN: 00431648. DOI: 10.1016/j.wear.2017.08.014. URL: https://linkinghub.elsevier.com/retrieve/pii/S0043164817311328 (visited on 08/12/2021).

[65] H. K. D. H. Bhadeshia and W. Solano-Alvarez. 'Critical Assessment 13: Elimination of white etching matter in bearing steels'. en. In: *Materials Science and Technology* 31.9 (July 2015), pp. 1011–1015. ISSN: 0267-0836, 1743-2847. DOI: 10.1179/1743284715Y.0000000036. URL: https://www.tandfonline.com/doi/full/10.1179/1743284715Y.0000000036 (visited on 09/12/2021).

[66] W. Solano-Alvarez and H. K. D. H. Bhadeshia. 'White-Etching Matter in Bearing Steel. Part II: Distinguishing Cause and Effect in Bearing Steel Failure'. en. In: *Metallurgical and Materials Transactions A* 45.11 (Oct. 2014), pp. 4916–4931. ISSN: 1073-5623, 1543-1940. DOI: 10.1007/s11661-014-2431-x. URL: http://link.springer.com/10.1007/s11661-014-2431-x (visited on 27/11/2021).

[67] Benjamin Gould and Aaron Greco. 'Investigating the Process of White Etching Crack Initiation in Bearing Steel'. en. In: *Tribology Letters* 62.2 (May 2016), p. 26. ISSN: 1023-8883, 1573-2711. DOI: 10.1007/s11249-016-0673-z. URL: http://link.springer.com/10.1007/s11249-016-0673-z (visited on 18/12/2021).

[68] T. Bruce et al. 'Formation of white etching cracks at manganese sulfide (MnS) inclusions in bearing steel due to hammering impact loading: White etching crack formation in bearing steel'. en. In: *Wind Energy* 19.10 (Oct. 2016), pp. 1903–1915. ISSN: 10954244. DOI: 10.1002/we.1958. URL: https://onlinelibrary.wiley.com/doi/10.1002/we.1958 (visited on 19/10/2021).

[69] Joerg Franke et al. 'White Etching Cracking—Simulation in Bearing Rig and Bench Tests'. en. In: *Tribology Transactions* 61.3 (May 2018), pp. 403–413. ISSN: 1040-2004, 1547-397X. DOI: 10.1080/10402004.2017.1339839. URL: https://www.tandfonline.com/doi/full/10.1080/10402004.2017.1339839 (visited on 04/06/2022).

[70] Mohanchand Paladugu and R. Scott Hyde. 'White etching matter promoted by intergranular embrittlement'. en. In: *Scripta Materialia* 130 (Mar. 2017), pp. 219–222. ISSN: 13596462. DOI: 10.1016/j.scriptamat.2016.11.030. URL: https://linkinghub.elsevier.com/retrieve/pii/S135964621630584X (visited on 18/11/2021).

[71] M.-H. Evans et al. ‘Effect of hydrogen on butterfly and white etching crack (WEC) formation under rolling contact fatigue (RCF)’. en. In: *Wear* 306.1-2 (Aug. 2013), pp. 226–241. ISSN: 00431648. DOI: 10.1016/j.wear.2013.03.008. URL: https://linkinghub.elsevier.com/retrieve/pii/S0043164813001877 (visited on 08/12/2021).

[72] Walter Holweger et al. ‘White Etching Crack Root Cause Investigations’. en. In: *Tribology Transactions* 58.1 (Jan. 2015), pp. 59–69. ISSN: 1040-2004, 1547-397X. DOI: 10.1080/10402004.2014.942938. URL: http://www.tandfonline.com/doi/abs/10.1080/10402004.2014.942938 (visited on 21/11/2021).

[73] Wolfram Kruhöffer and Jörg Loos. ‘WEC Formation in Rolling Bearings under Mixed Friction: Influences and “Friction Energy Accumulation” as Indicator’. en. In: *Tribology Transactions* 60.3 (May 2017), pp. 516–529. ISSN: 1040-2004, 1547-397X. DOI: 10.1080/10402004.2016.1183250. URL: https://www.tandfonline.com/doi/full/10.1080/10402004.2016.1183250 (visited on 08/12/2021).

[74] Kenichi Iso, Atsushi Yokouchi and Hiromichi Takemura. ‘Research Work for Clarifying the Mechanism of White Structure Flaking and Extending the Life of Bearings’. In: Apr. 2005, pp. 2005–01–1868. DOI: 10.4271/2005-01-1868. URL: https://www.sae.org/content/2005-01-1868/ (visited on 08/12/2021).

[75] C. Newlands, A. Olver and N. Brandon. ‘Gaseous evolution of hydrogen from hydrocarbon oil and grease lubricated contacts’. en. In: *Tribology Series*. Vol. 41. Elsevier, 2003, pp. 719–726. ISBN: 978-0-444-51243-7. DOI: 10.1016/S0167-8922(03)80185-2. URL: https://linkinghub.elsevier.com/retrieve/pii/S0167892203801852 (visited on 02/06/2022).

[76] Mika Kohara, Takayuki Kawamura and Masaki Egami. ‘Study on Mechanism of Hydrogen Generation from Lubricants’. en. In: *Tribology Transactions* 49.1 (Apr. 2006), pp. 53–60. ISSN: 1040-2004, 1547-397X. DOI: 10.1080/05698190500486324. URL: http://www.tandfonline.com/doi/abs/10.1080/05698190500486324 (visited on 08/12/2021).

[77] D. Ray et al. ‘Hydrogen embrittlement of a stainless ball bearing steel’. en. In: *Wear* 65.1 (Dec. 1980), pp. 103–111. ISSN: 00431648. DOI: 10.1016/0043-1648(80)90012-5. URL: https://linkinghub.elsevier.com/retrieve/pii/0043164880900125 (visited on 02/06/2022).

[78] Jürgen Wranik et al. ‘A Study on Decisive Early Stages in White Etching Crack Formation Induced by Lubrication’. en. In: *Lubricants* 10.5 (May 2022), p. 96. ISSN: 2075-4442. DOI: 10.3390/lubricants10050096. URL: https://www.mdpi.com/2075-4442/10/5/96 (visited on 02/06/2022).

[79] Tabassumul Haque et al. ‘Lubricant Effects on White Etching Cracking Failures in Thrust Bearing Rig Tests’. en. In: *Tribology Transactions* 61.6 (Nov. 2018), pp. 979–990. ISSN: 1040-2004, 1547-397X. DOI: 10.1080/10402004.2018.1453571. URL: https://www.tandfonline.com/doi/full/10.1080/10402004.2018.1453571 (visited on 02/06/2022).

[80] Joerg Loos, Iris Bergmann and Matthias Goss. ‘Influence of Currents from Electrostatic Charges on WEC Formation in Rolling Bearings’. en. In: *Tribology Transactions* 59.5 (Sept. 2016), pp. 865–875. ISSN: 1040-2004, 1547-397X. DOI: 10.1080/10402004.2015.1118582. URL: https://www.tandfonline.com/doi/full/10.1080/10402004.2015.1118582 (visited on 04/06/2022).

[81] Hidenobu Mikami and Takayuki Kawamura. ‘Influence of Electrical Current on Bearing Flaking Life’. In: Apr. 2007, pp. 2007–01–0113. DOI: 10.4271/2007-01-0113. URL: https://www.sae.org/content/2007-01-0113/ (visited on 04/06/2022).

[82] Steven Chatterton, Paolo Pennacchi and Andrea Vania. ‘Electrical pitting of tilting-pad thrust bearings: Modelling and experimental evidence’. en. In: *Tribology International* 103 (Nov. 2016), pp. 475–486. ISSN: 0301679X. DOI: 10.1016/j.triboint.2016.08.003. URL: https://linkinghub.elsevier.com/retrieve/pii/S0301679X16302493 (visited on 04/06/2022).

[83] F. Steinweg et al. ‘Formation of White Etching Cracks under electrical current flow - Influence of load, slip and polarity’. en. In: *Wear* (May 2022), p. 204394. ISSN: 00431648. DOI: 10.1016/j.wear.2022.204394. URL: https://linkinghub.elsevier.com/retrieve/pii/S0043164822001557 (visited on 13/06/2022).

[84] R. H. Vegter and J. T. Slycke. ‘The Role of Hydrogen on Rolling Contact Fatigue Response of Rolling Element Bearings’. en. In: *Bearing Steel Technologies: Developments in Rolling Bearing Steels and Testing*. Ed. by John M. Beswick. 100 Barr Harbor Drive, PO Box C700, West Conshohocken, PA 19428-2959: ASTM International, Jan. 2010, pp. 201–201–17. ISBN: 978-0-8031-7510-5. DOI: 10.1520/STP49130S. URL: http://www.astm.org/doiLink.cgi?STP49130S (visited on 05/06/2022).

[85] M.-H. Evans et al. ‘White etching crack (WEC) investigation by serial sectioning, focused ion beam and 3-D crack modelling’. en. In: *Tribology International* 65 (Sept. 2013), pp. 146–160. ISSN: 0301679X. DOI: 10.1016/j.triboint.2013.03.022. URL: https://linkinghub.elsevier.com/retrieve/pii/S0301679X13001680 (visited on 18/10/2021).

[86] Young Sup Kang, Ryan D. Evans and Gary L. Doll. 'Roller-Raceway Slip Simulations of Wind Turbine Gearbox Bearings Using Dynamic Bearing Model'. In: *STLE/ASME 2010 International Joint Tribology Conference*. San Francisco, California, USA: ASMEDC, Jan. 2010, pp. 407–409. ISBN: 978-0-7918-4419-9 978-0-7918-3890-7. DOI: 10.1115/IJTC2010-41191. URL: https://asmedigitalcollection.asme.org/IJTC/proceedings/IJTC2010/44199/407/348675 (visited on 08/12/2021).

[87] J.C. Gregory. 'Chemical conversion coatings of metals to resist scuffing and wear'. en. In: *Tribology International* 11.2 (Apr. 1978), pp. 105–112. ISSN: 0301679X. DOI: 10.1016/0301-679X(78)90137-8. URL: https://linkinghub.elsevier.com/retrieve/pii/0301679X78901378 (visited on 05/06/2022).

[88] Kenred Stadler et al. 'Benefits of Using Black Oxidized Bearings in Wind Applications'. In: *Evolution* (Jan. 2015). URL: https://evolution.skf.com/en/benefits-of-using-black-oxidized-bearings-in-wind-applications/.

[89] *ISO 683-17 Heat-treated steels, alloy steels and free-cutting steels - Part 17: Ball and roller bearing steels*. Tech. rep. International Organization for Standardization, 2014.

[90] Jarle Hjelen. *Scanning elektron-mikroskopi*. Trondheim: Metallurgisk institutt, NTH, Aug. 1989. URL: https://www.nb.no/items/4103cf534b134a2f8edceb208f901e0d?page=1.

[91] Stuart I. Wright and Matthew M. Nowell. 'EBSD Image Quality Mapping'. en. In: *Microscopy and Microanalysis* 12.01 (Feb. 2006), pp. 72–84. ISSN: 1431-9276, 1435-8115. DOI: 10.1017/S1431927606060090. URL: http://www.journals.cambridge.org/abstract_S1431927606060090 (visited on 14/11/2021).

[92] S.I. Wright. 'Orientation Texture'. en. In: *Encyclopedia of Condensed Matter Physics*. Elsevier, 2005, pp. 221–233. ISBN: 978-0-12-369401-0. DOI: 10.1016/B0-12-369401-9/00696-3. URL: https://linkinghub.elsevier.com/retrieve/pii/B0123694019006963 (visited on 14/11/2021).

[93] Hualong Li et al. 'Deformation mechanism and texture and microstructure evolution during high-speed rolling of AZ31B Mg sheets'. en. In: *Journal of Materials Science* 43.22 (Nov. 2008), pp. 7148–7156. ISSN: 0022-2461, 1573-4803. DOI: 10.1007/s10853-008-3021-3. URL: https://link.springer.com/10.1007/s10853-008-3021-3 (visited on 16/06/2022).

[94] Bharat Bhushan and Manuel L. B. Palacio. 'Nanoindentation'. en. In: *Encyclopedia of Nanotechnology*. Ed. by Bharat Bhushan. Dordrecht: Springer, 2012. ISBN: 978-90-481-9750-7. DOI: 10.1007/978-90-481-9751-4_100475.

[95] W.C. Oliver and G.M. Pharr. ‘An improved technique for determining hardness and elastic modulus using load and displacement sensing indentation experiments’. en. In: *Journal of Materials Research* 7.6 (June 1992), pp. 1564–1583. ISSN: 0884-2914, 2044-5326. DOI: 10.1557/JMR.1992.1564. URL: http://link.springer.com/10.1557/JMR.1992.1564 (visited on 12/11/2021).

[96] *ISO 14577-1 Metallic materials - Instrumented indentation test for hardness and materials parameters - Part 1: Test method.* Tech. rep. International Organization for Standardization, 2015.

[97] Emilio Jiménez-Piqué, Yves Gaillard and Marc Anglada. ‘Instrumented Indentation of Layered Ceramic Materials’. In: *Key Engineering Materials* 333 (Mar. 2007), pp. 107–116. ISSN: 1662-9795. DOI: 10.4028/www.scientific.net/KEM.333.107. URL: https://www.scientific.net/KEM.333.107 (visited on 12/11/2021).

[98] Viktorija Šmeļova et al. ‘Microstructural changes in White Etching Cracks (WECs) and their relationship with those in Dark Etching Region (DER) and White Etching Bands (WEBs) due to Rolling Contact Fatigue (RCF)’. en. In: *International Journal of Fatigue* 100 (July 2017), pp. 148–158. ISSN: 01421123. DOI: 10.1016/j.ijfatigue.2017.03.027. URL: https://linkinghub.elsevier.com/retrieve/pii/S014211231730141X (visited on 11/06/2022).

[99] Dieter Radaj and Michael Vormwald. *Fatigue assessment methods.* New York: Springer, 2012. ISBN: 978-3-642-30739-3.

[100] M. Oezel et al. ‘Formation of white etching areas in SAE 52100 bearing steel under rolling contact fatigue – Influence of diffusible hydrogen’. en. In: *Wear* 414-415 (Nov. 2018), pp. 352–365. ISSN: 00431648. DOI: 10.1016/j.wear.2018.08.022. URL: https://linkinghub.elsevier.com/retrieve/pii/S0043164818308524 (visited on 13/06/2022).

# Appendix

# A EPMA results

## A Case-hardened steel

EPMA analysis of area A3 in the case-hardened steel. The elements tested were silicon, oxygen, carbon, manganese, chromium, iron, molybdenum and nickel.

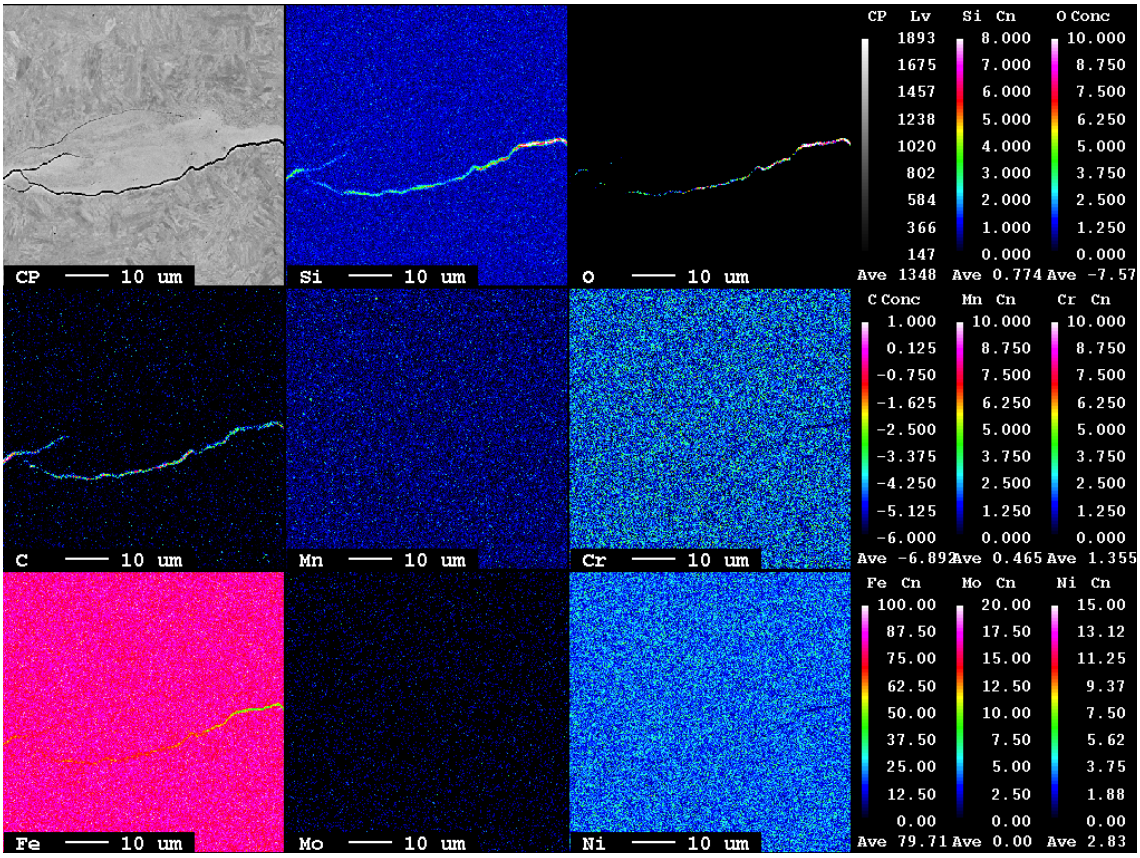

**Figure A.1.** EPMA result from area A3 in case-hardened steel.

# B Through-hardened steel

EPMA analysis of area B5 in the through-hardened steel is presented in Figure A.2. The elements tested were aluminium, oxygen, sulphur, carbon, chromium, manganese and iron.

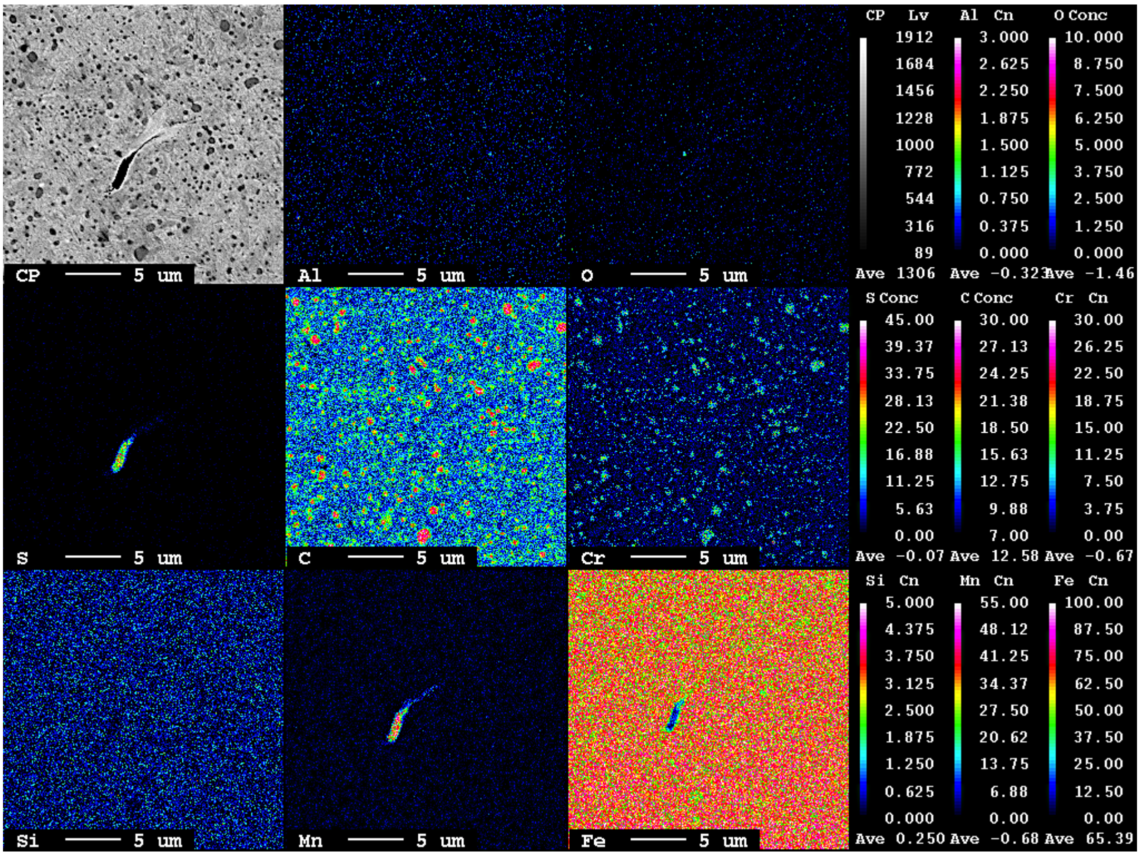

**Figure A.2.** Result from EPMA analysed WEC B5 in through-hardened steel.

EPMA analysis of area B15 in the through-hardened steel is presented in Figure A.3. The elements tested were aluminium, oxygen, sulphur, carbon, chromium, manganese and iron.

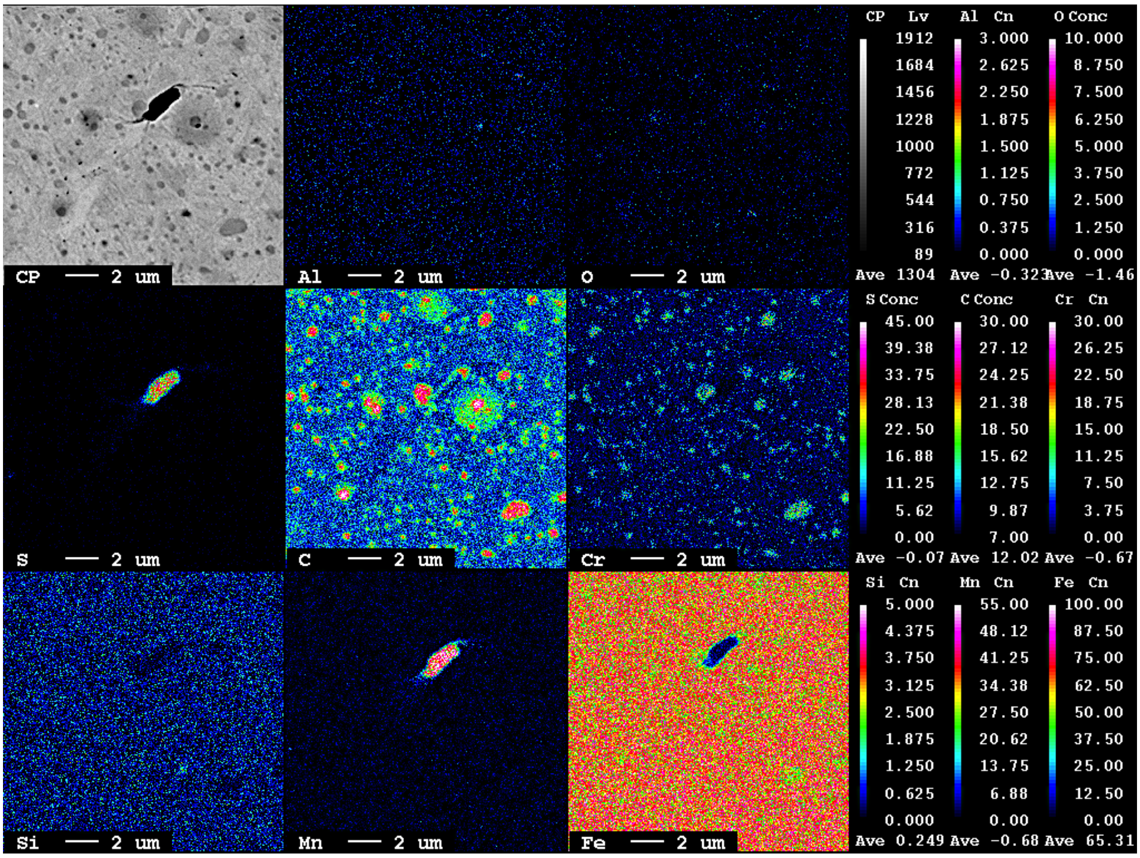

**Figure A.3.** Result from EPMA analysed WEC B15 in through-hardened steel.

EPMA analysis of area B16 in the through-hardened steel is presented in Figure A.4. The elements tested were aluminium, oxygen, sulphur, carbon, chromium, manganese and iron.

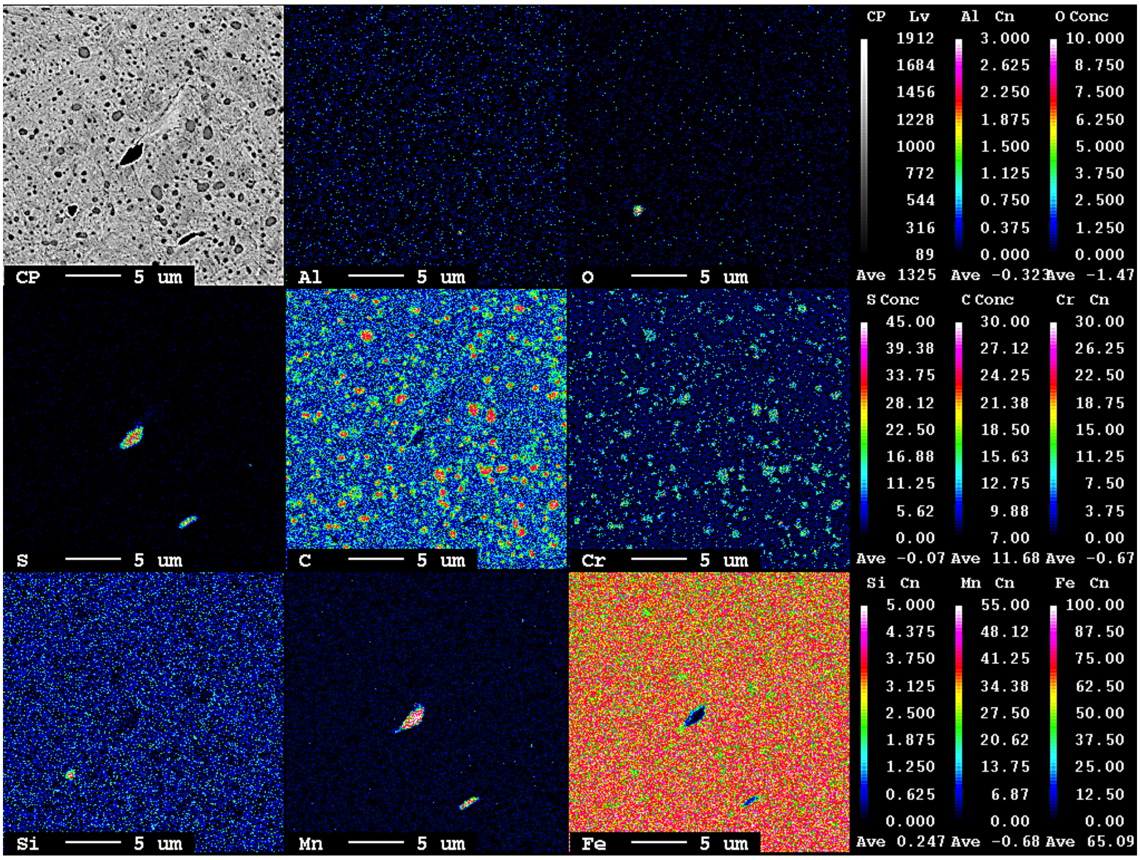

**Figure A.4.** Result from EPMA analysed WEC B16 in through-hardened steel.

# B Nanoindentation

Table B.1 presents all nanoindentation hardness data from point measurements.

**Table B.1.** Hardness values form nanoindentation point measurements.

| Area | Indent number | Hardness (GPa) |
|---|---|---|
| **Matrix** | | |
| Matrix | 0 | 6.410309 |
| Matrix | 1 | 5.761042 |
| Matrix | 2 | 6.209274 |
| Matrix | 3 | 6.017179 |
| Matrix | 4 | 6.151573 |
| Matrix | 5 | 5.386369 |
| Matrix | 6 | 5.884022 |
| Matrix | 7 | 5.697124 |
| Matrix | 8 | 5.052456 |
| Matrix | 9 | 5.901290 |
| Matrix | 10 | 6.070963 |
| Matrix | 11 | 5.555909 |
| Matrix | 12 | 5.337570 |
| Matrix | 13 | 5.644518 |
| Matrix | 14 | 6.109480 |
| Matrix | 15 | 5.126152 |
| **WEC B10** | | |
| WEM | 1 | 8.030574 |
| WEM | 2 | 8.975671 |
| WEM | 3 | 8.017611 |
| WEM | 4 | 7.997712 |
| WEM | 5 | 7.965967 |
| WEM | 6 | 7.463436 |
| WEM | 7 | 8.878464 |
| WEM | 8 | 7.969308 |
| WEM | 9 | 7.322167 |
| WEM | 10 | 7.781137 |
| Matrix | 11 | 6.519295 |
| Matrix | 12 | 6.476665 |
| Matrix | 13 | 6.464765 |
| **WEC B11** | | |
| Inclusion | 0 | 8.425065 |
| Inclusion | 1 | 8.779365 |
| WEM | 2 | 7.349036 |
| WEM | 3 | 7.424241 |
| WEM | 4 | 7.429843 |

NTNU
Norwegian University of
Science and Technology